# Lawrence Berkeley National Laboratory

## LBL Publications

**Title**

Search for Time Reversal Invariance Violation in the Beta-Decay of 56Co

**Permalink**

https://escholarship.org/uc/item/3756k0fw

**Author**

Mortara, Justin L, Ph.D. Thesis

**Publication Date**

1999-02-01

**Copyright Information**

# ERNEST ORLANDO LAWRENCE BERKELEY NATIONAL LABORATORY

BERKELEY LAB

# Search for Time Reversal Invariance Violation in the Beta-Decay of $^{56}$Co

Justin L. Mortara

**Nuclear Science Division**

February 1999

Ph.D. Thesis

## DISCLAIMER

# Search for Time Reversal Invariance Violation in the Beta-Decay of $^{56}$Co

Justin Louis Mortara
Ph.D. Thesis

Department of Physics
University of California, Berkeley

and

Nuclear Science Division
Ernest Orlando Lawrence Berkeley National Laboratory
University of California
Berkeley, CA 94720

February 1999

Search for time reversal invariance violation in the beta-decay of $^{56}$Co

by

Justin Louis Mortara

B.A. (University of Chicago) 1992

A dissertation submitted in partial satisfaction of the

requirements for the degree of

Doctor of Philosophy
in

Physics

in the

GRADUATE DIVISION

of the

UNIVERSITY OF CALIFORNIA, BERKELEY

Committee in charge:

Professor Stuart J. Freedman, Chair
Professor J. David Jackson
Professor Eugene H. Haller

Spring 1999

# Search for Time Reversal Invariance Violation in the Beta-Decay of $^{56}$Co

Copyright © 1999

by

Justin Louis Mortara

# Abstract

Search for time reversal invariance violation in the beta-decay of $^{56}$Co

by

Justin Louis Mortara

Doctor of Philosophy in Physics

University of California, Berkeley

Professor Stuart J. Freedman, Chair

This thesis describes a search for time reversal invariance violation in the isospin hindered beta-decay of $^{56}$Co. In particular, we have searched for a $T$ odd corrleation of the form $E_1(\hat{J} \cdot \hat{k})(\hat{J} \cdot \hat{p} \times \hat{k})$, where $\hat{J}$, $\hat{p}$ and $\hat{k}$ represent the nuclear spin, positron momentum and photon momentum respectively. The result, $E_1 = -0.001 \pm 0.006$, is consistent with no time reversal invariance violation.

*For Anne.*

# Acknowledgements

The guidance and tutelage of Professor Stuart J. Freedman was invaluable through the course of this work. While he encouraged me to work independently, his persistent and insightful questions kept me from pursuing too many fruitless ends. Most importantly, I was allowed to be stubborn and learn freely from my own mistakes. The result was an immensely rewarding research experience filled with a strong sense of self-accomplishment. As I take on greater responsibilities, I hope to emulate this style and to treat others with the same degree of freedom.

The work at low temperatures was only possible with a host of other highly skilled collaborators. Professor Seamus Davis provided the necessary introduction to the diverse world of low temperature physics. His energy and enthusiasm for physics research was truly inspirational. Other members of his group, including graduate students Eric Hudson, Andrew Schechter, and especially Kristine Lang, provided invaluable practical assistance and guidance with running the dilution refrigerator.

Don Syversrud and David Ruiz were critical to the success of this project. Their expert technical support in the construction and design of the apparatus was invaluable and their spirited camaraderie kept me moving forward during the most frustrating times.

Finally, Anne L. Clunan provided the much-needed emotional support to see everything through to completion. Her patience and encouragement made seemingly impossible tasks possible.

# Contents

# Chapter 1

# Introduction

## 1.1 The Role of Symmetries in Physics

Theories of physics develop according to the belief that simpler is better. This idea is best expressed by Occam's razor, which states that "...entities are not to be multiplied beyond necessity." Hence, a simpler theory that explains the experimental observations is superior to a more complex one that is capable of explaining those same observations. To achieve the desired theoretical simplicity, physics often asserts symmetry principles that reduce potential complexity. To be sure, these symmetry principles are subject to experimental verification. After all, the notion of simplicity is somewhat subjective.

A particular class of symmetries are the discrete space-time symmetries. Included in this class are symmetries of charge ($C$), parity ($P$) and time ($T$). Each of these is associated with a particular invariance principle: conservation of charge symmetry is associated with invariance under particle anti-particle exchange, parity with invariance under spatial reflection and time with invariance under motion reversal. Based upon observations of reflection invariance in our physical space, parity conservation was once considered inviolate. The electromagnetic interaction proved to obey this symmetry and Fermi's initial formulation of the weak interaction, based upon the electromagnetic interaction, was also explicitly parity conserving[1].

This universal notion of parity conservation was undone by the $\tau - \theta$ puzzle. Two

different meson decay modes, one going into $3\pi$ and the other into $2\pi$, were observed. These two final states have different parities. Therefore, if the decay interaction was parity conserving, then the different parity final states must be associated with two distinct initial particles. These particles were named $\tau$ and $\theta$[2]. The $\tau-\theta$ puzzle arose because observations of the masses and lifetimes of these supposedly distinct particles suggested that they were identical[3]. A solution to this puzzle was suggested by T. D. Lee and C. N. Yang who observed that there was no conclusive evidence that the weak interaction conserved or violated parity invariance[4]. If parity conservation was violated, then the $\tau$ and $\theta$ could be the same particle decaying to two different parity final states. Following this suggestion, three measurements performed in rapid succession yielded conclusive evidence that parity conservation was indeed violated by the weak interaction. In the beta-decay of polarized $^{60}$Co[5], the electron momentum exhibited a dependence on the parity odd observable $\hat{J}\cdot\hat{p}$, where $\hat{J}$ is the nuclear spin of the $^{60}$Co and $\hat{p}$ is the electron momentum. Electrons where emitted preferentially anti-parallel to the spin of the nucleus. Other observations of parity violation were made in the decay sequence $\pi^+ \to \mu^+ \to e^+$[6][7]. These experiments utilized an elegant technique based on the prediction of Lee and Yang that the $\mu$ emitted from the $\pi$ decay would be polarized. The subsequent decay of the $\mu \to e\nu\nu$ could then be probed for parity violating signals depending on the muon spin and electron momentum.

In the framework of a four fermion interaction, these observations suggested that the neutrino and electrons participating in the weak interaction would have a definite "handedness." That is, these particles had a non-vanishing expectation value for $\hat{\sigma}\cdot\hat{p}$, where $\hat{\sigma}$ and $\hat{p}$ are the spin and momentum respectively. The handedness of these particles was determined by a series of experiments[8][9]. It was concluded that the neutrino and electron were left handed, while the positron and anti-neutrino were right handed. This demonstrated that charge symmetry invariance, in addition to parity conservation, was violated in the weak interaction. Under $C$, the left-handed neutrino becomes the non-existent (or, at least, unobserved) left-handed anti-neutrino. These results, combined with measurements of other beta-decay observables, led to the formulation of the V - A theory of the weak interaction in which parity is maximally violated.

It was then realized that the weak interaction, while separately violating the conservation of parity and charge symmetries, was seemingly invariant under the combined transformation of charge-parity or $CP$. All observed weak decays, while violating $P$, appeared to conserve $CP$. This meant that the weak interaction states should be expressed as states of definite $CP$, rather than states of definite $P$. In the neutral kaon system, this implied that decaying kaon states should not be expressed as strong interaction eigenstates, $K^0$ and $\bar{K}^0$, since these are not states of definite $CP$ and hence are not eigenstates of the weak interaction. Instead, the states of definite $CP$ are linear combinations of the strong eigenstates

$$|K_1^0> = \frac{1}{\sqrt{2}}[|K^0> - |\bar{K}^0>] \tag{1.1}$$

$$|K_2^0> = \frac{1}{\sqrt{2}}[|K^0> + |\bar{K}^0>] \tag{1.2}$$

where $K_1^0$ has $CP = +1$ and $K_2^0$ has $CP = -1$. Since the $2\pi$ final state has $CP = +1$ and the $3\pi$ final state has $CP = -1$, $K_1^0$ decays much faster than the $K_2^0$ due to available phase space. For this reason, under the assumption of $CP$ invariance, the $K_1^0$ is associated with the $K_S^0$ (S for short-lived) and the $K_2^0$ with $K_L^0$ (L for long-lived). Hence, $CP$ invariance demands that $K_L^0$ cannot decay into $2\pi$. Less than ten years after the discovery of parity violation, the observation of $K_L^0 \to 2\pi$ led to the fall of $CP$ invariance[10]. The very small branch of $CP$ violating decay is characterized by

$$|\eta_{+-}| = \frac{(K_L^0 \to 2\pi)}{(K_L^0 \to 3\pi)} \tag{1.3}$$

where $\eta_{+-} \approx 2 \times 10^{-3}$. The mechanism for incorporating this observed $CP$ violation in the Standard Model is phenomenological. By including an additional phase in the Cabibbo-Kobayishi-Maskawa (CKM) matrix, the experimentally required $CP$ violation is produced. Since the CKM matrix is a 3 x 3 rotation matrix, it requires only three real parameters if the rotation is purely real. The additional phase is a fourth parameter which introduces a complex component into the CKM matrix that cannot be absorbed by simply redefining normalizations. This complex component gives rise to an expression of $CP$ violation in

3

the Standard Model. To date, a deeper understanding of the origins of this symmetry violation is lacking and as such it is worthy of further study. To be fair, there is also no theoretical motivation for why parity is maximally violated in the weak interaction. Both $P$ and $CP$ violation are observations which have been inserted into the Standard Model. These symmetry principles have fallen with little theoretical insight as to why.

With the fall of the $P$ and $CP$ invariance principles, a natural question arises: what of $CPT$? Interestingly, a strong statement about $CPT$ invariance was made long before the discovery of $CP$ violation. General assumptions inherit in modern relativistic field theories: Lorentz invariance (all inertial frames observe the same laws of physics), locality (no action at a distance) and the usual connection between spin and statistics, together imply $CPT$ invariance[11]. The most precise means of testing $CPT$ invariance is comparison of particle and anti-particle masses. According to $CPT$ invariance, these masses should be identical. In particular, the mass difference of the $K^0$ and the $\bar{K}^0$ is consistent with $CPT$ invariance[12] at a level

$$\left| \frac{(m_{\bar{K}^0} - m_{K^0})}{m_{K^0}} \right| \leq 10^{-18} \tag{1.4}$$

Conservation of $CPT$, coupled with $CP$ violation, implies that $T$ should be violated. The question remains: where should $T$ invariance violation appear?

## 1.2   Searches for $T$ invariance violation

Searches for $T$ invariance violation can be grouped into three broad categories. One category belongs to detailed balance experiments. These experiments measure differential cross-sections of reactions in both a forward and backward sense of time. Time reversal invariance requires that the forward and backward reactions yield the same result. Consider a measurement where projectiles $A$ and $B$ collide to produce $C$ and $D$. The differential cross-sections for this reaction, $B(A, C)D$, can be measured in detail. Time reversal invariance requires that if the experiment is run backwards in time, so that $C$ and $D$ collide to produce $A$ and $B$, the same differential cross-sections will be measured. Hence measurements determined from $B(A, C)D$ should agree with those determined from $D(C, A)B$. The

most precise experiment of this variety indicates agreement with $T$ invariance at a level of $5 \times 10^{-4}$[13]. This experiment is sensitive to $T$ invariance violation in the strong interaction through comparison of the differential cross-sections in the strong processes $Mg(\alpha,p)Al$ and $Al(p,\alpha)Mg$.

Another probe of $T$ invariance violation involves searches for permanent electric dipole moments of "fundamental" particles. If a non-zero electric dipole moment (EDM) exists, then another quantum number, in addition to that associated with the magnetic dipole moment, might be necessary to describe a particle state. However, such an additional quantum number increases the number of possible particle states. Since the observed spin statistics of fermions are satisfied with a single spin quantum number, the EDM cannot contribute an additional independent quantum number. This means that an electric dipole moment of a fundamental particle must be parallel or anti-parallel to the magnetic dipole moment or spin. Therefore, an EDM, $d_e$ can be expressed as

$$d_e \rightarrow d_e \vec{S} \qquad (1.5)$$

where $\vec{S}$ is the spin operator associated with the magnetic dipole moment. Now, such an EDM interacting with an external electric field will have energy $U = -d_e \vec{S} \cdot \vec{E}$. Under $T$, this transforms to $U = d_e \vec{S} \cdot \vec{E}$ since $\vec{E}$ is even and $\vec{S}$ is odd. Hence, a non-zero EDM is $T$ violating. The most sensitive measurements in this category come from the neutron[14] and the electron[15] electric dipole moments, both of which have set limits at levels below $10^{-25}e{\cdot}cm$.

The third category of $T$ invariance tests involves measurements of $T$ odd correlations in particle decays. These experiments are analogous to the beta-decay parity violation measurements, but the correlation term sought is a scalar or pseudoscalar constructed of an odd number of $T$ odd observables. Decay correlations from electromagnetic[16], strong[17] and weak processes have been investigated. In this work, emphasis will be placed on weak interaction decays where a variety of measurements have been performed.

In a recent investigation of the weak decay $K_L \rightarrow \pi\pi\gamma \rightarrow \pi\pi ee$, a correlation of the

form

$$(\hat{n_\pi} \times \hat{n_e}) \cdot \hat{p_\pi} (\hat{n_\pi} \cdot \hat{n_e}) \qquad (1.6)$$

was measured and found to be non-zero[18]. In this correlation, $\hat{n_\pi}$ and $\hat{n_e}$ represent the unit vectors perpendicular to the decay planes defined by the pions and the electrons respectively. These involve the cross product of the pion momenta or the electron-positron momenta and hence they are even under a $T$ transformation. The remaining term, $\hat{p_\pi}$ is the pion momentum which is odd under the $T$ and therefore the entire correlation is $T$ odd. The preliminary non-zero value for this correlation is consistent with a prediction based on the CKM matrix[19][20]. This measurement shows that the same parameterization used to explain neutral kaon $CP$ violation is also capable of producing $T$ violation in the same system. However, it does little to improve the understanding of the mechanism for $CP$ violation and why it has only been observed in the neutral kaons.

Other correlations in non-strange decays, in particular those in nuclear beta-decay, have been investigated over the years. A summary of the different decay correlations measured in nuclear beta-decay is shown in Table 1.1. For each measurement, the correlation contribution due to final state interactions, where calculated, is shown. These final state interactions are $T$ conserving interactions that contribute a non-zero value to the $T$ violating correlations. Since they arise from the electromagnetic interaction between the outgoing beta particle and the daughter nucleus, the final state interactions generally increase with increasing atomic number $Z$.

The most significant limits on $T$ invariance violation in this area come from the decay of the $n$ and $^{19}$Ne. In both of these experiments, a $T$ odd, $P$ even correlation of the form

$$D\hat{J} \cdot (\hat{p_e} \times \hat{p_\nu}) \qquad (1.7)$$

is searched for. In this correlation, $J$, $p_e$ and $p_\nu$ are the initial nuclear spin, electron and neutrino momenta respectively. In these experiments, the low energy recoiling daughter nucleus is detected instead of the neutrino momentum. Limits on the $D$ coefficient from $n$ decay are $D_n = (1.1 \pm 1.7) \times 10^{-3}$[21] and from $^{19}$Ne decay $D_{^{19}Ne} = (0.4 \pm 0.8) \times 10^{-3}$[22].

6

| Nucleus | $J_i \rightarrow J_f$ | $T_i \rightarrow T_f$ | Correlation | Value ($\times 10^{-3}$) | Final State ($\times 10^{-3}$) |
|---|---|---|---|---|---|
| $n$ | $\frac{1}{2} \rightarrow \frac{1}{2}$ | $\frac{1}{2} \rightarrow \frac{1}{2}$ | $D\hat{J} \cdot (\hat{p}_e \times \hat{p}_\nu)$ | $1.1 \pm 1.7$ [21] | 0.01 |
| $^{19}$Ne | $\frac{1}{2} \rightarrow \frac{1}{2}$ | $\frac{1}{2} \rightarrow \frac{1}{2}$ | $D\hat{J} \cdot (\hat{p}_e \times \hat{p}_\nu)$ | $0.4 \pm 0.8$ [22] | 0.2 |
| $^{19}$Ne | $\frac{1}{2} \rightarrow \frac{1}{2}$ | $\frac{1}{2} \rightarrow \frac{1}{2}$ | $R\hat{\sigma}_e \cdot (\hat{J} \times \hat{p}_e)$ | $-79 \pm 53$ [23] | 1 |
| $^{8}$Li | $2 \rightarrow 2$ | $1 \rightarrow 0$ | $R\hat{\sigma}_e \cdot (\hat{J} \times \hat{p}_e)$ | $4 \pm 14$ [24] | $\leq 1$ |
| $^{58}$Co | $2 \rightarrow 2$ | $2 \rightarrow 3$ | $E_1(\hat{J} \cdot \hat{k})(\hat{J} \cdot \hat{p} \times \hat{k})$ | $130 \pm 300$ [25] | N/A |
| $^{52}$Mn | $6 \rightarrow 6$ | $1 \rightarrow 2$ | $E_1(\hat{J} \cdot \hat{k})(\hat{J} \cdot \hat{p} \times \hat{k})$ | $90 \pm 160$ [26] | N/A |
| $^{56}$Co | $4 \rightarrow 4$ | $1 \rightarrow 2$ | $E_1(\hat{J} \cdot \hat{k})(\hat{J} \cdot \hat{p} \times \hat{k})$ | $-11 \pm 22$ [27] | $\sim 0.1$ |

Table 1.1: Tests of $T$ violation in nuclear beta-decay. In the above, $\hat{J}$ refers to the initial nuclear spin. N/A indicates that the final state calculation is not available.

Both of these experiments are sensitive to $T$ invariance violation arising from a non-zero phase between the vector and axial vector couplings[28]. These experiments are primarily sensitive to "allowed" terms in the beta-decay interaction.

Another $T$ violating correlation studied in nuclear beta-decay is

$$R\hat{\sigma}_e \cdot (\hat{J} \times \hat{p}_e) \tag{1.8}$$

where $\hat{\sigma}_e$ is the spin of the electron or positron emitted in the decay and $\hat{J}$ is the initial nuclear spin. Unlike the $D$ correlation, the $R$ correlation is both $T$ and $P$ odd. In both of the $R$ correlation experiments listed in Table 1.1, the transverse electron (positron) spin was measured using large angle Mott scattering. Neither experiment reported evidence for $T$ invariance violation.

Finally, there are the $E_1$ measurements where the beta-decays of interest are to an excited state in the daughter nuclei. The gamma radiation emitted from the excited state is detected in lieu of detecting the recoiling daughter or the electron polarization. The $E_1$ correlation is both $T$ and $P$ odd and is given by

$$E_1(\hat{J} \cdot \hat{k})(\hat{J} \cdot \hat{p} \times \hat{k}). \tag{1.9}$$

where $\hat{J}$, $\hat{p}$, and $\hat{k}$ are the initial nuclear spin, positron and photon momentum. The limits obtained from $E_1$ measurements are less stringent than those obtained from $D$ measurements. However, the decays studied in $E_1$ measurements provide a complimentary test of $T$ violation. Since they occur outside of an isospin multiplet (unlike the $n$ or $^{19}$Ne), there is no requirement that the dominant decay terms be first class. Therefore, these experiments may be sensitive to $T$ violation arising from second class currents which are relatively suppressed in the allowed decays. This is discussed in greater detail in Section 2.2.

## 1.3 Outline of the Experiment

The decay scheme of $^{56}$Co is shown in Fig 1.1. The decay proceeds from an isospin state $T = 1$ with spin-parity $J^\pi = 4^+$ to an excited state of $^{56}$Fe with $T = 2$, $J^\pi = 4^+$ by positron emission. The normal selection rules for Fermi transitions ($\Delta T = 0, \Delta J = 0$) forbid this decay, but it is an allowed Gamow-Teller transition ($\Delta T = 0$ or 1, $\Delta J = 0$ or 1, but $0 \nrightarrow 0$). The $ft$ value for the decay is large, with $\log ft = 8.62$. For this reason, the decay is known as an isospin hindered decay.

Despite the fact that the Fermi transition is forbidden, measurements that are sensitive to the ratio of Fermi to Gamow-Teller matrix elements have shown it to be non-zero. The ratio, $y = C_V M_F / C_A M_{GT}$, can be determined through measurements of the beta-asymmetry $A$[29] as well as measurements of the beta-gamma circular polarization $A_{CP}$[30][31]. An average of these measurements yields $y = -0.095 \pm 0.005$ which indicates a significant, non-zero Fermi matrix element. The origin of this non-zero vector matrix element can be explained through a breakdown of isospin symmetry or possibly through a contribution of second class currents which, unlike first class vector currents, can connect states of different isospin[32]. If the underlying mechanism for $T$ violation is in second class currents, $^{56}$Co provides an ideal test.

The particular decay correlation investigated is $E_1(\hat{J} \cdot \hat{k})(\hat{J} \cdot \hat{p} \times \hat{k})$, where $\hat{J}$ is the initial nuclear spin, $\hat{p}$ is the beta momentum and $\hat{k}$ is momentum of either gamma-ray following the beta-decay. This measurement differs experimentally from the $D$ correlation of Equation 1.7 in two significant ways. First, a measurement of $E_1$ requires only nuclear alignment rather than polarization. This is evident since $\hat{J}$ appears twice in the correlation. A second difference is the absence of the neutrino momentum in the $E_1$ correlation. Of course, actual measurements of $D$ do not require neutrino detection, but rather the detection of a low energy recoil ion. In the case of the $E_1$ correlation, the gamma-ray momentum is detected in lieu of the recoil ion. The $\sim 1$ MeV gamma-rays following the beta-decay of $^{56}$Co are far easier to detect than the $\sim 100$ eV recoil ions.

In this work, the necessary nuclear alignment is achieved through low temperature nuclear orientation. The $^{56}$Co is implanted into a natural single crystal Co host that provides
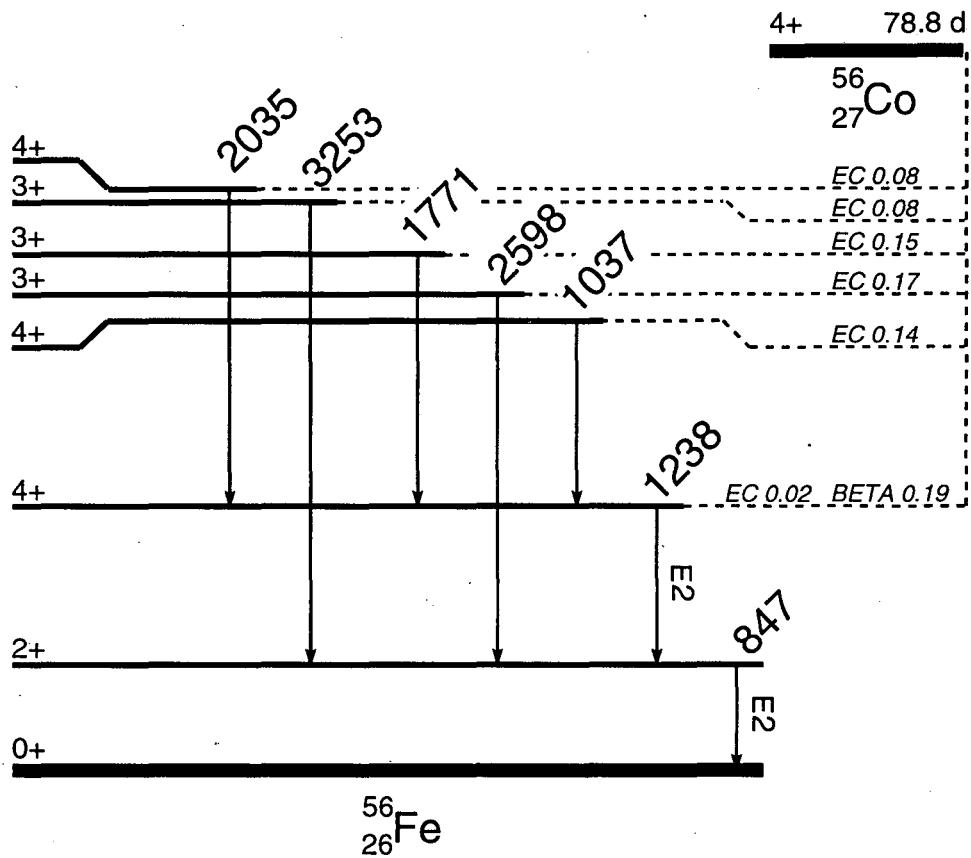
Figure 1.1: Partial decay scheme of $^{56}$Co.

a strong hyperfine field to align the nuclei. When cooled to mK temperatures with a $^3$He-$^4$He dilution refrigerator, this magnetic field produces significant nuclear alignment. Beta particles from the decays are detected with a silicon detector at mK temperatures and the subsequent gamma radiation is detected with NaI($Tl$) detectors at room temperature. This experiment was designed to improve upon the previous measurement[27] where a limit of $E_1 = -0.011 \pm 0.022$ was achieved.

# Chapter 2

# Theory

## 2.1 Time Reversal Invariance

The assertion of $T$ invariance requires that the physical laws be invariant under a transformation $t \to -t$. An common explanation of $T$ conservation considers a film of some physical process. In this case, the statement of $T$ conservation requires that the physical laws deduced by studying the process recorded on the film be the same independent of the direction the film is played. If the deduced laws depend upon the film direction, then $T$ conservation is violated. For example, consider tracing the path of a ball thrown by Jack to Jill. By measuring the velocity and position of the ball, it is possible to deduce the physical laws of motion. If the film was run backwards, the ball would appear to travel from Jill to Jack, but the measurements would reveal the identical physical laws. This is a demonstration of $T$ invariance.

This "film based" explanation is often confused with the idea that the *likelihood* of the forward and backward process should be the same. For example, possessed with Galilean curiousity, one might record the dropping of different bottles of wine from the top of the Tower of Pisa. Of course the bottles would fall, break, and spread wine all over the stones below. An audience viewing the film in reverse would see the reassembly of bottle and wine and obviously doubt the likelihood of this process. In fact, they would know the film was run in reverse. However, if the audience was only trying to determine the underlying
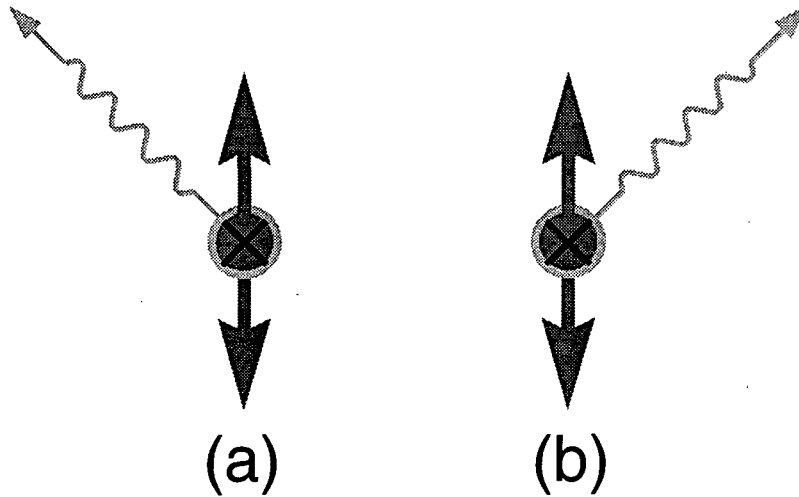
$$(\hat{J} \cdot \hat{k})(\hat{J} \cdot \hat{p} \times \hat{k}) \quad \rightarrow \quad -(\hat{J} \cdot \hat{k})(\hat{J} \cdot \hat{p} \times \hat{k})$$

Figure 2.1: Illustration of $E_1$ correlation under reflection of gamma-ray momentum through plane defined by nuclear spin and beta momentum. The bi-directional vertical arrow represents the nuclear alignment and the beta momentum is into the page.

physical laws of motion, their conclusions would be the same as if the film was run in the forward direction. The difference lies in the initial conditions. In the case of the bottle being dropped from the tower, the initial condition is the intact bottle at rest at some height. In the reverse process, the initial conditions are exceedingly more complicated. The droplets of wine and shards of class must be projected back toward a central area where they will assemble into the intact bottle of wine. Establishing this initial condition is a realistic impossibility, but if the conditions were met, the reassembly of bottle and wine would take place. That this is unlikely is not a statement of $T$ violation.

In decay experiments, tests of $T$ violation are performed by searching for $T$ odd correlations in the decay products. In the case of $^{56}$Co, the correlation is

$$E_1(\hat{J} \cdot \hat{k})(\hat{J} \cdot \hat{p} \times \hat{k}), \tag{2.1}$$

The transformation of $\hat{J}$ under $T$ is the same as for a classical angular momentum $\vec{L} = \vec{r} \times \vec{p}$ and hence $\hat{J} \rightarrow -\hat{J}$. The beta and gamma-ray momenta, $\hat{p}$ and $\hat{k}$ also change sign under

$T$ and therefore the entire correlation is $T$ odd. In Figure 2.1, two possible decays are illustrated which have a different sign according to the $E_1$ correlation. If $E_1$ is zero, both decay modes (a) and (b) are equally probable. If $E_1$ is non-zero, either mode (a) or (b) will be preferred. Experimentally, this is tested by comparing the number of coincidences observed in mode (a) to the number in mode (b).

How does the decay correlation relate to running the process backwards? To be sure, a decay correlation is not a comparison between the forward and backward process. To understand the relationship, consider the transition amplitude to first order[33]

$$\mathcal{M} \propto < \beta(p_2, s_2)|\mathcal{T}|\alpha(p_1, s_1) >, \qquad (2.2)$$

where $\mathcal{T}$ is the transition operator connecting the initial and final states. The terms $p_i, s_i$ indicate the momenta and spin of the initial and final states. The time reversed amplitude is then given by

$$\mathcal{M}' \propto < \alpha(-p_2, -s_2)|\mathcal{T}|\beta(-p_1, -s_1) >, \qquad (2.3)$$

where the initial and final states have been exchanged and the spins and momenta have been transformed according to $T$. Now, a strict comparison of the forward and backward process would require testing the equality $\mathcal{M} = \mathcal{M}'$. However, this requires running the decay in reverse. Fortunately, the practical impossibility of reversing the decay can be avoided if $\mathcal{T}$ is hermitian. With $\mathcal{T} = \mathcal{T}^\dagger$,

$$\mathcal{M}'^* \propto (< \alpha(-p_2, -s_2)|\mathcal{T}|\beta(-p_1, -s_1) >)^* = < \beta(-p_2, -s_2)|\mathcal{T}|\alpha(-p_1, -s_1) > . \qquad (2.4)$$

So that the effect of complex conjugation on the time reversed amplitude $\mathcal{M}'$ is to reverse initial and final states again without changing the spins or momenta. Now, the right hand side of Equation 2.4 is identical to Equation 2.2 excepting the signs of the spins and momenta. The condition of time reversal invariance can now be expressed as $\mathcal{M} = \mathcal{M}'^*$. To test this equality, consider Figure 2.1. Assume that $\mathcal{M}$ is associated with part (a) of the figure. Changing the signs of the spins and momenta in (a), followed by a rotation of 180°

14

in the plane defined by the spin and the beta momentum, yields the decay pattern shown in (b). Assuming rotational invariance, the process shown in Figure 2.1 (b) can then be identified with $\mathcal{M}'^*$. Now, a non-zero value of $E_1$ will cause a preference for (a) or (b) and therefore $\mathcal{M} \neq \mathcal{M}'^*$, indicating $T$ invariance violation.

Clearly, the essential underlying assumption in this argument is that the transition operator $\mathcal{T}$ is hermitian. While this is an appropriate statement to first order, the hermiticity of $\mathcal{T}$ fails when secondary interactions, known as final state effects, are included. The final state effects, which in the case of nuclear beta-decay are due to the electromagnetic interaction, are $T$ conserving. Therefore, in the case of $E_1$, the measured quantity is

$$E_1 = E_1^{TRV} + E_1^{fs}, \qquad (2.5)$$

where $E_1^{TRV}$ is the $T$ violating portion and $E_1^{fs}$ is the $T$ conserving contribution due to final state effects. The significance of final state effects in correlation measurements has been seen in the decay

$$\Lambda \rightarrow p\pi \qquad (2.6)$$

where a non-zero value of a $T$ violating correlation,

$$B(\hat{J}_\Lambda \times \hat{J}_p) \cdot \hat{p}_\pi \qquad (2.7)$$

has been observed[17]. The observation, $B = 0.10 \pm 0.07$, is consistent with the contribution expected from final state interactions. In this decay, the final state interactions are due to a strong interaction between the outgoing pion and proton. For this reason, the effect is significantly larger than the equivalent electromagnetic effects in nuclear beta-decay.

## 2.2  Nuclear Beta Decay

The beta decay transition amplitude for a single nucleon is given by the product of hadronic and leptonic terms

$$\mathcal{M} = \frac{G_V}{\sqrt{2}} \cos \theta_C < A|J_\mu^W|B > l^\mu \qquad (2.8)$$

15

where $J_\mu^W$ is the weak hadronic current and $B$, $A$ represent the final and initial nuclear states. The term $l^\mu$ is pure $V - A$ and is given by

$$l^\mu = \bar{u}(k_1)\gamma^\mu(1 + \gamma_5)u(k_2). \tag{2.9}$$

Now, in the absence of strong interactions, $J_\mu^W$ will simply take a form similar to the leptonic current with $V$ and $A$ terms. With the strong interaction *turned on*[33], there are additional induced terms, that have no weak leptonic analogue,

$$< B|J_\mu^W|A > = \bar{u}(p_1)\left[f_1(q^2)\gamma_\mu + if_2(q^2)\sigma_{\mu\nu}q^\nu + f_3(q^2)q_\mu \right. \tag{2.10}$$
$$\left. + g_1(q^2)\gamma_\mu\gamma_5 + ig_2(q^2)\sigma_{\mu\nu}q^\nu\gamma_5 + g_3(q^2)q_\mu\gamma_5\right]u(p_2)$$

where the various form factors $f$ and $g$ depend on the momentum transfer $q = p_1 - p_2$ in the decay.

The form factors in Equation 2.11 can be classified according to their transformation properties under $G$-parity. A $G$-parity transformation is the combined transformation of $C$ and a rotation in isospin space such that

$$G = Ce^{i\pi T_2}. \tag{2.11}$$

Since the strong interaction is invariant under both $C$ and isospin transformations, the properties of the strong induced vector and induced axial vector terms in Equation 2.11 should exhibit the same behavior under a $G$-parity transformation as the vector and axial vector terms before the strong interaction. In other words, the strong interaction, being invariant under $G$-parity, should not effect the transformation properties of the vector and axial vector current in their pure $V$ and $A$ forms. Currents that obey this simple argument are labeled first class and those that do not are denoted second class. Under a $G$-parity transformation, the various vector terms in Equation 2.11 transform as

$$\bar{u}(p_1)f_1(q^2)\gamma_\mu u(p_2) \overset{G}{\to} \bar{u}(p_1)f_1(q^2)\gamma_\mu u(p_2) \tag{2.12}$$

$$\bar{u}(p_1)f_2(q^2)\sigma_{\mu\nu}q^{\nu}u(p_2) \xrightarrow{G} \bar{u}(p_1)f_2(q^2)\sigma_{\mu\nu}q^{\nu}u(p_2) \tag{2.13}$$

$$\bar{u}(p_1)f_3(q^2)q_{\mu}u(p_2) \xrightarrow{G} -\bar{u}(p_1)f_3(q^2)q_{\mu}u(p_2) \tag{2.14}$$

and the axial vector terms as

$$\bar{u}(p_1)g_1(q^2)\gamma_{\mu}\gamma_5 u(p_2) \xrightarrow{G} -\bar{u}(p_1)g_1(q^2)\gamma_{\mu}\gamma_5 u(p_2) \tag{2.15}$$

$$\bar{u}(p_1)g_2(q^2)\sigma_{\mu\nu}q^{\nu}\gamma_5 u(p_2) \xrightarrow{G} \bar{u}(p_1)g_2(q^2)\sigma_{\mu\nu}q^{\nu}\gamma_5 u(p_2) \tag{2.16}$$

$$\bar{u}(p_1)g_3(q^2)q_{\mu}\gamma_5 u(p_2) \xrightarrow{G} -\bar{u}(p_1)g_3(q^2)q_{\mu}\gamma_5 u(p_2) \tag{2.17}$$

For the vector terms, the transformation of the $f_1$ term defines a first class current. Based on this, $f_2$ is first class and $f_3$ is second class. With the axial vector terms, $g_1$ defines first class and therefore the $g_2$ term is second class while $g_3$ is first class.

To move from the description of a single nucleon to a $^{56}$Co nucleus, it is necessary to adopt a notation that accommodates the nuclear complexity. In addition, for a hindered decay such as $^{56}$Co, it is also desirable to maintain the recoil order terms that are neglected in the allowed approximation. For these reasons, the notation of Holstein[34] is used. For a single nucleon decay, this notation can be compared to Equation 2.11 to identify the following equalities

$$f_1(0) = a \tag{2.18}$$

$$f_2(0) = \frac{b-a}{\sqrt{3}(m_1+m_2)} \tag{2.19}$$

$$f_3(0) = \frac{e}{m_1+m_2} \tag{2.20}$$

$$g_1(0) = \frac{c}{\sqrt{3}} \tag{2.21}$$

$$g_2(0) = \frac{d}{\sqrt{3}(m_1+m_2)} \tag{2.22}$$

$$\tag{2.23}$$

The terms $a$ and $c$ clearly correspond to the familiar Fermi and Gamow-Teller matrix elements. The matrix element $b$ is associated with weak magnetism. In this formalism, $b$ includes both the "normal" magnetic moment and the "anomalous" portion which arises

17

from the tensor term proportional to $f_2$.

The next term, $e$, is predicted to vanish according to the conserved vector current (CVC) hypothesis. This is apparent if one considers the electromagnetic interaction between two protons

$$< B|J_\mu^{EM}|A > = \bar{u}(p_1)\left[F_1(q^2)\gamma_\mu + iF_2(q^2)\sigma_{\mu\nu}q^\nu + F_3(q^2)q_\mu\right]u(p_2). \qquad (2.24)$$

where the form factors $F_1$ and $F_2$ are related to charge and magnetic moments of the interacting nucleons. Now, since the electromagnetic current obeys $\partial_\mu J_\mu^{EM} = 0$, the term $F_3$ must equal zero. The physical interpretation of this is that the proton charge, $+e$, is not renormalized by the strong interaction. Since the CVC hypothesis relates the weak vector current to the isovector portion of the electromagnetic current through an isospin rotation[35], it follows that the analogous term in the vector portion of Equation 2.11, $f_3 = e/(m_1 + m_2)$, is also zero.

In this notation, the induced tensor term $d$ is associated with the second class term $g_2$. For decays within an isospin multiplet (e.g. the single nucleon decay), $d$ is purely second class. For decays outside of a multiplet, there is a mixed contribution of first and second class terms in $d$. This term is neglected in the allowed approximation. However, $d$ is included in the discussion of $E_1$, since it is possible that it is relatively enhanced in the hindered decay.

Given this formalism, and assuming the validity of CVC, the $T$ violating portion of $E_1$ is given by[36]

$$E_1^{TRV} \simeq \frac{2}{|a|^2 + |c|^2}Im\left[a^*\left(c - \frac{1}{3}\frac{E_0 - E}{M}d\right)\right] \qquad (2.25)$$

where $E_0$ is total available decay energy and $E$ is the beta energy. Averaging Equation 2.25 over observed beta energies yields

$$\bar{E}_1^{TRV} \simeq \frac{2}{|a|^2 + |c|^2}Im\left[a^*\left(c - \frac{E_0}{6M}d\right)\right] \qquad (2.26)$$

In both of these expressions, it is clear that the $T$ violating effect arises when $a$, $c$, and $d$ are not relatively real. The hindrance strategy[32][37] suggests looking at decays where $(|a|^2 + |c|^2)$ is small to enhance the $T$ violating signal. In particular, it was pointed out[32]

that a hindered decay could have greater sensitivity to $T$ violation arising from second class currents than allowed decays such as the neutron and $^{19}$Ne. The allowed decays are dominated by first class terms, while in a hindered decay such as $^{56}$Co, the first class terms $a$ and $c$ are suppressed. If the mechanism that hinders the first class terms $a$ and $c$ does not also hinder the second class contribution to $d$, then a relative enhancement of a $T$ violating effect could occur.

The $T$ allowed contribution to $E_1$ is given by

$$\bar{E}_1^{fs} \simeq \frac{\alpha Z E^2}{2Mp(|a|^2 + |c|^2)} Re \left\{ a^* \left[ (c + b - d) - \frac{m_e^2}{E^2}(3c + b + d) \right] \right\} \qquad (2.27)$$

where $Z$ is the atomic number and $E$, $p$ are the energy and momentum of the beta. Based on previous measurements of $^{56}$Co[29][30][27], this effect is estimated to be $E_1^{fs} \approx 10^{-4}$. This is more than an order of magnitude smaller than the experimental sensitivity and hence is not considered in the analysis.

The full decay distribution for $^{56}$Co, including both the $T$ violating correlation and the normal, $T$ allowed gamma-ray anisotropy is given by[38][36]

$$
\begin{aligned}
W(\hat{J}, \hat{p}, \hat{k}, T) \quad \propto \quad & 1 - 1.3431 \frac{(\frac{17}{20} + y^2)}{(1 + y^2)} R_2(T) P_2(\hat{J} \cdot \hat{k}) \qquad (2.28) \\
& - \quad 0.9132 \frac{(\frac{1}{2} + y^2)}{(1 + y^2)} R_4(T) P_4(\hat{J} \cdot \hat{k}) \\
& + \quad E_1 \frac{v}{c} \frac{1}{\sqrt{80}} \left[ 1.3431 \frac{(\frac{17}{20} + y^2)}{(1 + y^2)} R_2(T) P_2'(\hat{J} \cdot \hat{k}) \right. \\
& + \quad 0.9132 \frac{(\frac{1}{2} + y^2)}{(1 + y^2)} R_4(T) P_4'(\hat{J} \cdot \hat{k}) \left. \right] (\hat{J} \cdot \hat{p} \times \hat{k}),
\end{aligned}
$$

where $\hat{J}$, $\hat{p}$ and $\hat{k}$ are the initial nuclear spin, beta momentum and gamma-ray momentum unit vectors. The ratio of Fermi to Gamow-Teller matrix elements is defined by

$$y = C_V M_F / C_A M_{GT}. \qquad (2.29)$$

The statistical tensors $R_2$ and $R_4$ depend on the temperature and reflect the degree of nuclear orientation. This derivation assumes that the excited daughter states following the

beta-decay (see Figure 1.1) are short lived so that there is no reorientation of the nuclear spin before emission of the gamma-ray. For $^{56}Fe^*$ this is a good approximation since the lifetimes of these states is less than 0.6 ps for the $4^+$ state and 6 ps for the $2^+$ state[39]. In the case of $^{56}Co$ in single crystal hcp Co, the effective magnetic field is $H_{eff} = -22.7$ T[40] and the corresponding precision times are on the order of $\sim 1$ ns. Therefore, the emitted gamma-rays are an accurate reflection of the nuclear spin of the daughter. Furthermore, the same distribution is valid for either gamma-ray following the positron decay. This is because the gamma-cascade is a stretched electric quadrupole transition ($4^+ \rightarrow 2^+ \rightarrow 0^+$) in which no deorientation occurs when passing through the $2^+$ state[41][42].

The first two lines of Equation 2.28 reflects the normal gamma-ray anisotropy which arises from the nuclear alignment. These terms are proportional to even powers of $\cos\theta$ where $\theta$ is the angle between the gamma-ray momentum and nuclear spin. Hence, in Figure 2.1, the contribution of these $T$ allowed terms is the same for both (a) and (b). The third and fourth lines of Equation 2.28, contain the $T$ odd correlation $E_1(\hat{J} \cdot \hat{k})(\hat{J} \cdot \hat{p} \times \hat{k})$. In a simplified geometry, this correlation is proportional to $\sin 2\theta$ which changes sign under the reflection $\theta \rightarrow -\theta$ as shown in Figure 2.1.

In order to compare $E_1$ to the results measured by $D$ correlation experiments, it is convenient to assume that the $T$ violation is arising from a single complex phase between two of the nuclear form factors. For the neutron and $^{19}Ne$, the $D$ coefficient is interpreted as arising from an interference between $a$ and $c$. For $^{56}Co$, the assumption that the $T$ violation is arising from an interference between $a$ and $c$ is subject to additional assumptions. After all, one motivation for choosing the isospin hindered decay is to consider the possibility that the $T$ violation is arising from an interference with the second class term $d$. With the allowed decay experiments, the phase, $\phi$ is related to $D$ by

$$D = \frac{2\sqrt{3}|y| \sin\phi}{1 + 9|y|^2} \tag{2.30}$$

with $y$ being defined as in Equation 2.29.

To determine $\sin\phi$, the result of a $D$ correlation measurement is combined with an asymmetry measurement that depends on $y$ and $\cos\phi$. By convention, $\phi$ is chosen to

20

| Correlation | Value | $y$ | Reference |
|---|---|---|---|
| $A_{CP}$ | $0.002 \pm 0.010$ | $-0.108 \pm 0.013$ | [31] |
| $A_{CP}$ | $0.017 \pm 0.013$ | $-0.130 \pm 0.020$ | [30] |
| $A$ | $0.359 \pm 0.009$ | $-0.091 \pm 0.005$ | [29] |

Table 2.1: Determination of $y = C_V M_F / C_A M_{GT}$ for $^{56}$Co through beta asymmetry and beta gamma circular polarization measurements.

be near 180°. Time reversal invariance then requires $\phi = 180°$. For $E_1$, the analogous expression is[37]

$$E_1 = \frac{2|y| \sin \phi}{(1 + |y|^2)} \tag{2.31}$$

A measurement of $E_1$ is combined with measurements of $|y|$ determined through beta-asymmetry and beta-gamma circular polarization experiments to extract $\phi$. A summary of these measurements is shown in Table 2.1. In $^{56}$Co, the beta-asymmetry depends on $|y|$ and $\cos \phi$ in the following manner

$$A = \frac{1}{1 + |y|^2} \left[ \frac{1}{5} + \frac{4}{\sqrt{5}} |y| \cos \phi \right] . \tag{2.32}$$

The beta-gamma circular polarization is given by

$$A_{CP} = \frac{\sqrt{3}}{6} \frac{1}{1 + |y|^2} \left[ \frac{2}{\sqrt{5}} + 4|y| \cos \phi \right] F_1(2, 2, 4, 4), \tag{2.33}$$

where the coefficient $F_1$ depends upon the multipole order of the $\gamma$-ray transition as well as the initial and final state nuclear spins. The measurement of $A$[29] and an average of recent measurements of $A_{CP}$[30][31] along with the single measurement of $E_1$[27] are shown as a function of $y$ and $\phi$ in Figure 2.2. At $\phi = 180°$, there is a slight disagreement between the $\beta$-asymmetry measurement and the $\beta - \gamma$ circular polarization measurements. Since these measurements have a different functional dependence on $\phi$ and $y$, it is possible for
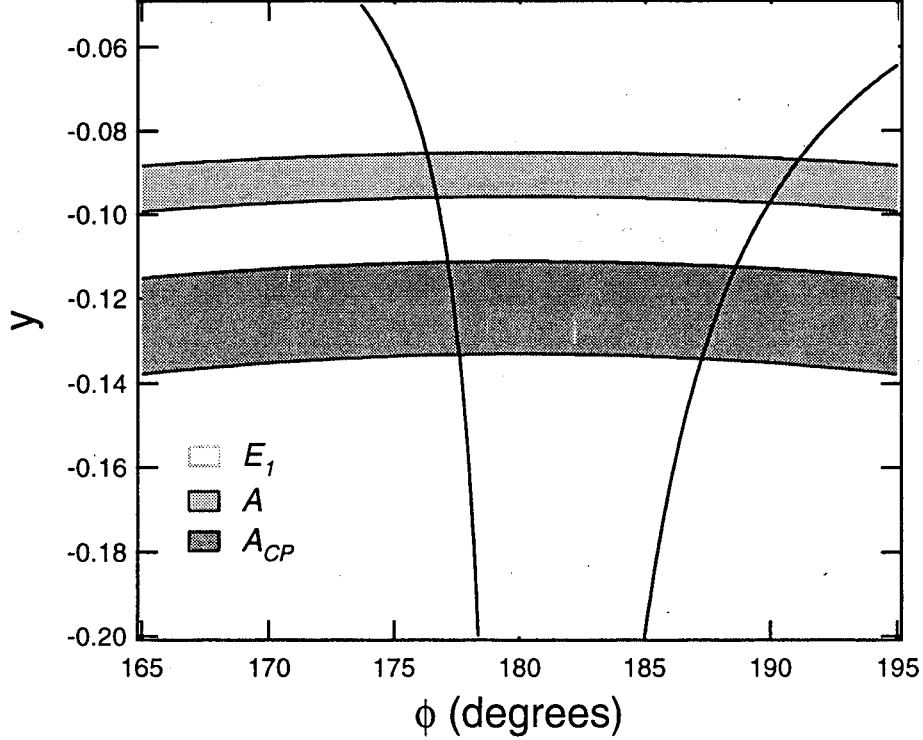
Figure 2.2: Determination of $\phi$ and $y$ for $^{56}$Co based on measurements of $E_1$[27], the $\beta$-asymmetry $A$[29] and the $\beta - \gamma$ circular polarization $A_{CP}$[30][31]. Error bands are $1\sigma$.

these results to agree at other values of $\phi$. In fact, if the $E_1$ measurement is ignored so that $\phi$ is not constrained to be near 180°, then two other solutions are possible at $\phi \approx 110°$ or $\phi \approx 250°$. These solutions yield agreement between the $A$ and $A_{CP}$ measurements, but indicate significant $T$ violation inconsistent with the result for $E_1$[27]. For this reason, a simple average of the $A$ and $A_{CP}$ results is used to determine $y$. The resulting average value is $y = -0.095 \pm 0.005$ at $\phi = 180°$. Using this value in Equation 2.31, the current limit on $E_1 = -0.011 \pm 0.022$ yields $\phi = 183 \pm 6°$. The equivalent measurement in neutron decay yields $\phi = 180.07 \pm 0.18°$[21][43].

# Chapter 3

# The Experimental Method

## 3.1  Nuclear Orientation

This experiment utilizes low temperature nuclear orientation to achieve alignment of the $^{56}$Co nuclei. Nuclear orientation is commonly used for low temperature thermometry with $^{60}$Co(Co-hcp). In general, this technique involves the implantation of nuclei into substitutional sites of a ferromagnetic lattice. The implanted nuclei experience an effective magnetic field arising from a hyperfine interaction with the host electrons. In cases where the orbital electron wave functions have significant density near the nuclei, this effective field can reach values of several Tesla. However, the orientation of this field depends upon the magnetic domains of the ferromagnet.

Magnetic domains arise through the significant exchange interaction between the orbital $d$ or $f$ shell electrons in ferromagnets such as Fe, Co and Ni. The domain structure is determined by whatever configuration minimizes the total potential energy and this configuration differs with different ferromagnetic crystals. In Figure 3.1, the domain structures for unmagnetized single crystal cobalt and iron are shown. Single crystal Co, unlike Fe, has domains that are aligned along a single axis. In cobalt, which is a hexagonal close packed (hcp) structure, this single orientation axis is along the hexagonal axis. In iron, which is body centered cubic (bcc), there is a three-fold symmetry along the cube edges and this leads to three possible domain axes. In studies that require nuclear alignment, a Co host
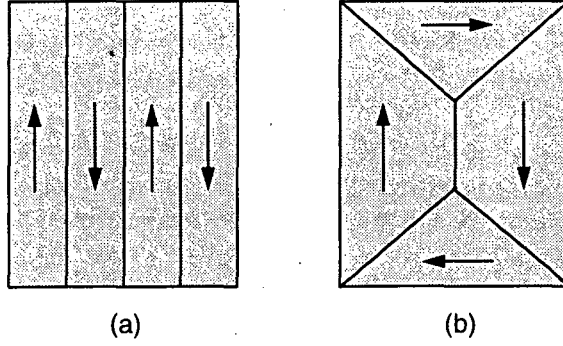
Figure 3.1: Domain structure in (a) unmagnetized single crystal Co and (b) unmagnetized single crystal Fe.

can be used without application of an external magnetic field. In Fe and other ferromagnets, a external field must be applied to make a single domain axis energetically favorable.

In the case of Co, the domain width has been found to range from 10 to 60 $\mu$m[44]. Since there are a finite number of domains, the possibility exists that an unpaired domain would result in some residual polarization. A significant polarization can lead to undesirable asymmetries due to the well known parity violation of the weak interaction. With a polarized sample, an additional term of odd rank must be included in Equation 2.28. This term takes the form of $R_1[3(\hat{p} \cdot \hat{k})(\hat{J} \cdot \hat{k}) - (\hat{p} \cdot \hat{J})]$. Combined with some non-uniformity in the beta detector, this odd rank term can give rise to a false asymmetry that is indistinguishable from the $T$ violating asymmetry. For the crystal samples used in this work, the range of domain sizes suggests a small non-cancellation of the polarization at a level of 0.3 to 2 percent. The largest resulting false asymmetry, assuming beta detector variations as large as 15 percent, is less than $10^{-4}$. However, if an Fe host were used, the domains would be completely polarized by the external field, and the residual asymmetry would be 50 times larger. Also, the fringe components of this external field could cause a deflection of the beta particles which yields an effective non-uniformity in the beta detector.

In the presence of a magnetic field, the energy of a particular nuclear level is given by

$$E_m = -(\mu B_{eff})m \tag{3.1}$$

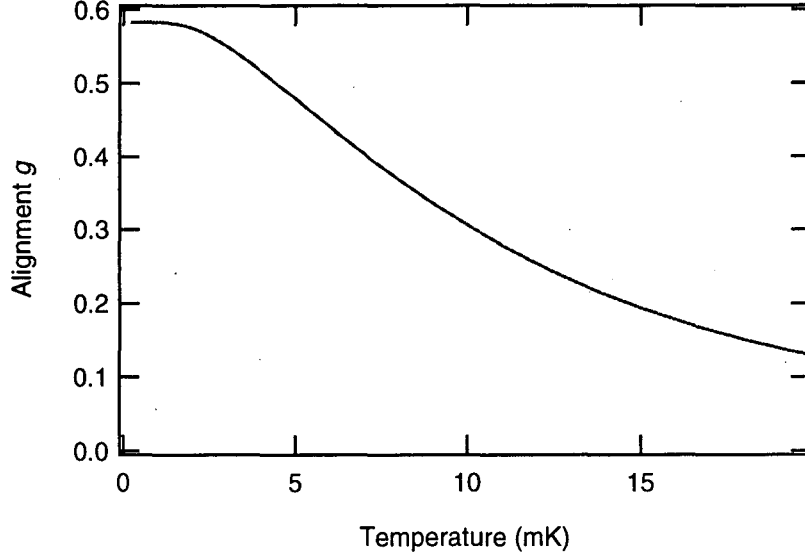where $m$ is the magnetic quantum number and $\mu$ the nuclear magneton. Given an ensemble

24

Figure 3.2: $^{56}$Co(Co-hcp) nuclear alignment $g$ as a function of temperature.

of these nuclear spins in thermodynamic equilibrium at temperature $T$, the probability of,
a particular spin state $m$ is given by Boltzman factors which depend upon the ration of $\mu B$
to $kT$.

$$a_m = \frac{\exp(-E_m/kT)}{\sum_m \exp(-E_m/kT)} \tag{3.2}$$

Clearly, at temperatures where $kT \gg \mu B$, there will be little population difference between
the various nuclear substates. As temperatures are reduced to $kT \sim \mu B$, the lower energy
substates will be preferentially occupied and hence nuclear orientation occurs. For typical
values of $\mu \approx \mu_N$ and $B_{eff} \approx 20$ T, appreciable population differences between the magnetic
substates requires temperatures in the mK regime. The degree of nuclear alignment is
characterized by a parameter $g$ which is given by[45]

$$g = \frac{\sum a_m \frac{[m^2 - I(I+1)]}{3}}{I^2 \sum a_m} \tag{3.3}$$

where $I$ is the nuclear spin. The alignment parameter $g$, calculated for $^{56}$Co(Co-hcp), is
shown in Figure 3.2. The relevant parameters for $^{56}$Co(Co-hcp) are $\mu = 3.851\mu_N$[39] and
$B_{eff} = -22.7$ T[46].

The gamma-ray decay distribution from the oriented nuclei is given by

$$W(\theta) = \sum_{\lambda} R_\lambda(T) U_\lambda A_\lambda Q_\lambda P_\lambda(\cos\theta),$$

(3.4)

where $R_\lambda$ is the statistical tensor of the initial state that contains all of the temperature dependence. It is defined by

$$R_k = \sum_m (-1)^m C(JJk; m, -m) a(m),$$

(3.5)

where $C(JJk; m, -m)$ are Clebsch-Gordon coefficients and $a(m)$ is defined in Equation 3.2. In experiments where there is only nuclear alignment or, alternatively, only the gamma-ray direction (and not the beta direction) is observed, the sum in Equation 3.4 is over even values of $\lambda$. The additional terms, $U_\lambda$ and $A_\lambda$ are deorientation and angular distribution coefficients that give rise to the numerical factors in Equation 2.28. The correction for finite detector solid angle is expressed in $Q_\lambda$ and the angular dependence is contained in the Legendre polynomial $P_\lambda(\cos\theta)$. As noted previously, the deorientation coefficient, $U_\lambda$, is unity for the stretched electric quadrupole transition and therefore the 1238 and 847 keV gamma-rays following the beta decay of $^{56}$Co have the same angular distributions.

## 3.2  Design Criteria

This experiment was designed to improve upon the previous measurement[27] by increasing the sensitivity to $E_1$ as well as introducing new techniques to eliminate systematic uncertainties. Much of the design effort was focused on addressing the three challenges faced in the earlier work: refrigeration, detector coverage and sensitivity to detector asymmetries.

### 3.2.1  Refrigeration

The degree of refrigeration and its stability determine the average nuclear alignment and hence the experimental sensitivity to $E_1$. In the previous experimental effort, adiabatic demagnetization was used to cool the cobalt sample. This technique involved the pre-cooling

of a cerium magnesium nitrate (CMN) salt to 100 mK by means of a dilution refrigerator. After pre-cooling, the CMN salt was thermally isolated from the active refrigeration and a 1.2 T magnetic field was slowly demagnetized to yield a base temperature of 6 mK. With no active refrigeration, the residual heat leak, combined with the source activity, would cause this apparatus to warm up at a rate of 1 mK per day. As shown in Figure 3.2, the alignment $g$ is already decreased by half when the temperature warms from 6 mK to 13 mK. This gradual source warming limited the useful run length to about one week with an average temperature of $\approx 9$ mK. At 9 mK, the alignment parameter is reduced by 25 percent relative to the 6 mK base temperature. Based on this, two improvements in refrigeration were desired: (1) long term refrigerator stability that could support runs over 1 month long and (2) a lower average base temperature to increase the degree of nuclear alignment.

### 3.2.2 Detectors

Figure 3.3 illustrates the detector arrangement used in the previous experiment. For gamma-ray detection, three 13 cm × 10 cm NaI($Tl$) detectors were located 13 cm away, in the plane of the source as shown. A Si(Li) detector was placed directly below the source crystal for positron detection. To maximize sensitivity to the $E_1$ correlation, $(\hat{J}\cdot\hat{k})(\hat{J}\cdot\hat{p}\times\hat{k})$, two of the NaI($Tl$) were located at ± 45 degrees with respect to the crystal axis. In this configuration, a non-zero $E_1$ would be indicated by different beta-gamma coincident rates for these two NaI($Tl$) detectors. The third NaI($Tl$) detector, positioned along the c-axis, is insensitive to $E_1$ and was used to monitor the source temperature.

Increased detector coverage is obviously desirable for enhancing statistical precision. However, as the solid angle for each detector is increased, the lower angular resolution decreases and so too the sensitivity to any angular correlation. This effect is illustrated for $P_2(\hat{J}\cdot\hat{k})$, plotted as a function of detector solid angle in Figure 3.4. This dilution for $P_K$ is typically referred to as a solid angle correction factor $Q_K$, which is defined as

$$Q_K \equiv \frac{\int P_K(\hat{J}\cdot\hat{k})\varepsilon(\theta)d\Omega}{\int \varepsilon(\theta)d\Omega} \tag{3.6}$$

where the integration is performed over the face of the detector with the z-axis along the
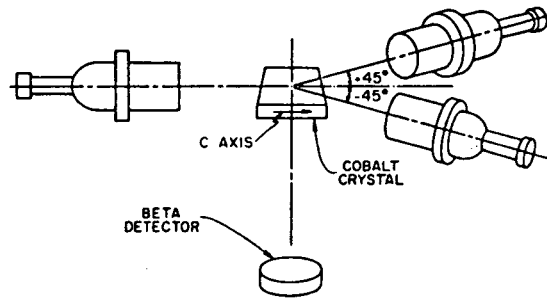
Figure 3.3: Detector arrangement used in reference [27].
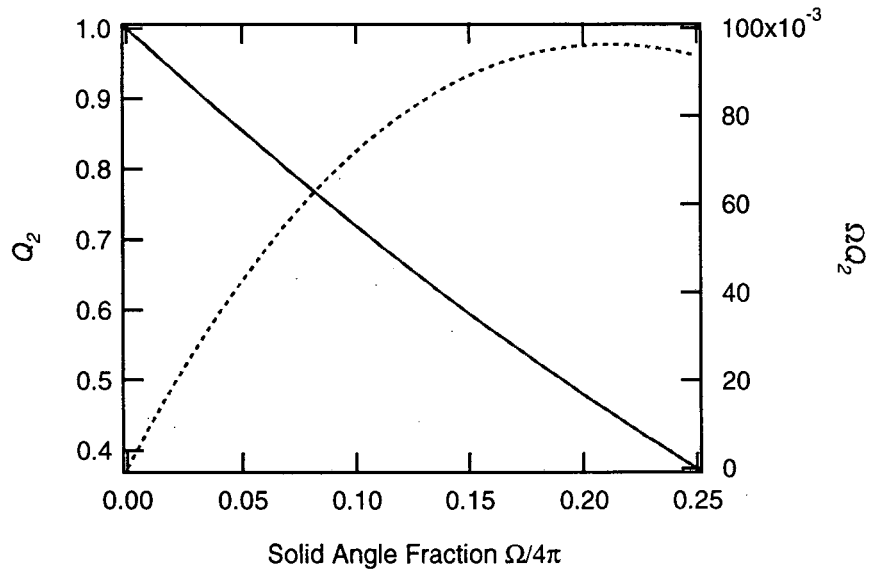


Solid Angle Fraction $\Omega/4\pi$

Figure 3.4: The solid line represents the solid angle correction factor $Q_2$ assuming uniform detector efficiency (left hand scale). The dashed line indicates the correction factor weighted by the solid angle (right hand scale).

cylindrical axis of the detector and the detector efficiency is given by $\varepsilon(\theta)$. Of course, the appropriate figure of merit for a statistics limited experiment is Equation 3.6 weighted by the solid angle itself. By weighting the solid angle correction in this fashion, the appropriate emphasis on event rate is attained. As shown in Figure 3.4, this figure of merit, $\Omega Q_2$, favors large solid angles over angular resolution for reasonable values of the detector solid angle. In the previous experiment, the NaI($Tl$) solid angle was less than 0.04 of $4\pi$. Therefore, significant sensitivity can be gained by simply increasing the detector solid angles.

To increase the detector solid angles, the detectors can simply be moved closer to the source. This is a cryogenic challenge since the NaI($Tl$) operate at room temperature and the Si(Li) detector is typically operated at 77 K. The gamma-rays following the decay of $^{56}$Co are energetic enough ($\approx 1$ MeV) to penetrate the surrounding heat shields and liquid helium dewar to escape the mK environment. So, the design objective for the gamma-ray detectors is to create a refrigerator and dewar that together minimize the distance and material between the mK environment and room temperature. This must be done under the constraint of maintaining acceptable boil-off rates of liquid helium.

To increase the solid angle of the beta detector is more challenging. The positrons emitted in the decay of $^{56}$Co ($Q \approx 1.46$ MeV) are not energetic enough to penetrate the surrounding materials and reach higher temperature regions of the refrigerator. Unfortunately, standard cold semiconductor detectors operate at liquid nitrogen temperatures which is more than 4 orders of magnitude warmer than the source. The previous experiment used a standard 1 cm$^2$ $\times$ 3 mm thick Si(Li) detector. To keep this detector operational, it was heated to a temperature of 70 K and shielded from the mK environment with several layers of aluminized mylar. To prevent this heated region from significantly raising the temperature, the detector was placed 2 cm away from the source. The resulting solid angle was less than 0.02 of $4\pi$. To improve upon this design requires either a larger beta detector or one that operates at lower temperatures. A larger detector, placed below the source crystal, requires the entire mK region to be larger than is practical. Therefore, significant improvement in the beta detector solid angle requires a detector that can operate at lower temperatures.

### 3.2.3 Systematic Uncertainties

To understand the sources of systematic uncertainty in this measurement, consider the detector arrangement of Figure 3.3. As asserted earlier, a non-zero value of $E_1$ will cause different beta-gamma coincident rates for the two NaI($Tl$) located at $\pm$ 45 degrees. Given this, one might construct the following simple ratio to measure $E_1$

$$E_1 \propto \frac{N_c^1 - N_c^2}{N_c^1 + N_c^2} \tag{3.7}$$

Where $N_c^1$ and $N_c^2$ represent beta-gamma coincidence events where either the 847 or 1238 keV gamma-ray was measured in detector 1 or 2 in coincidence with a positron in the beta detector. Detectors 1 and 2 are those located at $\pm$ 45 degrees to the c-axis. In the following discussion, it is assumed that only photopeak events, where the total gamma-ray energy is recorded, are considered. Ignoring several experimental details, a non-zero value of Equation 3.7 would indicate a non-zero $E_1$. Using the following definitions for the various terms in Equation 2.28

$$
\begin{aligned}
f(\theta, T) &\equiv 1.3431 \frac{(\frac{17}{20} + y^2)}{(1 + y^2)} R_2(T) P_2(\hat{J} \cdot \hat{k}) + 0.9132 \frac{(\frac{1}{2} + y^2)}{(1 + y^2)} R_4(T) P_4(\hat{J} \cdot \hat{k}) \quad (3.8)\\
g(\theta, T) &\equiv \frac{v}{c} \frac{1}{\sqrt{80}} \left[ 1.3431 \frac{(\frac{17}{20} + y^2)}{(1 + y^2)} R_2(T) P_2'(\hat{J} \cdot \hat{k}) \right. \\
&\quad + \left. 0.9132 \frac{(\frac{1}{2} + y^2)}{(1 + y^2)} R_4(T) P_4'(\hat{J} \cdot \hat{k}) \right] \times (\hat{J} \cdot \hat{p} \times \hat{k}),
\end{aligned}
$$

the angular distribution can be written as,

$$W(\theta, T) \propto 1 - f(\theta, T) + E_1 g(\theta, T). \tag{3.9}$$

Under reflection about the spin axis, $f(\theta) \to f(-\theta)$ and $g(\theta) \to -g(-\theta)$. Now, neglecting the finite solid angle corrections for simplicity, Equation 3.7 becomes

$$\frac{\epsilon_\beta \Omega_\beta \{\epsilon_1 \Omega_1 [1 - f(\theta_1, T) + E_1 g(\theta_1, T)] - \epsilon_2 \Omega_2 [1 - f(\theta_2, T) + E_1 g(\theta_2, T)]\}}{\epsilon_\beta \Omega_\beta \{\epsilon_1 \Omega_1 [1 - f(\theta_1, T) + E_1 g(\theta_1, T)] + \epsilon_2 \Omega_2 [1 - f(\theta_2, T) + E_1 g(\theta_2, T)]\}}. \tag{3.10}$$

When $E_1$ is identically zero, this becomes

$$\frac{\epsilon_1 \Omega_1 [1 - f(\theta_1, T)] - \epsilon_2 \Omega_2 [1 - f(\theta_2, T)]}{\epsilon_1 \Omega_1 [1 - f(\theta_1, T)] + \epsilon_2 \Omega_2 [1 - f(\theta_2, T)]}. \tag{3.11}$$

In these expressions $\epsilon$ and $\Omega$ represent the efficiency and solid angles for the two NaI($Tl$) and beta detectors. Clearly, Equation 3.10 can deviate from zero even if $E_1$ is identically zero because of differences between detector efficiencies or solid angles. Even if we assume that $\epsilon_1 = \epsilon_2$ and $\Omega_1 = \Omega_2$, with a zero value for $E_1$, we have

$$\frac{N_c^1 - N_c^2}{N_c^1 + N_c^2} = \frac{[f(\theta_1, T) - f(\theta_2, T)]}{[f(\theta_2, T) + f(\theta_1, T)]} \tag{3.12}$$

which is a purely systemmatic asymmetry. Now, if $f(\theta_1, T) \neq f(\theta_2, T)$, Equation 3.12 will still be non-zero. Since $f(\theta, T)$ is composed of even powers of $\cos \theta$, Equation 3.12 will be equal to zero provided that $\theta_1 = -\theta_2$. To achieve this condition, precise alignment of the NaI($Tl$) detectors relative to the nuclear spin axis is required.

Hence, there are two basic sources that contribute to a systematic, non-zero value of $E_1$. First, there are variations in detector efficiencies and solid angles. Since variations due to one or the other are not readily distinguishable, they are grouped together. The second source of systematic error is misalignment of the detectors relative to the nuclear spin axis. This can be caused by either imprecise mechanical alignment of the detectors relative to the crystal edge or an imperfectly cut crystal for which the crystal edge is not parallel to the c-axis. This misalignment is especially problematic because the resulting angular distribution, as shown schematically in Figure 3.5, is indistinguishable from that due to a non-zero $E_1$.

Both of these systematic effects were addressed in the previous work[27] by considering a slightly more complicated expression than that of Equation 3.7.

$$\Delta = \frac{N_c^1 - N_c^2}{N_c^1 + N_c^2} - \xi \frac{N_s^1 - N_s^2}{N_s^1 + N_s^2} \tag{3.13}$$

where $N_s^1$ and $N_s^2$ represent singles events in the two detectors. Since the singles events

31

θ = 0

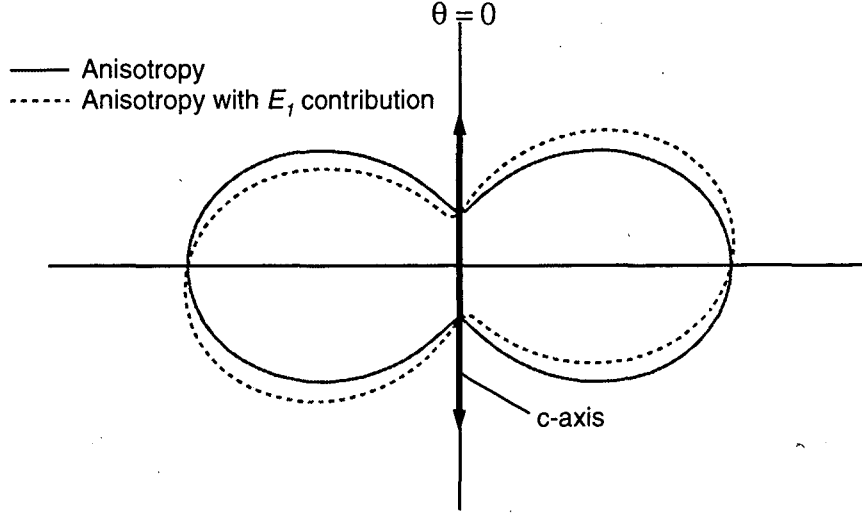——— Anisotropy
------ Anisotropy with $E_1$ contribution

c-axis

Figure 3.5: Gamma-ray anisotropy showing the effect of $E_1 = 0$ and $E_1 \neq 0$. Note that the $T$ violating asymmetry is similar to a rotation of the $T$ allowed anisotropy. Such a rotation occurs due to detector misalignment relative to the c-axis.

arise from decays where the beta is emitted in all possible directions, the difference in the singles event rates should be insensitive to $E_1$. This is because the $E_1$ correlation is odd in the beta momentum, and when integrated over all possible directions it will vanish. As seen in Figure 1.1, these singles events also arise from electron capture decays to higher levels in $^{56}$Fe and hence they do not have the same angular distribution as those gamma-rays emitted after the beta decay. For this reason, the singles anisotropy will be denoted by $h(\theta, T)$ to distinguish it from $f(\theta, T)$. Neglecting detector variations, and assuming that $E_1 g(\theta_1) \approx -E_1 g(\theta_2)$, Equation 3.13 can be expressed as

$$\frac{[-f(\theta_1, T) + f(\theta_2, T) + 2E_1 g(\theta_1, T)]}{[1 - f(\theta_1, T) + 1 - f(\theta_2, T)]} - \xi \frac{[-h(\theta_1, T) + h(\theta_2, T)]}{[1 - h(\theta_1, T) + 1 - h(\theta_2, T)]} \tag{3.14}$$

In the above equation, the first term is the result of the difference between coincident event rates. This has a contribution due to misalignment and a contribution due to $E_1$. The second term arises from a difference between the singles event rates. Ignoring detector variations, this will be non-zero only due to misalignment. By subtracting this term from the coincident events ratio, the misalignment effect can be removed. The factor $\xi$ is necessary to account for the difference between the singles and coincident gamma-ray anisotropies. The

32

singles events partially arise from gamma-rays following electron capture decays to higher nuclear levels (see Figure 1.1). These higher levels have different angular momentum values that induce a change in the observed gamma-ray anisotropy so that $f(\theta, T) \neq h(\theta, T)$. The factor $\xi$ was measured in the previous experiment and found to be $1.2 \pm 0.2$ and $1.4 \pm 0.2$ for the 1238 and 847 keV gamma-rays, respectively.

To eliminate the remaining asymmetries due to detector variations in Equation 3.13, data was collected at various temperatures and analyzed with the expression

$$\Delta = \kappa(\theta, T)E_1 + C \qquad (3.15)$$

where $\kappa(\theta, T)$ is the sensitivity factor that depends upon finite solid angles, detector positioning and temperature. In the previous work, $\kappa \approx -0.045$ at a temperature of 7 mK. The constant $C$ is used to account for differences in detector efficiencies and solid angles. Since these factors are temperature independent, any temperature dependence of $\Delta$ in Equation 3.15 could be ascribed to $E_1$. In this manner, a result of $E_1 = -0.011 \pm 0.022$ was obtained[27].

This analysis approach has obvious limitations. First of all, to eliminate the effect of detector variations, it requires the warming of the source. Without a temperature change, no separation of $E_1$ from $C$ can be made in Equation 3.15. This significantly reduces the experimental sensitivity, since a large portion of data must be taken with little nuclear alignment. Furthermore, the use of the singles data to correct for angular misalignment is limited by the precision to which the correction factor $\xi$ is known. Ideally, a new design would not require the warming of the source and would not depend upon use of the singles anisotropy.

## 3.3 Apparatus

The dilution refrigerator used in this experiment was designed and constructed specifically for this work. Without the constraints of an existing refrigerator, important advances were made to meet the design criteria peculiar to this type of experiment. Significant steps were

taken in all three aspects outlined in the previous section: refrigeration, detector coverage and techniques for eliminating systematic errors.

### 3.3.1 Refrigeration

To provide stable mK temperatures, an Oxford 400 $^3$He-$^4$He dilution refrigerator was used. Non-standard customizations of the Oxford 400 heat shields and vacuum can were performed by Oxford. There are three separate cooling stages in the refrigerator. The first stage is simply a bath of liquid $^4$He that surrounds the refrigerator vacuum can. This maintains the entire external surface at 4.2 K. The second stage consists of a small reservoir of liquid $^4$He that is pumped on to reduce the temperature of incoming circulation it surrounds to 1.2 K. Between this $^4$He pot and the dilution stage there are various intricate heat exchangers that cool the incoming circulation with the returning $^3$He gas. At the dilution stage there is a two phase mixture of $^3$He and $^4$He. One phase is a dilute mixture of $^3$He in $^4$He while the other is pure $^3$He. The less dense, pure $^3$He floats on top of the dilute $^3$He phase. Cooling occurs when $^3$He atoms move from the dilute phase into the pure $^3$He phase and are pumped away. The $^3$He gas is re-circulated and returned via the condenser line in a closed loop. Modern dilution refrigerators are capable of reaching base temperatures below 10 mK without demagnetization techniques. Temperatures below 50 $\mu$K are now accessible by first pre-cooling with a dilution refrigerator and then performing nuclear demagnetization on copper.

The design of the pumping system is standard with the exception of the $^3$He-$^4$He circulation pump. Rather than a mechanical scroll pump, a Varian MacroTorr turbo-molecular with V700HT controller was used. A turbo-molecular pump was chosen to minimize the amount of mechanical vibration transmitted along the pumping lines. Although this experiment is not sensitive to such vibrations, the dilution refrigerator is ultimately intended for vibration sensitive applications.

Typical operating parameters for the refrigerator are listed in Table 3.1. At these settings, the base temperature at the mixing chamber is routinely below 6.5 mK. This temperature has been maintained for periods as long as 2 months and measured with both

| | | |
|---|---|---|
| Pressures | Still | 20 mT |
| | Pot | 5.6 mm |
| | Condenser | 31 mm |
| Temperatures | Pot | 3.2 kΩ |
| | Still | 10.4 kΩ |
| | Cold Plate | 21.8 kΩ |
| | Mixing Chamber | 55 kΩ |

Table 3.1: Operating parameters for dilution refrigerator. Temperatures are listed as resistances measured with $RhO_2$ thermometry.

$^{60}$Co nuclear orientation as well as $RhO_2$ and Ge resistance thermometry.

### 3.3.2 Detectors

For gamma-ray detection, $5 \times 6$ inch NaI($Tl$) detectors are used. There are eight total detectors, arrayed in a plane as shown in Figure 3.6. Four of the detectors are packed close to the source and are positioned at $\pm 45°$ to the c-axis as shown. These detectors are sensitive to the $T$ violating correlation. The remaining four detectors are position at 0 and 90 degrees to the c-axis. These detectors are insensitive to $E_1$ and are used for cancellation of some systematic effects. The detector centers and the source crystal all lie in the same plane.

The four $E_1$ sensitive detectors are positioned just 6.7 cm from the source. This close packing of the detectors was achieved with a specially designed tail set for the dilution refrigerator and a complimentary helium dewar. To bring the gamma-ray detectors close to the source, the lower portion of the vacuum can and heat shields are tapered from an outer radius of 23 cm to 6 cm as shown in Figure 3.7. This reduces the size of the mK volume (from a standard cylindrical radius of 4 cm to 1.7 cm). The bottom of the surrounding helium dewar consists of an inner G-10 tail, an aluminum liquid nitrogen cooled shield, and then an outer G-10 tail. Aluminized mylar surrounds the outside of the inner tail for additional insulation. With this design, the distance between the central mK environment and room
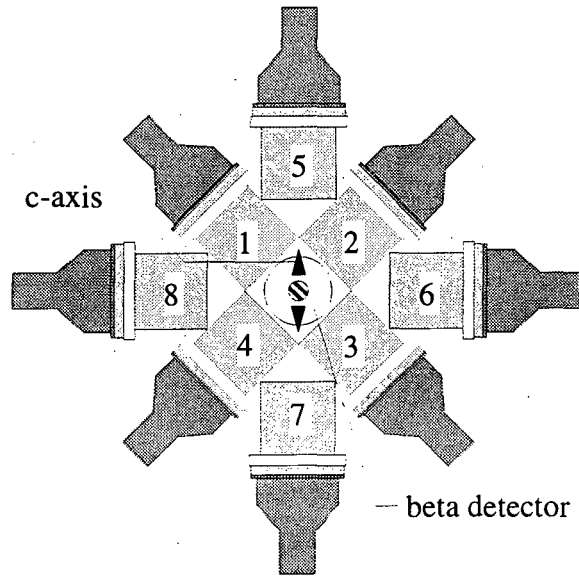
Figure 3.6: Top view of NaI($Tl$) detector arrangement. Detectors 1-4 are sensitive to $E_1$ and detectors 5-8 are used to eliminate other systematic uncertainties.

temperature was reduced to approximately 6 cm. This was achieved while maintaining very modest liquid helium consumption. While running, the liquid helium consumption was typically less than 4 liters/day. This allows for continuous running of 4-5 days without refilling liquid helium.

The beta-detector consists of a piece of high purity Si of 2 mm thickness with an active detection area of approximately 0.5 cm$^2$. As seen in Figure 3.7, this detector is located directly below the source and attached to the inner heat shield. This shield is thermally linked to the cold plate and operates at temperatures between 70-100 mK. This low temperature beta-detector was developed so that the source-detector distance could be minimized without raising the base temperature of the crystal. With this design, it was possible to bring the detector within 0.5 cm of the source with no apparent effect on the its temperature. The details of this detector are discussed in the next section.

The detector arrangement is similar to the previous geometry, but there are more detectors and they are situated closer to the source. Based simply on the improved detector coverage, this experiment enjoys a coincident count rate that is 60 times higher than the
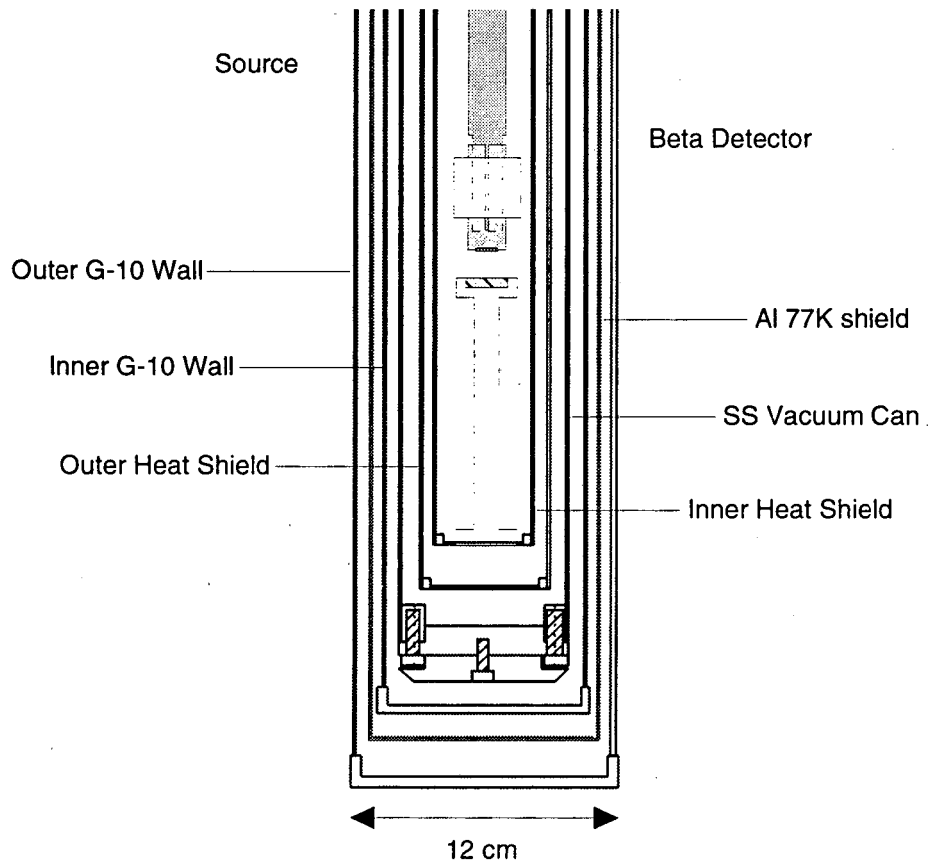
36

Figure 3.7: Cross-section of lower section of refrigerator and dewar.

previous experiment for the same intensity source. This comparison does not include consideration of temperature or solid angle correction factors, which are discussed in the analysis section.

### 3.3.3 Systematic Uncertainties

With the four $E_1$ sensitive detectors, the following ratio can be considered

$$R_\beta \equiv \frac{N_\beta^1 N_\beta^3}{N_\beta^2 N_\beta^4} \tag{3.16}$$

Where $N_\beta^i$ represents coincidences between the beta-detector and the $i$th gamma-ray detector. Substituting in the various efficiencies and angular terms using Equation 2.28, this becomes

$$R_\beta = \frac{(\epsilon_\beta \Omega_\beta)^2 \epsilon_1 \Omega_1 \epsilon_3 \Omega_3}{(\epsilon_\beta \Omega_\beta)^2 \epsilon_2 \Omega_3 \epsilon_4 \Omega_4} \frac{[1 - f(\theta_1, T) + E_1 g(\theta_1, T)][1 - f(\theta_3, T) + E_1 g(\theta_3, T)]}{[1 - f(\theta_2, T) + E_1 g(\theta_2, T)][1 - f(\theta_4, T) + E_1 g(\theta_4, T)]} \tag{3.17}$$

Assuming that the detectors are properly aligned and that the different efficiencies and solid angles are equal, Equation 3.16 is simply related to $E_1$.

$$E_1 \frac{g(\theta, T)}{1 - f(\theta, T)} = \frac{(1 - \sqrt{R_\beta})}{(1 + \sqrt{R_\beta})} \tag{3.18}$$

Of course, moving from Equation 3.17 to 3.18 requires unrealistic assumptions. Clearly, $R_\beta$ will deviate from unity for many reasons, including a non-zero $E_1$. As in the previous experiment[27], it is necessary to cancel out effects due to detector efficiencies and solid angles as well as misalignment.

To eliminate these effects, a "null" ratio, similar to that of Equation 3.17, but without any sensitivity to $E_1$ is measured. To construct such a ratio, one must measure the same gamma-ray anisotropy that follows the beta-decay, but without any sensitivity to the positron momentum. Integrated over all possible positron momenta, the $T$ violating correlation, $E_1(\hat{J} \cdot \hat{k})(\hat{J} \cdot \hat{p} \times \hat{k})$ vanishes. Hence, gamma-rays that are detected following the beta-decay, independent of the positron direction, are insensitive to $E_1$. Gamma-ray singles

events are likewise insensitive to $E_1$, but these events have a different anisotropy arising from electron capture events to higher nuclear levels.

To record such events, the additional four NaI($Tl$) detectors (labeled 5-8 in Figure 3.6) are used to detect the 0.511 MeV radiation that follows the positron annihilation. Since the positron will annihilate independent of the direction of its momentum, the annihilation radiation is ideal for a momentum insensitive beta trigger. By recording coincidences between the annihilation detectors and the $E_1$ sensitive detectors, the following ratio is constructed

$$R_a \equiv \frac{N_a^2 N_a^4}{N_a^1 N_a^3} \tag{3.19}$$

where the subscript $a$ is used to denote coincidences between the $i$th detector and the annihilation detectors. For simplicity, the annihilation detectors are treated as a single detector (this is trivially extended to all four annihilation detectors) and Equation 3.19 can be expressed as

$$R_a = \frac{(\epsilon_a \Omega_a)^2 \epsilon_2 \Omega_3 \epsilon_4 \Omega_4}{(\epsilon_a \Omega_a)^2 \epsilon_1 \Omega_1 \epsilon_3 \Omega_3} \frac{[1 - f(\theta_2, T)][1 - f(\theta_4, T)]}{[1 - f(\theta_1, T)][1 - f(\theta_3, T)]} \tag{3.20}$$

Taking the product of, $R_\beta$ and $R_a$, all of the efficiencies cancel to yield

$$
\begin{aligned}
R &\equiv R_\beta \times R_a \\
&= \frac{[1 - f(\theta_1, T) + E_1 g(\theta_1, T)][1 - f(\theta_3, T) + E_1 g(\theta_3, T)]}{[1 - f(\theta_2, T) + E_1 g(\theta_2, T)][1 - f(\theta_4, T) + E_1 g(\theta_4, T)]} \\
&\quad \times \frac{[1 - f(\theta_2, T)][1 - f(\theta_4, T)]}{[1 - f(\theta_1, T)][1 - f(\theta_3, T)]}
\end{aligned} \tag{3.21}
$$

Factoring out the $(1 - f(\theta_i, T))$, this reduces to

$$R = \frac{[1 + E_1 g(\theta_1, T)/(1 - f(\theta_1))][1 + E_1 g(\theta_3, T)/(1 - f(\theta_3))]}{[1 + E_1 g(\theta_2, T)/(1 - f(\theta_2))][1 + E_1 g(\theta_4, T)/(1 - f(\theta_4))]} \tag{3.22}$$

and since $g(\theta_i, T) = -g(-\theta_i, T)$, we can make the following approximation.

$$\frac{g(\theta_1, T)}{1 - f(\theta_1)} \approx \frac{g(\theta_3, T)}{1 - f(\theta_3)} \approx \frac{-g(\theta_2, T)}{1 - f(\theta_2)} \approx \frac{-g(\theta_4, T)}{1 - f(\theta_4)} \tag{3.23}$$

Equation 3.23 is only approximate in as much the detectors are not aligned to the crystal

axis. Combining these last two equations, $E_1$ is given by

$$E_1 = \frac{1 - f(\theta, T)}{g(\theta, T)} \times \frac{(1 - \sqrt{R})}{(1 + \sqrt{R})} \equiv \frac{1}{\kappa(\theta, T)} \times \frac{(1 - \sqrt{R})}{(1 + \sqrt{R})} \tag{3.24}$$

The factor $\kappa(\theta, T)$ is the sensitivity factor. Up to this point, the detectors have been treated as point objects. For the actual analysis, the factor $\kappa(\theta, T)$ is integrated over the finite NaI(*Tl*) and beta detector solid angles. This and other necessary corrections to $\kappa$ are discussed in Section 4.4.

If $E_1$ is identically zero, Equation 3.22 reduces simply to $R = 1$. This is independent of any assumptions about detector alignment or efficiencies. Further, this result is obtained without warming the source or using the singles anisotropy. The "null" ratio provided by the annihilation trigger provides a robust means to cancel out the most significant sources of a false $E_1$.

## 3.4    A mK Beta Detector

In the search for heavy dark matter, semiconductor detectors capable of simultaneously detecting both ionization and phonon pulses have been developed. This dual detection approach is used to distinguish the massive dark matter candidates from the less massive background events[47]. Since massive particles tend to deposit more energy in the form of phonons, a measurement of both charge and phonon signals is a means to discriminate heavy dark matter candidates from the less massive background events arising from gamma-rays, electrons or muons interacting in the detector. In order to measure the phonon pulses, it is necessary to cool the semiconductor materials to mK temperatures and hence dilution refrigerators are routinely used.

For this work, such a low temperature detector could solve many challenges. Since it can operate at mK temperatures, no heating of the detector would be required for operation in the dilution refrigerator. Furthermore, since the detector does not require heating, it can be placed in close proximity to the source to maximize solid angle. However, it was determined that the phonon output signal from these detectors could not be used. Most of

the detector designs yielded pulses with risetimes of several milliseconds[48]. For the low rate dark matter experiments, these risetimes were acceptable, but for the higher counting rates expected in this experiment, pulse risetimes at least 1000 times faster than the typical bolometers are required.

Fortunately, the ionization pulse from these devices is much like that from a standard liquid nitrogen or room temperature semiconductor detector. Since in this experiment it is not necessary to record both the thermal and ionization signals, the thermal signal can be discarded in favor of the faster charge signal. In this simplified form, these devices offer a logical replacement for the Si(Li) detector technology used in the previous experiment[49]. The detector can be kept at mK temperatures, near the source crystal, without any heating or significant obstructions between them.

For an ionization detector, we chose to·work with silicon. Although significant work has also been done with germanium[48], silicon was chosen because of its lower atomic number $Z$. The lower $Z$ of silicon reduces the probability that a positron will backscatter out of the detector[50] and cause some distortion in the beta-decay spectrum. Although this experiment is not concerned with a precise measurement of the beta-decay spectrum, the backscattered events are still undesirable since the positron only deposits a fraction of its incident energy in the detector. If this fraction is below the detector noise threshold, the resulting pulse cannot be well discriminated from noise and the event is lost.

A high-purity silicon sample was obtained from the Low Temperature Physics Laboratory at Stanford University[51]. The room temperature resistivity of the sample is 40 k$\Omega$-cm. It measures $10 \times 10 \times 2$ mm thick and has a thin layer of titanium ($\approx 40$ nm thick) evaporated onto both square faces to act as electrodes. The 2 mm thick sample is just thick enough to fully stop the highest energy positrons from $^{56}$Co ($E \approx 1.46$ MeV) so that the total energy of the incident particles is measured[52]. The incident positrons interact in the silicon volume, creating electron-hole pairs. For silicon, the energy necessary to create an electron-hole pair is 3.7 eV[49]. A voltage is applied across the silicon to generate an electric field that sweeps the electrons and holes to the negative and positive contacts respectively. The total charge collected at the contacts is a direct measurement of the energy of the

detected particle.

Using an internal conversion electron source, $^{207}$Bi, we performed various studies of the beta detector at different temperatures and different applied voltages. The mono-energetic electrons from $^{207}$Bi were useful for studying the detector performance at energies comparable to those of $^{56}$Co (Q = 1.46 MeV). The electronics used for these measurements were conventional. An Ortec 142B pre-amplifier was mounted at room temperature on top of the cryostat. The detector was wired with stainless steel coaxial wire with a total length of 2 meters and capacitance of 260 pF. A Tennelec 222 fast/slow amplifier shaped the output from the pre-amplifier. The resulting unipolar pulse was digitized with a peak sensing ADC (Ortec model AD811).

Most of our experiences with the silicon sample match the observations of the Stanford group[53]. In particular, when first cooled, the sample exhibits "Mode I" followed by long term, stable "Mode II" behavior. In Mode I, the charge collection at a fixed voltage was poor. Over time, at the same applied voltage, the charge collection improved and would stabilize in a matter of hours after the initial mK cooling. In Mode I some of the charge liberated by the incident radiation is trapped at acceptor and donor impurities before it is collected. As the detector continues to be irradiated (or, in the case of some groups, an LED is turned on) these trap sites are filled. As the traps are filled, the charge collection efficiency increases and the detector enters Mode II.

A typical spectrum obtained with the $^{207}$Bi source is shown in Figure 3.8. This spectrum is obtained at a temperature of 100 mK after the detector had entered Mode II behavior. The corresponding energy calibration, using the four electron peaks, is shown in Figure 3.9. The energy calibration is found to be linear. The noise threshold is at about 175 keV. At 1 MeV, the resolution of the detector (FWHM) and electronics is 50 keV.

The effect of applied voltage on pulse height is shown in Figure 3.10. The pure Si sample operates at much lower voltages than typically used in commercial Si diode devices. Above bias voltages of 10 volts there is little change in the charge collection and resulting pulse height. While running, the bias voltage is maintained at 15 volts, corresponding to 75 volt/cm in Figure 3.10.
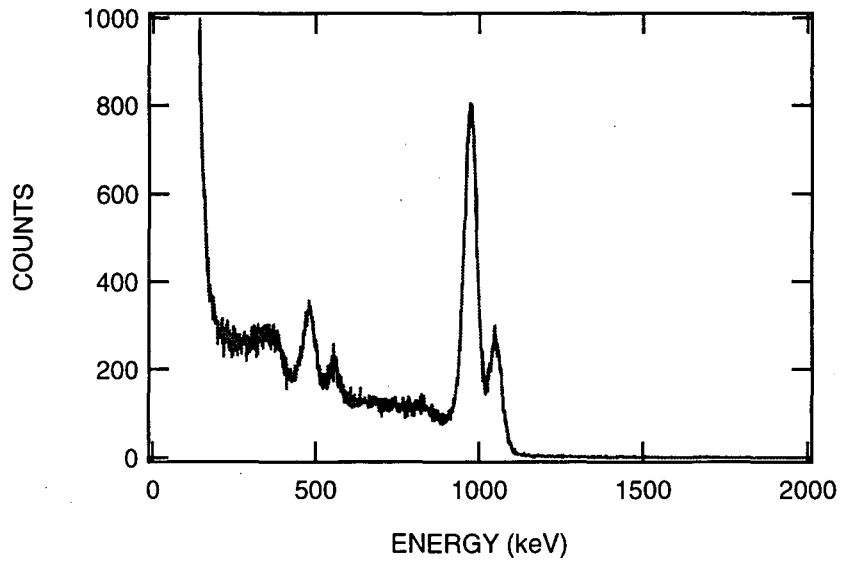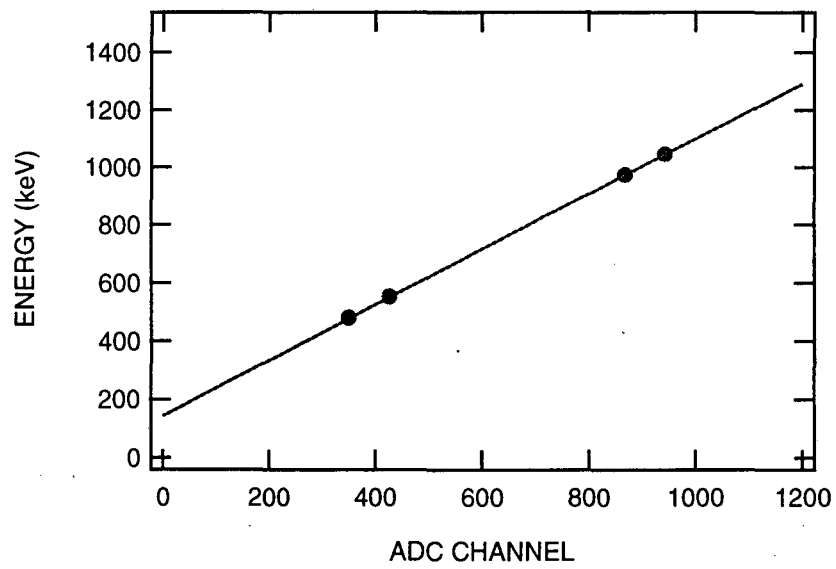
Figure 3.8: $^{207}$Bi pulse height spectrum at 100 mK.



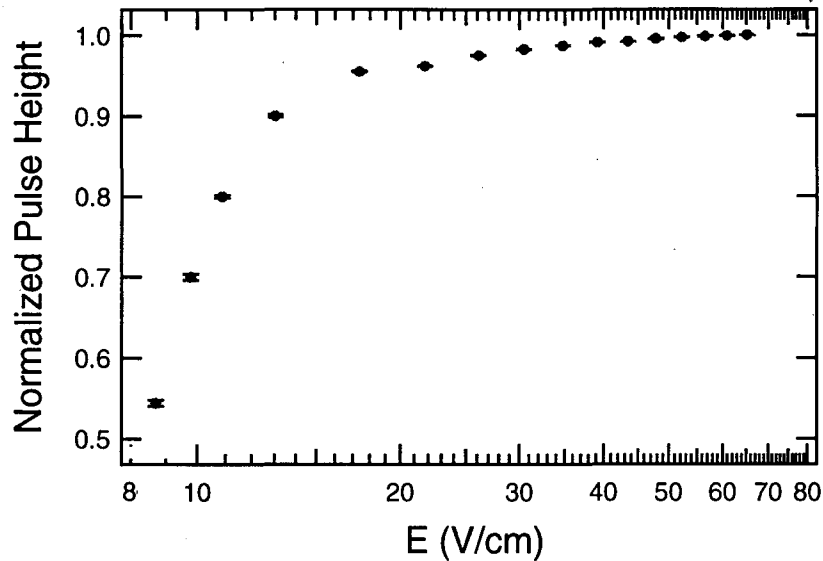Figure 3.9: Energy calibration using $^{207}$Bi.

Figure 3.10: Pulse height dependence on applied electric field.

## 3.5 Source Preparation

### 3.5.1 Crystal Preparation

Cobalt single crystals[54] were cut to nominal dimensions of $5 \times 5 \times 1$ mm. The c-axis was oriented parallel to the square plane and along one of the 5mm edges to within a 0.5 degree precision. The choice of crystal shape was determined by three criteria: (1) a desire for symmetry about the c-axis, (2) maximum surface area for implantation and (3) a simple means to make robust thermal contact. Although closure domains, which have a magnetization perpendicular to the c-axis, are minimized with a parallelepiped shaped crystal (with the c-axis parallel to the long dimension)[44], such a geometry is not optimal for any of the aforementioned criteria. The square geometry chosen provides greater symmetry and a larger surface area for implantation and thermal contact. To minimize the effect of closure domains, which occur at crystal edges, the implantation of the $^{56}$Co was performed within the central 4 mm of the 5 mm square.

Prior to implanting the $^{56}$Co into the single crystal cobalt, the crystal surface must be treated by mechanical and chemical polishing. These treatments are necessary to remove the deformation layers created when the crystal was cut. These deformation layers are not

single crystal cobalt and therefore do not provide the necessary hyperfine field for nuclear alignment. Although the deformation layer does not extend more than 50-100 $\mu$m into the bulk, the implantation will deposit [56]Co at a mean depth of only 500 angstroms into the crystal. The surface treatments used in this work are identical to those reported in reference [55], where [186]Hg was implanted into single crystal hcp Co. The implantation voltage in that work was 60 keV and was performed at the on-line mass separator ISOLDE-3 at CERN. Despite this low implantation voltage, the surface preparation proved adequate to ensure placement of the [186]Hg into substitutional sites of single crystal Co. For this work, the available implantation voltage was 180 keV (described in Section 3.5.2) and the implanted nucleus is approximately 3 times less massive.

Of the two crystal faces, only the implantation side requires the elaborate surface treatments. However, a coarse mechanical polish was also given to the backside of the crystal. This was done to remove the oxide layers that had formed over time. It is possible that such a cobalt-oxide layer would present significant thermal resistance at mK temperatures.

For the implantation surface polishing, each cobalt crystal is first mounted into an cylindrical epoxy form. The crystal is held against plate glass while epoxy is poured into a cylindrical mold over and around the sample. The crystal face is level with the flat epoxy face formed by contact with the plate glass. This form holds the sample during the polishing procedure and helps to reduce excessive polishing of the crystal edges. Attempts to polish test pieces without the epoxy form led to severely rounded edges that significantly reduced the flat surface area of the crystal.

The mechanical polishing is performed with diamond paste of decreasing size. Initial polishing is performed with 45 $\mu$m surface followed by 30, 15, 10, 6, 3, 1 and 0.25 $\mu$m diamond paste. The surface is polished using a Buehler Minimet polisher. This device automatically moves the epoxy mold in a figure-8 motion over the diamond paste at adjustable speeds and applied pressures. For each paste, the sample is polished for 5 minutes at constant pressure and then for an additional 5 minutes with the pressure slowly decreasing to zero. After each polishing step, the sample is cleaned in an ultrasonic bath of distilled water mixed with a solvent designed to help remove the diamond particles from the surface[56]. Special

care is necessary to avoid contamination of the finer polishing steps with the paste from the previous treatments. Contamination causes deep scratches to be made in an otherwise optically smooth surface.

After the final mechanical polishing step, the crystals are removed from the epoxy forms by placing them in an ultrasonic bath of acetone for a few hours. Following the mechanical polishing steps, the cobalt surface is optically smooth and scratches are not visible to the naked eye. However, even after the 0.25 $\mu$m polish, a deformation layer of 0.25 microns exists below the surface. The average implantation depth is approximately five times less than this and therefore a chemical polishing step is required.

Unlike mechanical polishing, electropolishing does not involve the destructive grinding of one material into another. By applying a potential difference between anode and cathode in the presence of a polishing solution, a reaction occurs which is similar to plating, but reversed. Layers of the sample are removed by chemical reactions and the amount of material removed can be monitored with an ampmeter. The principles of electropolishing are simple, but successful execution requires knowledge of recipes that are peculiar to the sample to be polished. In particular, one must know what solution and applied voltage/current should be used. Also, some recipes recommend particular cathode materials other than that of the sample.

For the electropolishing of cobalt, a solution of ortho-phosphoric acid (85%) was used. The cathode and all wires in the solution were made of cobalt. A constant voltage of 1.4 V was applied prior to introducing the cathode and anode into the ortho-phosphoric acid. This is absolutely essential to achieve a successful polish. Without the applied voltage, the reverse reaction occurs and this causes small hydrogen bubbles to form on the sample surface where plating, not electropolishing, is occurring. During the polishing process, a red film forms on the sample and the cathode collects small gas bubbles. A current of 13 mA is observed for 6 minutes. Given the geometry of the electropolish apparatus, this corresponds to the removal of $\approx 3\mu$m of surface material from the Co crystal. After polishing, the assembly is removed from the acid with the voltage on. The voltage is turned off and the sample is immediately flushed with distilled water. The crystal is then transferred to an ultrasonic

46

bath of distilled water to remove any remaining acid from the surface.

## 3.5.2 Implantation

The implantation was performed at the ATLAS accelerator in the Physics Division at Argonne National Laboratory (ANL)[57]. The ion source and platform at ATLAS produce singly charged beams of energies up to 200 keV. A mass analyzing magnet is followed by a magnetic quadrupole for beam focusing. The ion source is normally used at ATLAS to inject various beams into a tandem. For the implantation, our crystal targets were placed in the beamline after the quadrupole element and before the tandem.

The source material inserted into the ion source is referred to as a cone. The cones used in this work were created by $^{58}Ni(p, 2n)^{56}Ni$ with 40 MeV protons from the IPNS at ANL. These cones were produced in an unrelated effort to produce a radioactive beam of $^{56}Ni$. Fortunately, the $^{56}Ni$ decays with a half-life of 6.6 days to the desired $^{56}Co$. After several $^{56}Ni$ half-lives, when the activity is primarily $^{56}Co$, we were able to use the cones for our implantation.

The Co crystals were mounted on a 3 stage target ladder with circular collimators of 4 mm diameter. The first stage held only a collimator with no crystal target. This was used to tune the $^{58}Ni$ beam and periodically check on the source stability. After tuning to the mass-58 peak, the analyzing magnet was scanned to a calculated value for mass-56 and the target ladder was moved to one of the two other stages that held the crystal targets. The beam current at the mass-56 setting was not reliably measured and hence no additional adjustments to the beam optics were made after changing the analyzing magnet. Two implantations at 180 keV were successfully performed. The first implantation run lasted 4 days and produced a 10 nC source. The limiting factor in this first effort was the old radioactive cone that was produced a year before our implantation. A second implantation was performed over a period of 5 days with a fresh radioactive cone (less than 1 month old). This effort yielded a source activity of 800 nC. No annealing of the cobalt crystals is performed following the implantations. It has been demonstrated[58] that additional annealing, beyond that which naturally occurs at room temperature during implantation,

does not produce significantly better substitution of the implanted nuclei in the Co host lattice.

### 3.5.3 Thermal Contact

Since the degree of nuclear alignment depends strongly on the crystal temperature, it was essential to provide good thermal contact between the source and mixing chamber. The source is located approximately 50 cm from the mixing chamber so that it is situated in the tail section of the surrounding dewar. Several different designs to couple the source and mixing chamber were investigated. Initial designs proved inadequate and resulted in temperature gradients approaching 5-10 mK between the mixing chamber and crystal.

The final design, which yielded a temperature gradient less than 0.75 mK, consists of three different thermal joints. The first joint couples a long section of gold plated oxygen-free high conductivity (OFHC) copper (source rod) directly to the mixing chamber. This single piece is bolted to the mixing chamber with 10 M6 brass screws. Since the brass screws will undergo greater thermal contraction than the copper source rod, additional clamping pressure is provided during the cooling process.

The second joint connects the source rod and the source holder. The source holder is another piece of gold-plated OFHC copper that slip fits over the end of the source rod. The two pieces are held together with a nylon ring that slips over the source holder. The nylon ring is sized so that at room temperature it just barely slides over the assembly. Again, the concept of differential thermal contraction is used to provide a strong clamping effect. The nylon will undergo greater thermal contraction than the copper during the cooling process. During assembly, it was necessary to heat the copper and nylon slightly above room temperature to initially install the pieces. This guaranteed firm clamping even at room temperature.

The final joint is between the cobalt crystal and the source holder. Woods metal, a low temperature solder, is used to mount the crystal on the source holder. The choice of solder can be critical. Some solders are superconducting at mK temperatures and as such they become very poor thermal conductors. This is true of more common solders such as indium

48

and lead. These superconductors cannot be used unless the solder will be in the presence of a sufficiently strong magnetic field to quench the superconductivity. In addition, care must be taken so that the Co crystal is never heated above 390°C. At this temperature, hcp Co undergoes an irreversible phase change to bcc and its useful domain properties are lost.

## 3.6 Data Collection

Data were collected using a VAX 3100 running the CHAOS data acquisition system[59]. The CHAOS system recorded event mode data from a CAMAC crate to disk. CHAOS uses a single, master trigger to enable the read-out of the CAMAC system.

Data were recorded to disk in event mode and each run lasts 8-12 hours. A total of 12, 16 bit parameters are read out for each event. Both the beta and gamma signals are amplified with fast/slow spectroscopy amplifiers. The fast signal output is a tail pulse useful for discrimination and timing purposes. The slow output is a 3 $\mu$s shaped pulse that is used for energy measurements. The shaped pulses from all 8 NaI($Tl$) detectors and the beta detector are digitized with two Ortec AD811 peak sensing analog to digital converters. To measure background due to accidental coincidences, a LeCroy 2251 time to digital converter is used for both the beta-gamma and annihilation-gamma coincidences. Finally, a LeCroy 2241 event register is used to record which detectors initiated the trigger.

Either a beta or an annihilation trigger satisfies the hardware trigger. The beta trigger requires a coincidence between any of the $E_1$ NaI($Tl$) detectors (labeled 1-4 in Figure 3.6)and the beta detector. The annihilation trigger is satisfied by a coincidence between any of the $E_1$ NaI($Tl$) detectors and a pair of the annihilation detectors (labeled 5-8 in Figure 3.6). A less strict annihilation trigger, requiring only a single annihilation detector to be in coincidence with one of the $E_1$ detectors, was also considered. This scheme proved to be too sensitive to events where a single gamma-ray entered an $E_1$ detector and then scattered into an adjacent annihilation detector. This caused the acquisition system to trigger at an unacceptably high rate (approaching 6 kHz with the stronger source). Hardware thresholds for the $E_1$ NaI($Tl$) detectors are set just below the 0.511 MeV annihilation peak. The other NaI($Tl$) detectors and the beta detector have thresholds set just above the electronic noise

level.

The refrigerator temperature is monitored using both the $RuO_2$ resistance thermometer and the $^{56}Co$ nuclear orientation signal. Helium transfers are required once every 4-5 days and the liquid nitrogen shield is filled every 2-3 days. The refrigerator cold traps are cleaned at least once a month. During these operations, the data acquisition system is temporarily halted.

# Chapter 4

# Results

Data were collected with two different intensity sources. Initially, a 10 nC source was used to verify the crystal preparation and implantation procedures, as well as to develop the data acquisition trigger. With this initial source, the nuclear orientation signal indicated a temperature of 6.5 mK. This was consistent with the mixing chamber temperature measured via resistance thermometry. It was therefore concluded that the crystal surface preparation was adequate and that the implanted $^{56}Co$ was situated in substitutional and not interstitial sites in the host crystal. Data was collected with this weak source for one month to verify long-term stability of the refrigeration and data acquisition system. Following this run, an 800 nC source was produced using identical preparation methods. The data from this source is discussed in the following sections.

The first part of this chapter describes the alignment of the NaI($Tl$) array relative to the nuclear orientation axis. As discussed in Section 3.3.3, small angular misalignments which might lead to a false $E_1$ are cancelled by the annihilation-gamma coincidence ratio. However, one of the remaining systematic uncertainties depends on this misalignment angle at a higher order. In order to provide an accurate estimate of this effect, attention is given to measuring the misalignment angle accurately. An explanation of the energy calibrations and temperature determination is then given. This is followed by a description of the event selection criteria for the beta-gamma and annihilation-gamma coincidences which enter into the ratio $R$. The experimental sensitivity factor $\kappa$, which relates $R$ to $E_1$, is then discussed.

Finally, the value of $E_1$ and the remaining systematic uncertainties in this measurement are discussed.

## 4.1 Array Alignment

The NaI($Tl$) array was adjusted so that the detector plane was parallel with the crystal surface and the source was vertically centered on the detector faces. The initial angular alignment of the array to the cobalt crystal edge was only approximate. Since the crystal edge may not be parallel with the crystal axis, it is not sufficient to simply align the array along an edge of the crystal. Rather, it is better to use the gamma-ray anisotropy itself, which depends entirely on the crystal axis, to provide a measure of the array alignment.

In general, the gamma-ray anisotropy from aligned nuclei will have the form

$$W(\theta) \propto 1 - \alpha_2 P_2(cos\theta) - \alpha_4 P_4(cos\theta) \tag{4.1}$$

where $P_2$ and $P_4$ are Legendre polynomials. This expression ignores higher order even multipoles assumed to give a negligible contribution. The coefficients, $\alpha_2$ and $\alpha_4$, depend upon temperature, the particular nuclear level decay sequence and finite detector solid angles. In the approximation that the angular misalignment of all the detectors can be characterized by a single angle, Equation 4.1 can be generalized to

$$W(\theta) \propto 1 - \alpha_2 P_2(\cos(\theta + \delta)) - \alpha_4 P_4(\cos(\theta + \delta)) \tag{4.2}$$

where $\delta$ is the angle used to describe the misalignment of the detector array. By measuring this distribution at several angles, it is possible to determine $\delta$.

To measure this angular distribution, the NaI($Tl$) detectors 1-4 shown in Figure 3.6 are retracted to the same radial position as detectors 5-8 so that a regular octagonal array is formed. The eight detectors are set at $45 \pm 0.1°$ relative to each other and are equidistant from the source. This angular precision is based upon the tolerances of the array support structure and not on the detectors themselves. In this configuration, data were collected
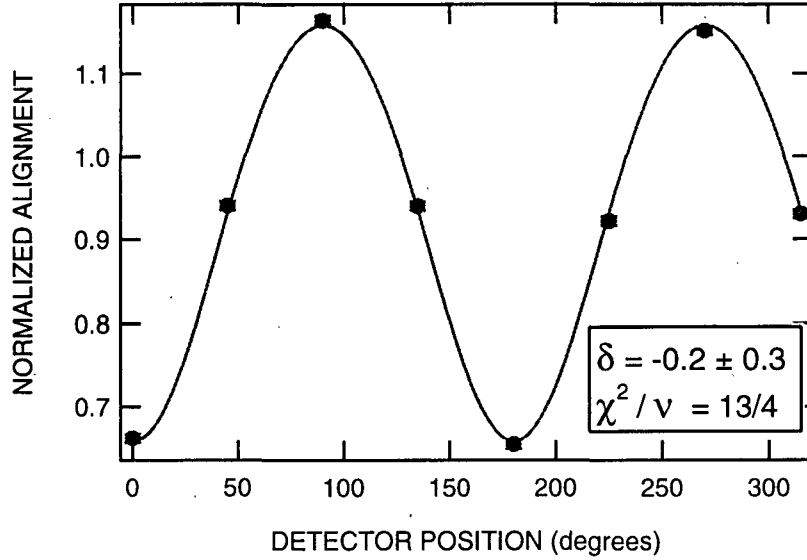
52

Figure 4.1: Nuclear orientation angular distribution.

with a simple trigger that simply collected singles events from all of the NaI($Tl$) detectors. A window was placed around the 1238 keV peak for each detector and the event rate within each window was recorded with the refrigerator operating near its base temperature. To cancel effects due to detector efficiencies, these rates were normalized by the corresponding rates measured at temperatures above 100 mK where the gamma-ray emission is isotropic [ and $\alpha_2 \approx \alpha_4 \approx 0$.

The anisotropy data before adjusting the array was measured and a fit to Equation 4.2 indicated that $\delta = 4.2 \pm 0.3°$. Based on this measurement, the array was rotated, and the subsequent distribution was recorded. This angular distribution and the corresponding fit is shown in Figure 4.1. The fitting procedure yields $\delta = -0.2 \pm 0.3°$. The quality of fit according to the chi-square estimator ($\chi_\nu^2 = 3.25$) is poor. The probability of exceeding the observed chi-square is less than one percent. This poor quality of fit was also observed in the data prior to adjusting the array ($\chi_\nu^2 = 3.5$). The high values of chi-square reflect the limitations of the underlying model being used. In reality, each detector is slightly misaligned by some amount, and the assumption of a single misalignment angle is not strictly valid. Moreover, the error in $\delta$ returned by the fitting algorithm is not an accurate indication of the true variance. Although any misalignment of the array cancels to first
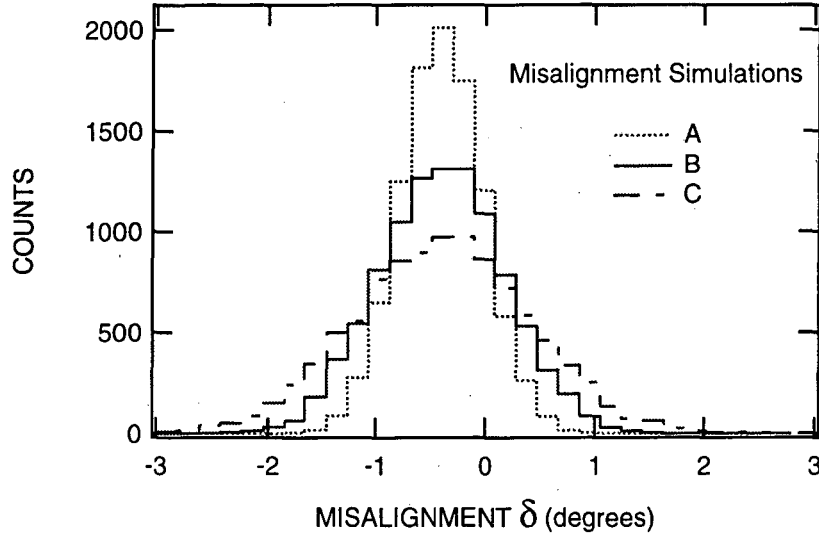
53

Figure 4.2: Simulations of angular misalignment determination. The three different histograms correspond to three different models of individual detector variations.

order in the ratio $R$, $\delta$ is used to estimate higher order systematic effects and it is necessary to have an accurate measure of its error.

To estimate the realistic variance in $\delta$, a simulation was performed. The inputs to the simulation include $\alpha_2$, $\alpha_4$ and a total misalignment angle $\delta$. Randomized angular offsets generated from a gaussian distribution represent the individual detector misalignments. The statistical power of each simulation is the same as the experimental data. The simulated data sets are then fit to Equation 4.2 and the computed $\delta$ is histogrammed. The width of the resulting histogram is an indication of the error in $\delta$. In Figure 4.2, three different histograms, corresponding to three different variances for the randomized angular offsets, are shown. The one sigma variance of the randomized angular offsets is set at 0.5°, 1.0° and 1.5° for the simulations labeled A, B and C respectively. These angular offsets correspond to maximum displacements of 4, 8 and 12 mm at the position of the detector faces. With the increase of the individual detector variations, the width of the histograms increases. This is expected, because as the individual detector misalignment increases, the model of Equation 4.2 becomes increasingly inaccurate. This results in a relatively flat profile in chi-square space, which in turn increases the variance on the returned parameter $\delta$. A summary of the simulations is shown in Table 4.1. As shown in the table, the variance

| Simulation | $\delta$ | $V_\theta$ | $\sigma_\delta$ |
|:---:|:---:|:---:|:---:|
| A | -0.4° | 0.5° | 0.4° |
| B | -0.4° | 1.0° | 0.6° |
| C | -0.4° | 1.5° | 0.8° |

Table 4.1: Results of alignment simulation. The $\delta$ and $V_\theta$ columns are the input values for the different simulations. Here $\sigma_\theta$ represents the one sigma variance of the random angular misalignment assigned to the individual detectors. The $\sigma_\delta$ column is the variance deduced from the simulation output in Figure 4.2.

in $\delta$ for simulations A, B, and C are 0.4, 0.6 and 0.8° respectively. Simulation C is probably too pessimistic since it allows for individual angular misalignments that correspond to displacements as large as 10 percent of the detector size. But, to maintain a conservative estimate of the error in $\delta$, the result of simulation B is used and the error in the measured value is taken to be

$$\delta = -0.2 \pm 0.6°. \tag{4.3}$$

This error is twice as large as the value returned from the fitting procedure. As discussed in Section 3.3.3, the primary effect of this angular misalignment is canceled by normalizing the beta-gamma coincidences with the annihilation-gamma coincidences. Only higher order effects that are sensitive to this error estimate are discussed in Section 4.5.

## 4.2 Energy Calibration and Temperature Determination

The singles gamma-ray spectrum from $^{56}$Co is shown in Figure 4.3. The three prominent gamma-ray peaks correspond to the 511 keV positron annihilation radiation, and the 847 and 1238 keV gamma-rays from the excited states of $^{56}$Fe. The additional peaks are from other excited states in $^{56}$Fe. These peaks are fit to gaussians and a polynomial background to determine the energy calibration. Over a wide energy range, it was found that the NaI($Tl$)
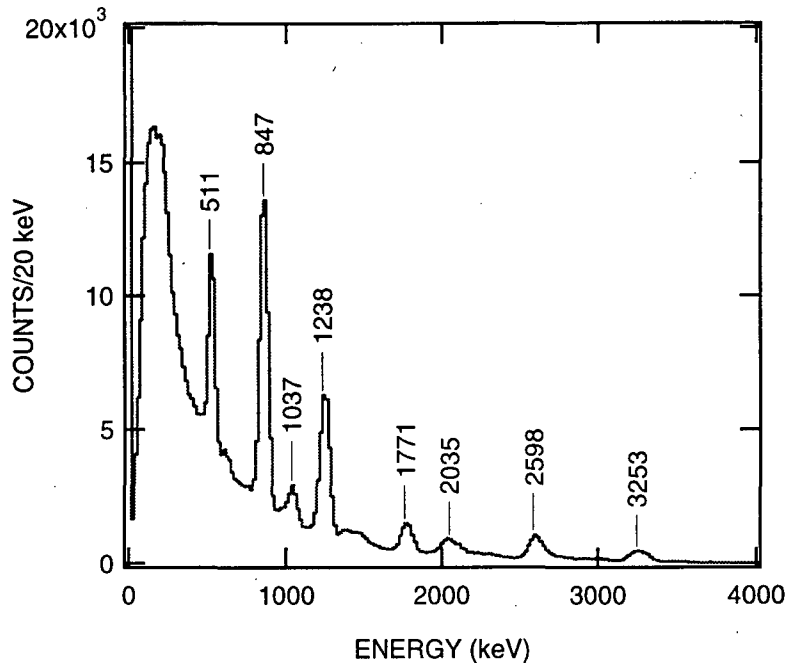
Figure 4.3: $^{56}$Co singles gamma-ray spectrum. The various gamma-rays shown in the level scheme of Figure 1.1 are labeled.

detectors required a small quadratic term in the energy calibration. This is probably due to the saturation of the photomultiplier at higher energies. A calibration is made for all of the NaI($Tl$) detectors for each run. This procedure accommodates small gain shifts, due primarily to room temperature fluctuations, that were observed over the course of the run. These gain shifts do not directly impact the measurement of $E_1$ since any shift that occurs in the beta-gamma coincidence channel will be canceled by the corresponding detector in the annihilation-gamma coincidence channel.

An energy calibration for the mK beta detector and the corresponding spectrum is shown in Figure 4.4. The discriminator threshold in the beta-spectrum corresponds to an energy of about 75 keV. The events recorded below 75 keV result from NaI($Tl$) singles events for which there were no beta event to read out. Above 200 keV, the spectrum exhibits some additional structures other than the continuous beta-decay spectrum. These additional features are due to Compton scattering of photons in the sensitive Si volume. Compton edges are visible for the 511, 847 and 1238 keV gamma-rays. By requiring gamma-ray energies in the NaI($Tl$) detectors that correspond to decays without positron emission,
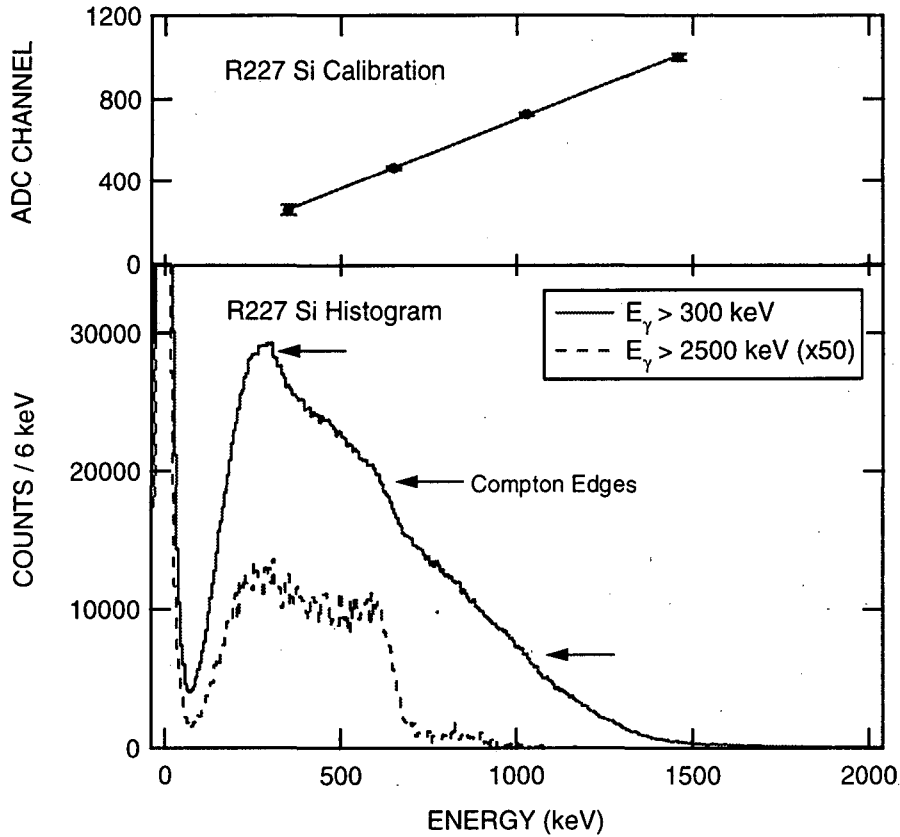
Figure 4.4: $^{56}$Co beta-decay spectrum measured with mK beta detector and corresponding energy calibration. Compton edges from the 511, 847 and 1238 keV gamma-rays are indicated by arrows in the spectrum. The solid line corresponds to events where the NaI($Tl$) detector recorded $E_\gamma > 300$ keV and the dashed line corresponds to events with $E_\gamma > 2500$ keV.

these Compton edges can be enhanced and used for energy calibration points.

In particular, as seen in the bottom of Figure 4.4, a requirement that a NaI($Tl$) detector records $E_\gamma > 2500$ keV yields an enhanced Compton spectrum for the 847 keV gamma-ray. Decays with $E_\gamma > 2500$ keV arise primarily from two gamma-ray cascades, shown in Figure 1.1, arising entirely from electron capture with no positron emission: 2598 → 847 and 3253 → 847 keV. The low energy Compton edge ($E \approx 350$ keV) corresponds to Compton scattering of 511 keV photons. Finally, the spectrum endpoint ($Q \approx 1.46$ MeV) provides another calibration point. The energy calibration is made for each run. The detector system is linear within the precision of the calibration method.

The nuclear orientation induced gamma-ray anisotropy is analyzed to determine the
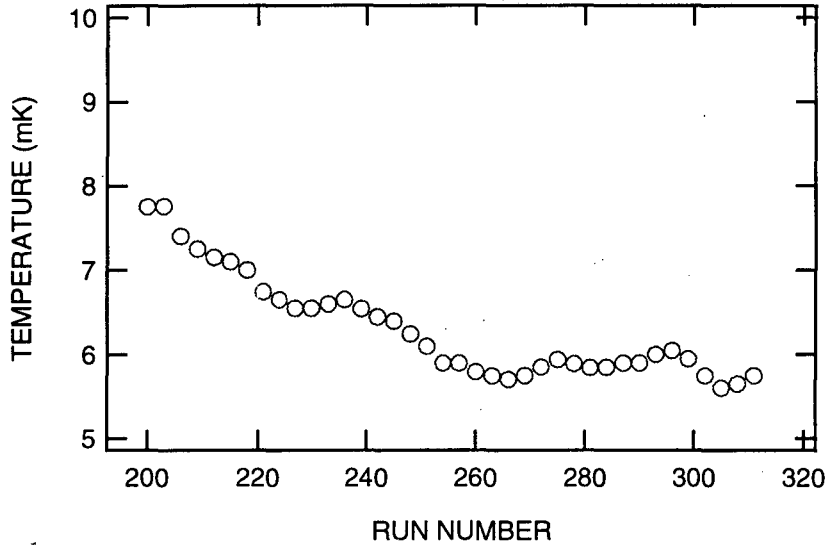
Figure 4.5: Source temperature deduced with nuclear orientation signal. Run length varies, but the time scale is approximately 1 day = 2 run numbers.

source temperature for each run. For this temperature determination, events are selected with beta energy above the Compton edge from the 847 keV gamma-ray ($E_\beta > 650$ keV). This requirement minimizes the sensitivity to the electron capture decays that have a different anisotropy signal. From these events, histograms of the gamma-ray energy in detectors 5 and 6 are formed. These detectors are located at 0° and 90° to the crystal axis where the anisotropy is at a minimum and maximum respectively. Events in a 150 keV energy interval centered on the 1238 keV peak are integrated for each detector and the ratio of $W(\theta = 90°)/W(\theta = 0°)$ is used to determine the source temperature. To eliminate variations due to detector efficiencies, these numbers are normalized by the relative efficiency determined at 100 mK where there is no anisotropy. This ratio is corrected for the finite detector solid angles and the temperature is determined assuming the known values of the nuclear moment($\mu = 3.851\mu_N$[39]) and hyperfine field ($B_{eff} = -22.7$ T[46]).

The temperature measured with the nuclear orientation signal exhibits a slow cooling process from 8 mK to slightly less than 6 mK over the first half of the experiment as seen in Figure 4.5. This cooling time constant ($\approx 3$ weeks) was longer than the trial experiment with the weaker activity source ($\approx 5$ days) and suggests that the thermal resistance between the source and mixing chamber was somewhat higher. Without heaters located in the

appropriate places, it was not possible to determine which thermal joint, was the source of increased resistance. The ultimate base temperature achieved was slightly lower ($\approx 0.5$ mK) than the trial experiment. This ultimate improvement is attributable to an optimization of the various operating pressures. In particular, the $^4$He pot pressure was reduced so that the returning circulation was cooler than the previous run.

## 4.3   Determination of $R$

Following the detector calibration and temperature determination, event selection is performed for the beta-gamma coincidences and the annihilation-gamma coincidences. From these coincidences, the ratio $R$ is constructed. Combined with the sensitivity factor $\kappa(\theta, T)$, $R$ determines $E_1$.

The beta-gamma coincidences recorded by the hardware trigger are subject to additional selection criteria. These criteria include: beta energy, gamma energy and coincidence timing. The beta energy is required to be $350 < E_\beta < 1850$ keV. The upper energy limit extends well beyond the beta spectrum endpoint ($Q \approx 1460$ keV) to include events where both a beta and a Compton scattered annihilation photon summed in the silicon detector. The lower energy threshold is chosen to reduce coincidences where only a gamma-ray triggered the beta detector. Requiring $E_\beta > 350$ keV eliminates a significant fraction of these Compton scattered gamma-rays, including all of those events arising from the 511 keV annihilation radiation. The remaining Compton scattered events effectively dilute the sensitivity to $E_1$. The size of this effect is discussed in Section 4.4. The NaI($Tl$) spectrum recorded in detector 1 after this energy cut is shown in Figure 4.6. Compared to the singles spectrum shown in Figure 4.3, there is an obvious enhancement of the 511 keV peak and a significant suppression of those gamma-ray peaks that arise solely via electron capture. The suppression of the electron capture lines demonstrates that, as expected, the beta detector is much more sensitive to positrons than gamma-rays.

The gamma energy in one of the four $E_1$ sensitive detectors is required to lie in of three energy gates. These gates are shown in Figure 4.7. The first gate is set from 750 to 950 keV and incorporates all of the 847 keV peak. The next gate is slightly larger and ranges from
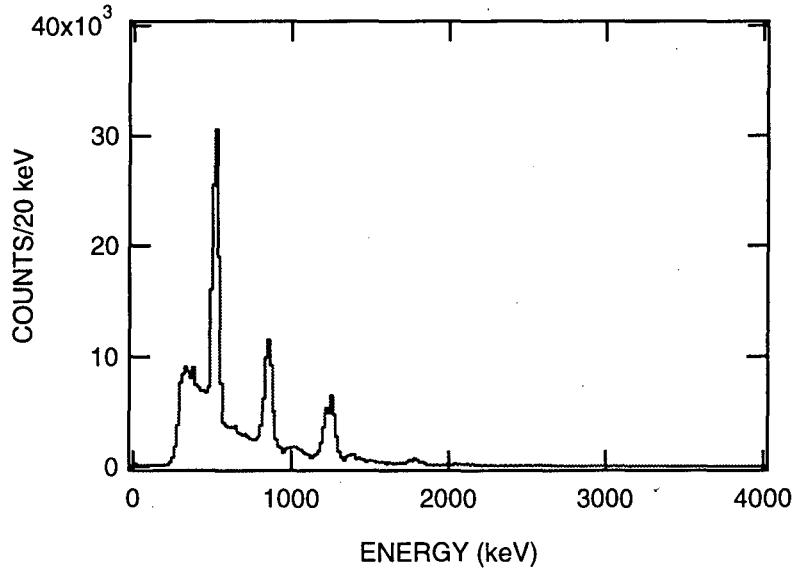
Figure 4.6: NaI(Tl) spectrum after requiring beta coincidence with $E_\beta > 350$ keV. Comparison with Figure 4.3 shows significant suppression of those peaks arising solely from electron capture decays.

1140 to 1460 keV. This energy window is wide enough to include the 1238 keV peak and the sum peak resulting from events where both the 847 keV gamma-ray and an annihilation photon entered the same detector. The final gate, from 1650 to 1850 keV, includes the other sum peak that results from the 1238 keV gamma-ray summing with the annihilation radiation. The events underneath the 847 keV peak mostly arise from Compton scattering of the 1238 keV gamma-ray. Since both gamma-rays contribute equally to the $T$ violating correlation, no subtraction of these events is necessary.

This gamma-ray energy cut differs from the approach used in the previous experiment[27]. In that analysis, gates were placed only around the two gamma-ray peaks and the sum peaks were ignored. The effect of neglecting the sum peaks for the method used in the present experiment is to introduce a slight efficiency dependence into the ratio $R$. In particular, if one considers events in a primary gamma-ray peak (either the 847 or 1238 keV peak), then the number of beta-gamma coincidences observed in a detector will be

$$N_\beta^i \propto \Omega_\beta \varepsilon_\beta \Omega_i \varepsilon_i(E_p)[1 - \Omega_i \varepsilon_i(E_a)][1 - f(\theta_i, T) + E_1 g(\theta_i, T)] \qquad (4.4)$$
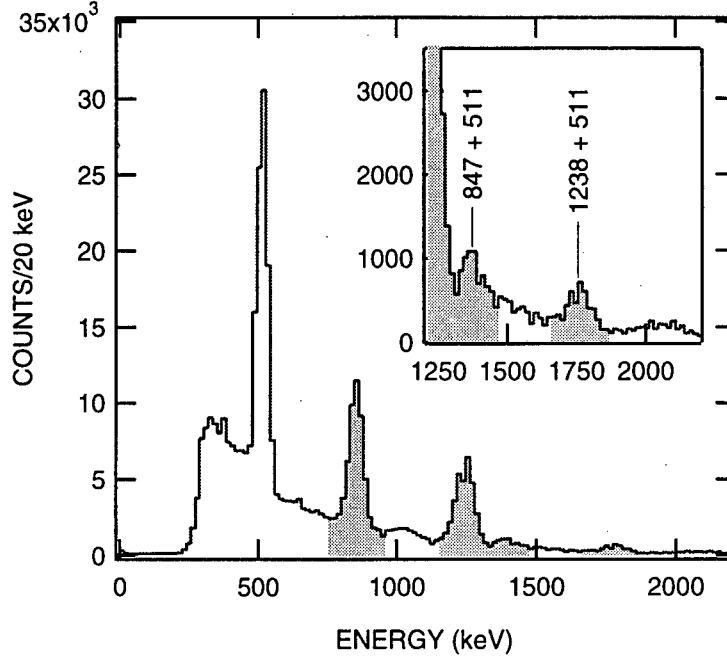
60

Figure 4.7: The gamma-ray energy gates used on the four $E_1$ detectors are shown in the shaded regions. The inset graph shows the sum peaks that are included with these energy cuts.

where $\varepsilon_1(E_p)$ and $\varepsilon_1(E_a)$ are the efficiencies for the NaI($Tl$) detector at the respective energies. The angular terms $f(\theta_i, T)$ and $g(\theta_i, T)$ are defined according to Equation 3.9. The term $[1 - \varepsilon_1(E_a)]$ accounts for the probability that a 511 keV annihilation photon will sum with the $E_p$ keV gamma and produce an event outside of the primary peak which will not be counted in $N_\beta^i$.

The equivalent expression for the annihilation-gamma events is somewhat different. Since the annihilation trigger relies upon the detection of the 511 keV photons in detectors 5-8, there is no annihilation radiation to sum with the gamma-rays recorded in detectors 1-4. Assuming that the annihilation trigger is perfect (i.e. that it is only triggered when the annihilation photons are detected in detectors 5-8), then the equivalent expression for Equation 4.4 is simply

$$N_\beta^i \propto \Omega_a \varepsilon_a \Omega_i \varepsilon_i(E_p)[1 - f(\theta_i, T)] \qquad (4.5)$$

where the term $[1 - \Omega_i \varepsilon_i(E_a)]$ has been dropped because the annihilation radiation was detected in detectors 5-8 and cannot sum with the primary gamma-ray. Now, when the ratio

$R$ is constructed according to Equation 3.21, the following term remains after simplification

$$R = \frac{[1 - \Omega_1\varepsilon_1(E_a)][1 - \Omega_3\varepsilon_3(E_a)]}{[1 - \Omega_2\varepsilon_2(E_a)][1 - \Omega_4\varepsilon_4(E_a)]} \frac{[1 - f(\theta_1,T)][1 - f(\theta_3,T)]}{[1 - f(\theta_2,T)][1 - f(\theta_4,T)]} \quad (4.6)$$
$$\times \frac{[1 - f(\theta_2,T)][1 - f(\theta_4,T)]}{[1 - f(\theta_1,T)][1 - f(\theta_3,T)]}$$
$$= \frac{[1 - \Omega_1\varepsilon_1(E_a)][1 - \Omega_3\varepsilon_3(E_a)]}{[1 - \Omega_2\varepsilon_2(E_a)][1 - \Omega_4\varepsilon_4(E_a)]}$$

Clearly, Equation 4.6 does not have to be unity, because it depends upon a ratio of efficiencies of different detectors. In order to circumvent this effect, it is necessary to include the sum peak in addition to the primary gamma-ray peak. By doing this, Equation 4.4 becomes

$$N_\beta^i \propto \Omega_\beta\varepsilon_\beta\Omega_i\varepsilon_i(E_p)[1 - \Omega_i\varepsilon_i(E_a)][1 - f(\theta_i,T) + E_1g(\theta_i,T)] \quad (4.7)$$
$$+ \Omega_\beta\varepsilon_\beta\Omega_i\varepsilon_i(E_p)\Omega_i\varepsilon_i(E_a)][1 - f(\theta_i,T) + E_1g(\theta_i,T)] \quad (4.8)$$
$$= \Omega_\beta\varepsilon_\beta\Omega_i\varepsilon_i(E_p)[1 - f(\theta_i,T) + E_1g(\theta_i,T)]. \quad (4.9)$$

Line 4.7 corresponds to the sum peaks. By re-capturing the summed events, the annihilation efficiency disappears from $N_\beta^i$ and with $E_1 = 0$, $R$ is again unity. This simple description contains implicit assumptions about the detector responses and the systematic uncertainties which are discussed in greater detail in Section 4.5.

The timing requirement for the beta-gamma coincidences is determined by histograming the time difference between beta and gamma events. A representative histogram is shown in Figure 4.8. The full-width half-maximum of the timing peak corresponds to a coincidence time resolution of 45 ns. This time resolution is limited by the slow beta detector timing signal. Events in the peak correspond to true coincidences and the flat background results from accidental coincidences. The ratio of true to accidental coincidences in the signal region is greater than 10:1. The asymmetric nature of the peak is due to pulse height dependent time slewing originating in the beta signals.

To assess whether or not it is necessary to correct for the accidental coincidences, a graph of the silicon pulse height as a function of the beta-gamma timing is shown in Figure 4.9. The
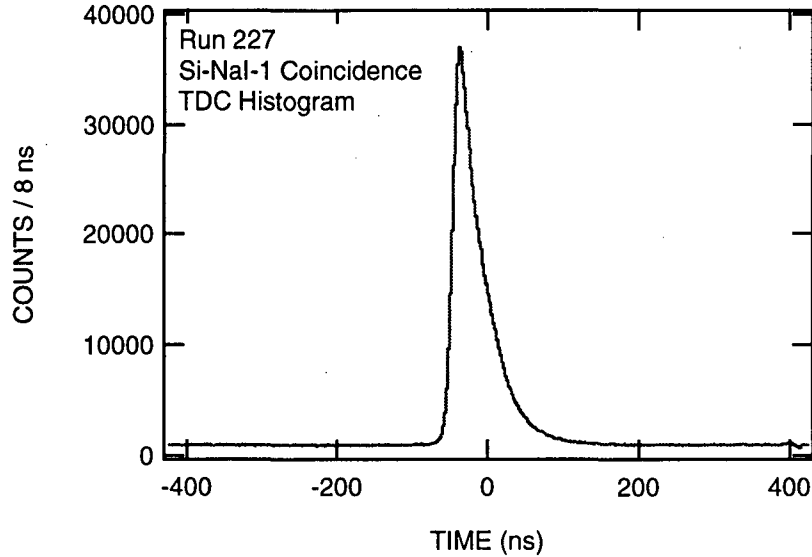
Figure 4.8: Beta-gamma coincidence TDC histogram. The FWHM of the timing peak corresponds to a coincidence time resolution of 45 ns.

previously mentioned requirement, $350 < E_\beta < 1850$ keV is shown as two solid horizontal lines in the figure. Clearly, the vast majority of the accidentals are eliminated by this requirement, indicating that most accidentals come from low energy beta pulses. Since the hardware threshold of the beta detector is set much lower than for the NaI($Tl$) detectors, this is expected. A 170 ns timing window is set, shown as the dashed vertical lines. In the region defined by the beta energy cut and this timing cut, the ratio of true to accidental coincidences is over 200:1. Accidentals are negligible and no subtraction is made in the analysis.

The annihilation-gamma event selection is based on three criteria similar to the beta-gamma event selection. These criteria include: the energy recorded in two back to back annihilation detectors, the gamma-ray energy recorded in one of the $E_1$ sensitive NaI($Tl$) detectors and the coincidence timing. A back to back annihilation trigger, requiring either detectors 5 and 7 or detectors 6 and 8 to be hit, is used to enhance the sensitivity to the annihilation radiation. In Figure 4.10, the energy recorded in back to back annihilation detectors is shown. The three bands that run parallel to both axes correspond to the three gamma-rays observed (511, 847, and 1238 keV). The events at the intersection of $E_5 \approx 511$
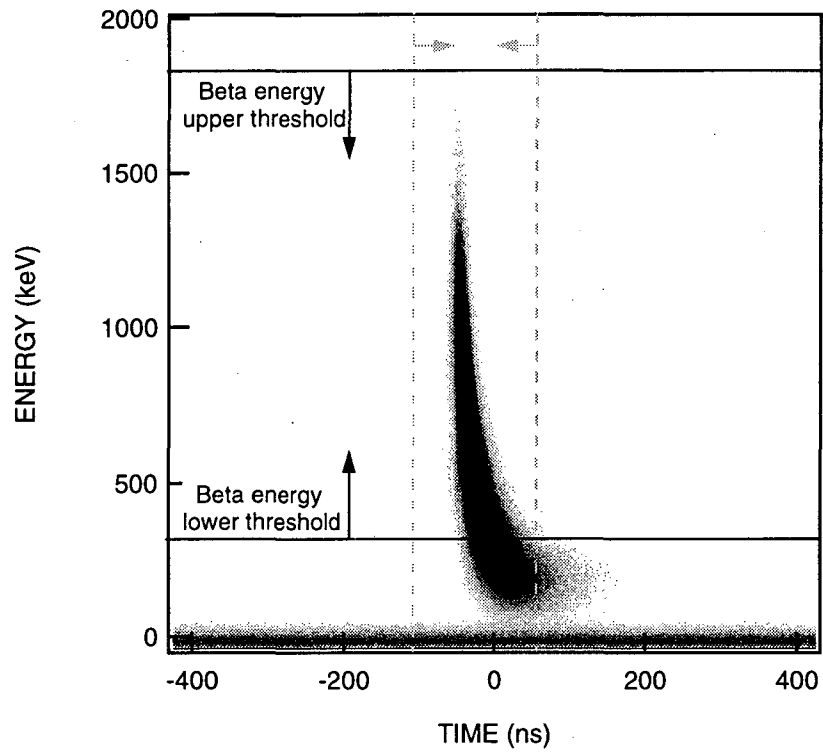
Figure 4.9: Beta energy vs. beta-gamma TDC. The horizontal lines correspond to the beta energy requirement $350 < E_\beta < 1850$ keV. The vertical lines represent a 170 ns timing window. In the region defined by these limits, the ratio of true to accidental coincidences is greater than 200:1.
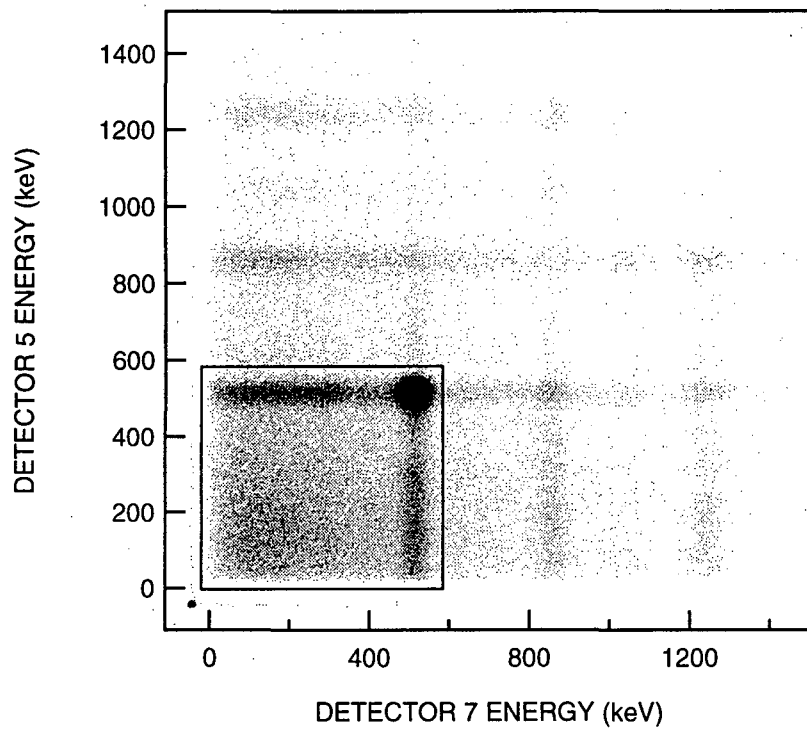
Figure 4.10: Gamma-ray energy recorded in back to back annihilation detectors 5 and 7. The boxed area indicates the energy requirement for annihilation identification of back to back events.
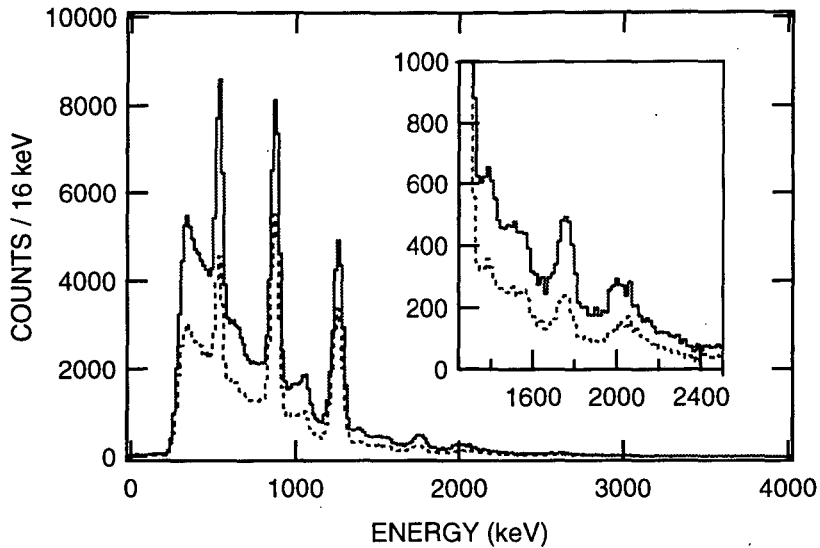
Figure 4.11: Gamma-ray energy recorded in detector 1 with requirement that back to back detectors 5 and 7 record $E_\gamma > 50$ keV (solid line) and with $50 < E_\gamma < 585$ keV (dashed line)

and $E_7 \approx 511$ keV clearly correspond to the annihilation radiation. The NaI($Tl$) spectrum from detector 1, after requiring this back to back condition is shown in Figure 4.11. The simple requirement that back to back detectors be triggered is not very precise. In particular, there is evidence of a 1037 keV peak in the spectrum and the inset of Figure 4.11 shows peaks at 1771 and 2035 keV. As shown in Figure 1.1, these cascades are $1771 \rightarrow 1238 \rightarrow 847$ keV (0.15 branch), $1037 \rightarrow 1238 \rightarrow 847$ keV (0.14 branch) and $2035 \rightarrow 1238 \rightarrow 847$ keV (0.08 branch). When the 1238 and 847 keV gamma-rays from these cascades are emitted back to back, the annihilation trigger could be satisfied while the first gamma-ray is recorded in detectors 1-4. To reduce these background coincidences, an energy gate of $50 < E_\gamma < 585$ is applied to the back to back detectors. This requirement is shown as a box in Figure 4.10. The effect this additional criteria has on the same NaI($Tl$) spectrum is shown as a dashed line in Figure 4.11. The electron capture peaks are suppressed as suspected. The residual contamination from the electron capture events is discussed in Section 4.4.

To maintain a consistent approach between the beta-gamma and annihilation-gamma coincidence analysis, the same energy gates are used for the $E_1$ sensitive detector. Since the summing with 511 keV photons is significantly suppressed, this wide interval is not necessary
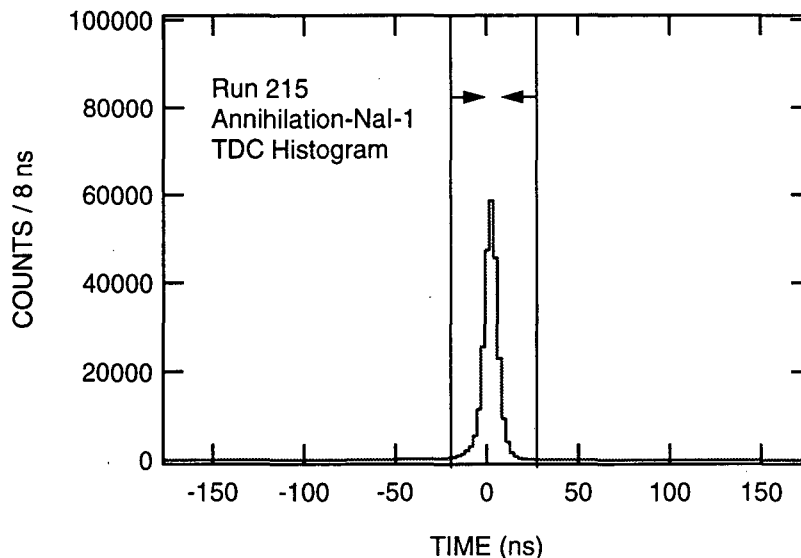
66

Figure 4.12: Annihilation-gamma coincidence TDC histogram. The 50 ns timing window used for the analysis is also shown.

to cover the sum peaks as it was in the beta-gamma coincidences. However, the cancellation of efficiencies in the $R$ of Equation 3.21 relies upon the efficiency for a given $E_1$ detector being the same for both the annihilation-gamma and beta-gamma coincidences. Since the sum windows used in the beta-gamma coincidences also include events where the 847 and 1238 keV gamma-rays summed in the same detector (an event which is equally possible for the annihilation-gamma coincidences), it is essential that the two different coincidence channels use the same analysis windows.

Figure 4.12 shows a typical timing peak for the annihilation-gamma coincident events. The full-width half-maximum of the timing peak corresponds to a coincidence time resolution of 25 ns. Events in the peak correspond to true coincidences whereas the flat background results from accidental coincidences. The ratio of true coincidences to accidentals is greater than 250:1. The timing window shown in Figure 4.12 is used with no further correction for accidentals.

With all of the criteria applied, it is now possible to compute $R$ for each run. The result is shown in Figure 4.13. In Figure 4.14 the deviation of $R$ from unity, normalized by the statistical error for each run, is histogrammed. The distribution is symmetric with a
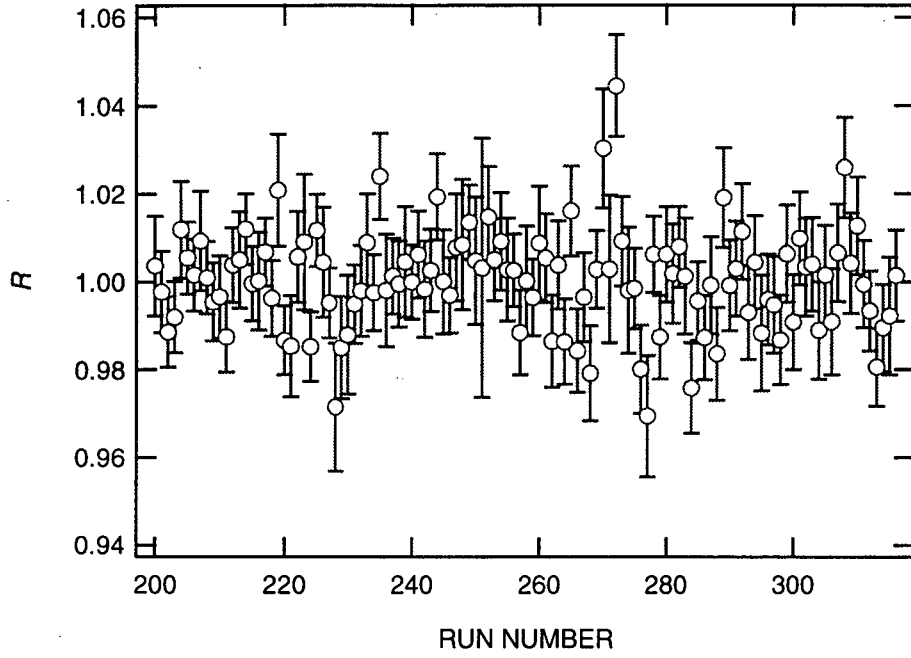
Figure 4.13: $R$ as a function of run number. The variation in error bars is due to different run lengths.
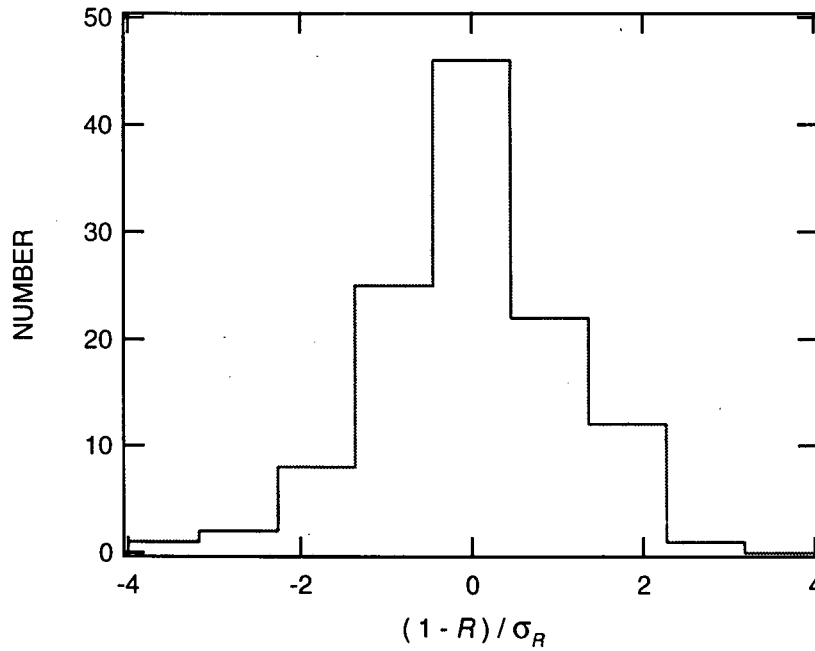


Figure 4.14: Histogram of $(1 - R)/\sigma_R$.

standard deviation near 1 as expected.

The only remaining step is the computation of the sensitivity factor $\kappa(\theta, T)$ for each run. Since the temperature varied over the course of the experiment, it is not possible to take a simple weighted average of $R$ and apply a single value of $\kappa(\theta, T)$ to it. This calculation is discussed in the next section.

## 4.4  Determination of $E_1$

According to the simple expression of Equation 3.24, the sensitivity factor is given by

$$\kappa(\theta, T) = \frac{g(\theta, T)}{1 - f(\theta, T)}. \tag{4.10}$$

This expression does not account for a number of additional experimental factors including: backscattered positrons, beta-gamma background contributions, and finite detector solid angles.

Backscattered events arise from instances where the positron was initially emitted into the source crystal and away from the beta detector. Some fraction $\eta$ of the these positrons then undergo large angle scattering by a cobalt nucleus and are subsequently recorded in the beta detector. For the beta-gamma coincidences, these backscattered positrons can be taken into account through a slight modification of Equation 3.9 to read

$$W_\beta(\theta, T) \propto 1 - f(\theta, T) + E_1 g(\theta, T) + \eta[1 - f(\theta, T) - E_1 g(\theta, T)]. \tag{4.11}$$

Here, $\eta$ represents the backscatter probability. Since the backscattered positrons have a momentum opposite to those positrons normally incident on the beta detector, they will have the opposite contribution to the $E_1$ correlation as reflected in Equation 4.11. This opposite sign dilutes the experimental sensitivity. The backscattering fraction from various materials has been studied as a function of $Z$ and incident energy[50]. For cobalt ($Z = 27$), the backscattered fraction is estimated to be $\eta \approx 0.34$. A simple model of backscattering is illustrated in Figure 4.15. This model represents the energy deposited in the cobalt
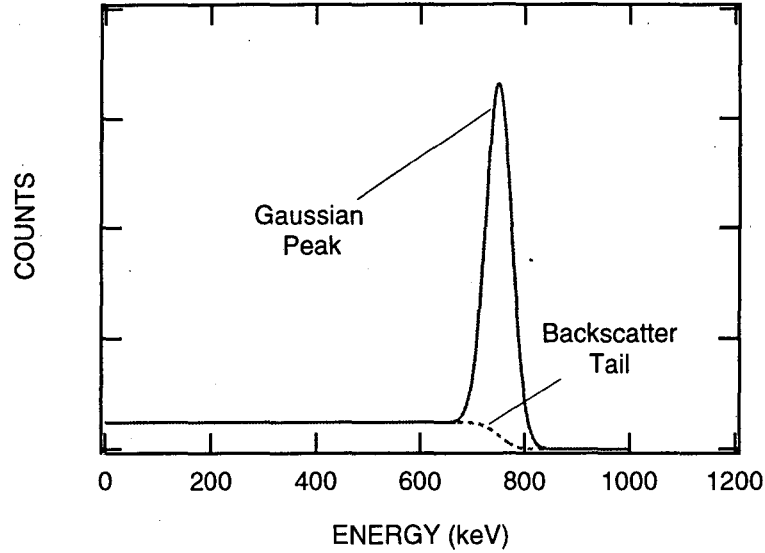
Figure 4.15: Mono-energetic model of backscattering. The spectrum shown is that of the energy deposited in the backscattering material. A complementary energy spectrum is then incident on the beta detector.

and includes a gaussian peak with a flat tail that extends from zero to the peak energy as shown. The backscattered events incident on the beta detector have a complementary energy spectrum. Taking the allowed beta spectrum and convoluting it with this model, one has

$$dN(E) \propto \int F(Z, E')pE'(E_0 - E')R(E', E)dE'dE, \qquad (4.12)$$

where $p$ and $E$ are the beta momentum and energy and $F(Z, E')$ is the Fermi function. The backscattering model is contained in the term $R(E', E)$. The result of this integration is shown in Figure 4.16. The effect of the backscattering is to move events to lower energies. Based upon this simple model, approximately 0.45 of the backscattered events are reduced to an energy below the threshold ($E_\beta > 350$ keV) indicated in the figure. This compares with only 0.22 of the beta spectrum that is normally below threshold. Therefore, the backscattering correction that is relevant for Equation 4.11 is reduced to

$$\eta_t = \frac{(1 - 0.45)}{(1 - 0.22)} \times 0.34 = 0.24. \qquad (4.13)$$

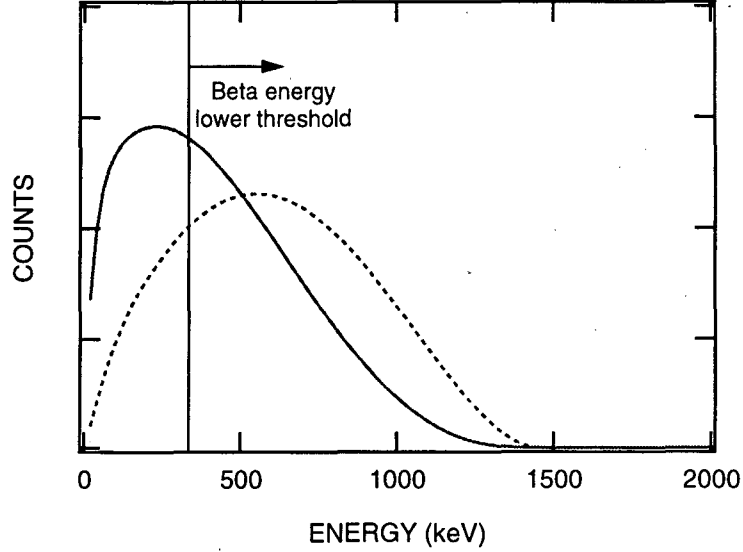where $\eta_t$ is the backscattered fraction above threshold.

70

Figure 4.16: Effect of backscattering on beta spectrum. The solid line is the $^{56}$Co beta spectrum corrected for finite energy resolution and backscattering from the cobalt crystal. The dashed line is the beta spectrum without any backscattering correction. The vertical line indicates the low energy threshold used in the analysis.

Another important modification of the sensitivity factor $\kappa$ is due to background coincidence events. In particular, background coincidences arise from gamma-ray interactions in the beta detector primarily from Compton scattering. The background contribution can be characterized by modifying Equation 4.11 with a single quantity $B_\beta$:

$$W_\beta(\theta, T) \propto 1 - f(\theta, T) + E_1 g(\theta, T) + \eta_t[1 - f(\theta, T) - E_1 g(\theta, T)] + B_\beta. \qquad (4.14)$$

The term $B_\beta$ will also dilute the sensitivity to $E_1$. The estimate of $B_\beta$ was obtained by fitting the observed beta spectrum. The allowed beta decay shape is

$$dN \propto F(Z, E) p E (E_0 - E) dE. \qquad (4.15)$$

This is multiplied by an instrumental correction factor

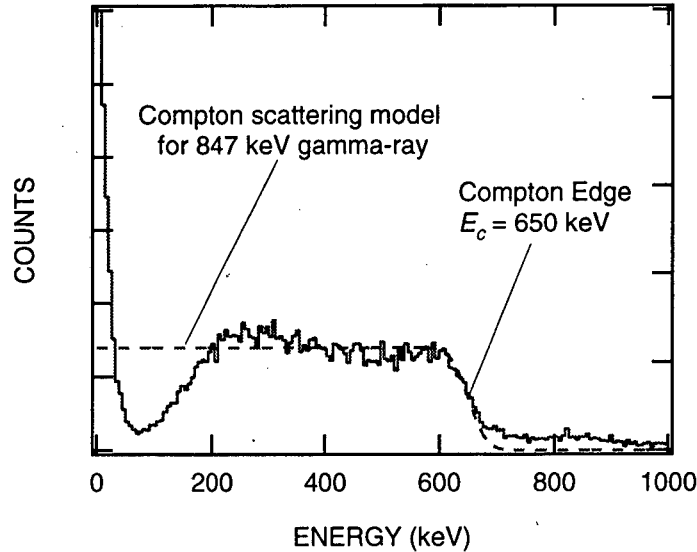$$S(E) = 1 + aE + bE^2, \qquad (4.16)$$

71

Figure 4.17: Model used for fitting the 847 keV Compton spectrum (dashed line). The solid line is the measured Compton spectrum that has been enhanced by gating on higher energy gamma-rays in the NaI($Tl$) detectors.

where $a$ and $b$, are treated as unknown parameters. The Compton spectrum arising from gamma-ray interactions in the beta detector is modeled by a simple flat tail located at the appropriate energy as shown in Figure 4.17. This characterization fits reasonably well to the measured spectrum as shown. Using this Compton scattering model together with the modified allowed beta spectrum shape, a fit to the spectrum gives a determination of the gamma-ray background fraction. The result of this procedure for a single run is shown in Figure 4.18.

The reduced chi-square for the fit is $\chi^2_\nu = 1.1$ and the background is $B_\beta = 0.133 \pm 0.015$. Using this fitting procedure over several runs, the results shown in Table 4.2 are obtained. The beta-gamma background is determined to be

$$B_\beta = 0.123 \pm 0.005 \tag{4.17}$$

The final correction for the finite detector solid angles requires an integration of the angular distribution terms over the faces of the beta and gamma-ray detectors. For com-
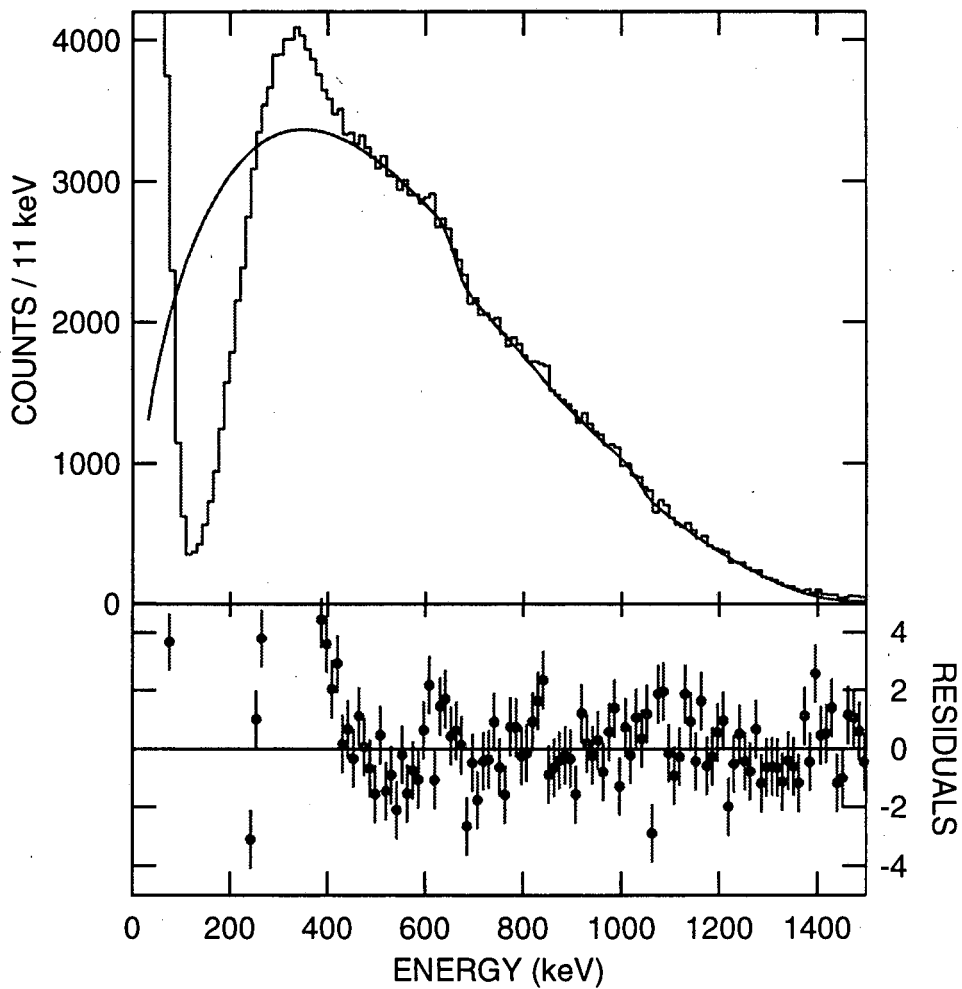
Figure 4.18: Fitting of the beta spectrum to determine background $B_\beta$. The top section shows the data and a fit according to the model described in the text. The fitted interval is from 450 to 1500 keV and the normalized residuals are shown in the bottom section. The reduced chi-square for this fit is $\chi^2_\nu = 1.1$ and the background is $B_\beta = 0.133 \pm 0.015$.

| Parameter | Value |
| --- | --- |
| $N$ | $109 \pm 5$ |
| $a$ | $(-12 \pm 0.35) \times 10^{-4}$ (keV)$^{-1}$ |
| $b$ | $(49 \pm 3) \times 10^{-8}$ (keV)$^{-2}$ |
| $B_\beta$ | $0.123 \pm 0.005$ |

Table 4.2: Average of results from background analysis. The free parameters are defined as follows: $N$ is the overall beta spectrum normalization, $a$ and $b$ are the instrumental shape factors and $B_\beta$ is the background fraction.

pactness, this will be denoted by an overbar so that Equation 4.14 becomes

$$W_\beta(\theta, T) \propto 1 - \bar{f}(\theta, T) + E_1 \bar{g}(\theta, T) + \eta_t[1 - \bar{f}(\theta, T) - E_1 \bar{g}(\theta, T)] + B_\beta. \tag{4.18}$$

The calculation of the solid angle corrections is described in Appendix A.

The annihilation-gamma coincidences are insensitive to $E_1$ and do not have any dependence on the backscattered positrons. Hence, the equivalent expression to Equation 4.18 for the annihilation-gamma coincidences is simply

$$W_a(\theta, T) \propto 1 - \bar{f}(\theta, T) + B_a, \tag{4.19}$$

where $B_a$ represents the annihilation-gamma background.

Substituting these expressions into the $R$ of Equation 3.21, and assuming that $\theta_1 = -\theta_2 = \theta_3 = -\theta_4$, one has

$$\sqrt{R} = \frac{[(1 + \eta_t)(1 - \bar{f}(\theta, T)) + E_1(1 - \eta_t)\bar{g}(\theta, T) + B_\beta]}{[(1 + \eta_t)(1 - \bar{f}(\theta, T)) - E_1(1 - \eta_t)\bar{g}(\theta, T) + B_\beta]} \tag{4.20}$$

$$\times \frac{[(1 + \eta_t)(1 - \bar{f}(\theta, T)) + B_a]}{[(1 + \eta_t)(1 - \bar{f}(\theta, T)) + B_a]} \tag{4.21}$$

$$= \frac{[(1 + \eta_t)(1 - \bar{f}(\theta, T)) + E_1(1 - \eta_t)\bar{g}(\theta, T) + B_\beta]}{[(1 + \eta_t)(1 - \bar{f}(\theta, T)) - E_1(1 - \eta_t)\bar{g}(\theta, T) + B_\beta]}.$$

With this approximation, there is no dependence on the annihilation-gamma background
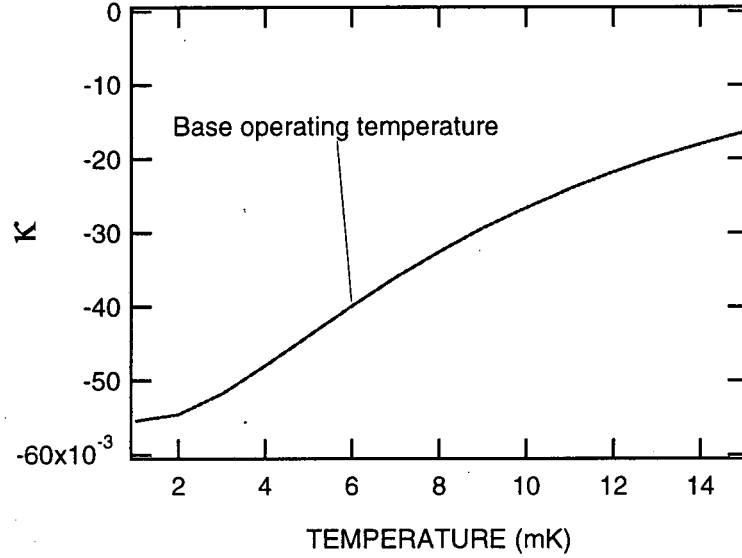
Figure 4.19: Sensitivity factor $\kappa$ as a function of temperature. Corrections for finite solid angles, positron backscattering and background coincidences are included.

$B_a$. This is expected since the primary function of the annihilation ratio $R_a$ is to cancel the efficiencies of the various detectors. This can be done by triggering on any events in coincidence with the $E_1$ detectors. It is only the cancellation of the angular misalignment that is sensitive to the origin of coincidence events. The expression for $E_1$ given by Equation 3.24 becomes

$$E_1 \frac{(1 - \eta_t)\bar{g}(\theta,T)}{(1 + \eta_t)(1 - \bar{f}(\theta,T)) + B_\beta} = \frac{1 - \sqrt{R}}{1 + \sqrt{R}}. \tag{4.22}$$

So that the full expression for $\kappa$ is

$$\kappa(\theta,T) = \frac{(1 - \eta_t)\bar{g}(\theta,T)}{(1 + \eta_t)(1 - \bar{f}(\theta,T)) + B_\beta} \tag{4.23}$$

and it is possible to compute the experimental sensitivity. Taking $\theta = 45°$, the sensitivity factor as a function of temperature is shown in Figure 4.19. At the base temperature attained during the run, the sensitivity factor is $\kappa \approx 0.04$. Applying the sensitivity factor to the value of $R$ measured from the individual runs, a value of $E_1$ is obtained for each run. The result is shown in Figure 4.20. The combined result, $E_1 = -0.001 \pm 0.005$, is consistent with no $T$ violation. The reduced chi-square for this fit is $\chi_\nu^2 = 1.01$. The
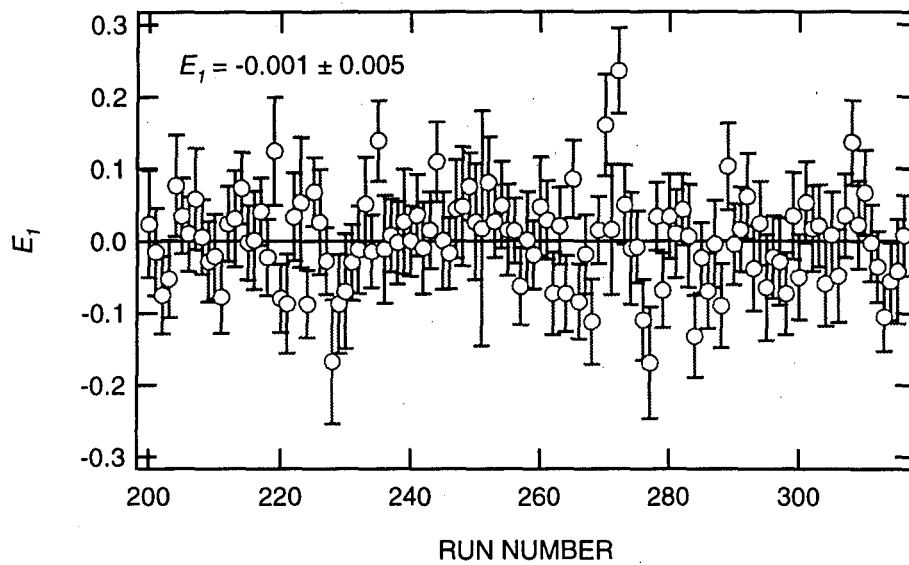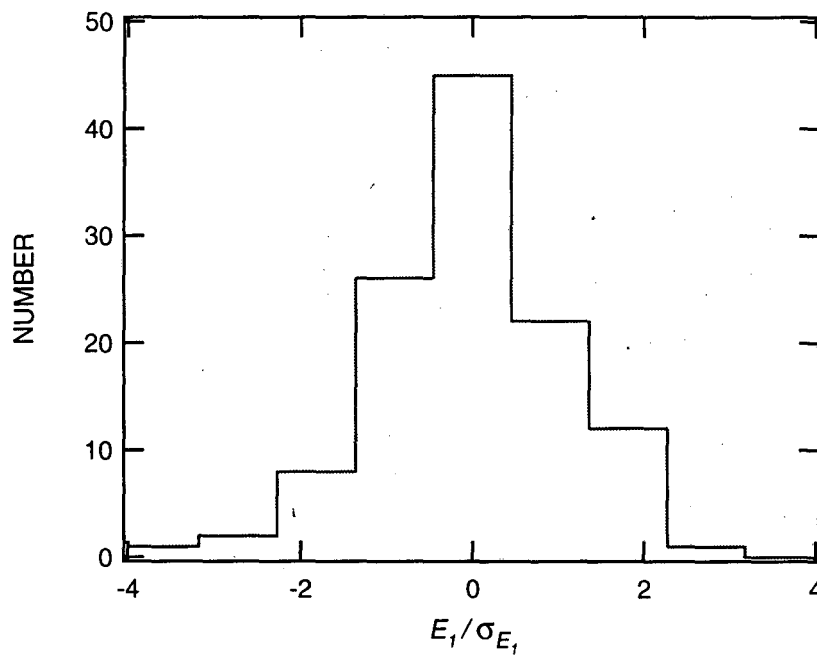
Figure 4.20: $E_1$ versus run number.



Figure 4.21: Histogram of $E_1/\sigma_{E_1}$.

values of $E_1$ are normalized by the corresponding statistical error and histogrammed in Figure 4.21. The distribution is symmetric with a standard deviation near unity as expected. The interpretation of this result in terms of a $T$ violating phase and possible systematic contributions are discussed in the following sections.

## 4.5   Systematic Contributions to $E_1$

There are two main sources of systematic uncertainty in this measurement. The first is due to the 511 keV photons summing with either the 1238 or 847 keV gamma-rays, and the second is due to higher order terms in $R$ that depend upon the product of background contributions and array misalignment. Both of these effects can cause $R$ to deviate from unity and lead to a false $E_1$.

As noted earlier, the 511 keV summing effect gives rise to a possible difference between the beta-gamma and annihilation-gamma coincidences. Since the annihilation-gamma coincidences rely on the observation of the 511 keV photons in other detectors, the likelihood of 511 keV summing in the primary gamma-ray detectors is suppressed. This is not the case for the beta-gamma coincidences, which exhibit an appreciable amount of summing with the 511 keV photons. This difference between the beta-gamma and annihilation-gamma coincidences is addressed through the inclusion of the "sum peak" windows in the gamma-ray energy cut. This approach is exact in the limit that the NaI detector response is a delta function at the incident energy. In this limit, the only possible observable energies are the total primary gamma-ray energy or the total primary gamma-ray energy summed with the total annihilation energy. These two possibilities are addressed with the two different energy windows used in the analysis: the peak and sum peak windows. What is neglected is the possibility that a partial energy deposition will occur which removes an event from the primary gamma-ray energy peak, but does not record an energy equal to the sum peak energy. The extent to which the probability of this effect depends upon the individual detector will give rise to a false $E_1$. To understand this contribution to the systemmatic uncertainty, a more thorough treatment of the summing effect is discussed below.

For simplicity, consider a single primary gamma-ray (either the 847 or 1238 keV gamma-

ray) and an annihilation photon. According to the analysis approach used here, there are two energy windows for each primary gamma-ray, one around the peak energy of the primary gamma-ray $E_p$, and the other around the sum peak energy $E_p + E_a$. The number of beta-gamma events recorded in a NaI($Tl$) detector can be expressed as integrals over these two different energy windows.

$$N_\beta^i \propto \int_{E_p-\Delta}^{E_p+\Delta} dE' \left\{ \int_0^{E_p} dE_p' \varepsilon_i(E_p, E_p') \delta(E' - E_p')[1 - \varepsilon_i^T(E_a)] \right. \tag{4.24}$$

$$+ \int_0^{E_p} dE_p' \int_0^{E_a} dE_a' \varepsilon_i(E_p, E_p') \varepsilon_i(E_a, E_a') \delta(E_1' + E_a' - E') \right\} \tag{4.25}$$

$$+ \int_{E_p+E_a-\Delta}^{E_p+E_a+\Delta} dE' \left\{ \int_0^{E_p} dE_p' \varepsilon_i(E_p, E_p') \delta(E' - E_p')[1 - \varepsilon_i^T(E_a)] \right. \tag{4.26}$$

$$+ \int_0^{E_p} dE_p' \int_0^{E_a} dE_a' \varepsilon_i(E_p, E_p') \varepsilon_i(E_a, E_a') \delta(E_1' + E_a' - E') \right\} \tag{4.27}$$

where the width of the energy window is $2\Delta$. Common factors related to the angular distribution terms and solid angles have been suppressed for compactness. The annihilation radiation is assumed to be isotropic. The term $\varepsilon(E, E')$ is a transfer function containing information about the NaI($Tl$) detector response. For a given incident energy $E$, $\varepsilon(E, E')$ represents the probability that an energy $E'$ is recorded. The total probability, or efficiency, integrated over all observable energies is denoted by $\varepsilon_1^T(E)$. Equations 4.24 and 4.26 correspond to events where the primary gamma ray is detected without any contribution from the annihilation photon. In effect, line 4.26 is negligible, since there are no events in the sum energy window that arise from the primary gamma-ray alone. Equations 4.25 and 4.27 are the corresponding expressions for events with both the primary gamma-ray and annihilation radiation signals.

These expressions should be compared against the corresponding ones for the annihilation-gamma coincidences. In the earlier discussion of the summing effect, it was assumed that the annihilation trigger was perfect (i.e. it only was satisfied by 511 photons). In this case, there are no annihilation photons to sum with the primary gamma-rays. In reality, the annihilation trigger is imperfect and there are some annihilation photons to sum with the primary gamma-rays. For example, the annihilation trigger can be satisfied by a single

511 photon being detected in coincidence with a partial energy deposition of either the 847 or 1238 keV gamma-ray. The remaining annihilation photon and primary gamma-ray can then sum together in a single detector. Since the same energy windows are used for the annihilation-gamma coincidences, a similar integral expression can be used to represent the number of events recorded in a NaI($Tl$) detector.

$$N_a^i \propto \int_{E_p-\Delta}^{E_p+\Delta} dE' \left\{ \int_0^{E_p} dE_p' \varepsilon_i(E_p, E_p')\delta(E'-E_p')[1 - \xi\varepsilon_i^T(E_a)] \right. \tag{4.28}$$

$$+ \xi\int_0^{E_p} dE_p' \int_0^{E_a} dE_a' \varepsilon_i(E_p, E_p')\varepsilon_i(E_a, E_a')\delta(E_1' + E_a' - E') \right\} \tag{4.29}$$

$$+ \int_{E_p+E_a-\Delta}^{E_p+E_a+\Delta} dE' \left\{ \int_0^{E_p} dE_p' \varepsilon_i(E_p, E_p')\delta(E'-E_p')[1 - \xi\varepsilon_i^T(E_a)] \right. \tag{4.30}$$

$$+ \xi\int_0^{E_p} dE_p' \int_0^{E_a} dE_a' \varepsilon_i(E_p, E_p')\varepsilon_i(E_a, E_a')\delta(E_1' + E_a' - E') \right\} \tag{4.31}$$

Here the only difference from the beta-gamma coincidences is the inclusion of the factor $\xi$ wherever the annihilation radiation terms appear. The most conservative estimate of this systematic effect is obtained with $\xi = 0$, in which case there is no summing contribution in the annihilation-gamma coincidences. This assumption maximizes the difference between the annihilation-gamma and beta-gamma coincidences and therefore maximizes any possible systematic contribution.

To evaluate these expressions for the beta-gamma and annihilation-gamma coincidences, it is necessary to assume a model for the NaI($Tl$) detector response $\varepsilon(E, E')$. The detector response is determined by comparing it with measured spectra. The functional form used is simply a gaussian peak combined with a flat tail that extends from zero to the Compton edge. This model is shown in comparison to a measured beta-gamma coincidence spectrum in Figure 4.22. The fit is not very good, but evaluation of a possible systematic contribution to $E_1$ is not sensitive to slight refinements of this model. This was verified by evaluating the systemmatic with a variety of response models supported by the measured spectra. The energy dependence of this model is based upon tabulated data for NaI($Tl$) detectors[52]. For simplicity, each detector is assumed to have the same response shape with an overall relative efficiency determined by measurements above 100 mK. To be complete, it is necessary to
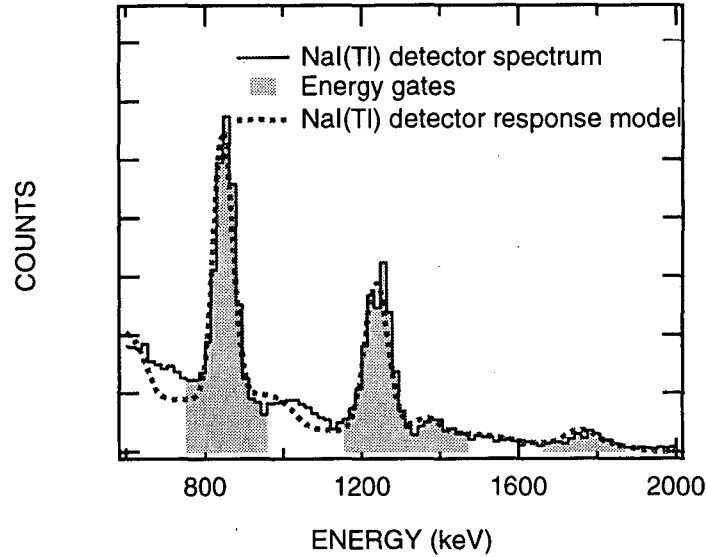
Figure 4.22: Detector response model used for NaI(*Tl*) detectors. The energy gates used in the analysis are shown as a shaded region.

include the contribution from summing events where both the 847 and 1238 keV gamma-ray enter the same detector. This summing occurs for both the annihilation-gamma and beta-gamma coincidences. A fraction of these sum events will be recorded in one of the primary or sum peak windows.

Calculations according to this model are shown in Table 4.3. Three different calculations, each with a different value of $\xi$ is shown. As expected, the systematic contribution is largest with $\xi = 0$ and equal to zero with $\xi = 1$. Taking the conservative approach with $\xi = 0$, the systematic contribution to $E_1$ is set at 2.2 $\times 10^{-3}$. This compares with a statistical error for $E_1$ of 5.0 $\times 10^{-3}$. Methods for further reducing and possibly eliminating this systematic uncertainty is discussed in Appendix B.

The second source of systematic uncertainty arises from a product of the array mis-alignment and background contributions. In the development of Equation 4.22, background contributions were considered in the limit that the detector array was perfectly aligned. If the array misalignment is characterized by a single angle $\delta$ as shown in Figure 4.23, then

80

|     $\xi$ | Systematic Contribution ($\times 10^{-3}$) |
|-----------|--------------------------------------------|
| 0         | 2.2                                        |
| 0.1       | 2.0                                        |
| 0.2       | 1.7                                        |
| 1.0       | 0.0                                        |

Table 4.3: Calculation of systematic contribution to $E_1$ due to annihilation radiation summing. Values for different inputs of $\xi$ are shown. With $\xi = 1$, there is no difference between the beta-gamma and annihilation-gamma coincidences so the systematic contribution is zero.

the following corrections to the angular terms entering $R$ can be considered

$$\bar{f}(\theta_1, T) = \bar{f}(\theta - \delta, T) \approx \bar{f}(\theta, T) - \overline{\delta f} \tag{4.32}$$

$$\bar{f}(\theta_2, T) = \bar{f}(\theta + \delta, T) \approx \bar{f}(\theta, T) + \overline{\delta f} \tag{4.33}$$

$$\bar{f}(\theta_3, T) = \bar{f}(\theta - \delta, T) \approx \bar{f}(\theta, T) - \overline{\delta f} \tag{4.34}$$

$$\bar{f}(\theta_4, T) = \bar{f}(\theta + \delta, T) \approx \bar{f}(\theta, T) + \overline{\delta f} \tag{4.35}$$

where $\theta = 45°$ and $\overline{\delta f}$ represents the small difference due to angular misalignment integrated over the finite detector solid angle. Although similar expressions could be used for the $T$ violating distribution term $g(\theta, T)$, this would involve the negligible product of $E_1$ and the array misalignment. Inserting these expressions along with the background contribution terms $B_a$ and $B_\beta$ into the equation for $R$, the following approximate expression is obtained

$$\frac{1 - \sqrt{R}}{1 + \sqrt{R}} = \frac{(1 - \eta_t)\bar{g}(\theta, T)}{(1 + \eta_t)[1 - \bar{f}(\theta, T)] + B_\beta} \tag{4.36}$$

$$\times \left\{ E_1 + \frac{\overline{\delta f}(B_a - B_\beta)}{[(1 - \eta_t)\bar{g}(\theta, T)][1 - \bar{f}(\theta, T) + B_a]} \right\} \tag{4.37}$$

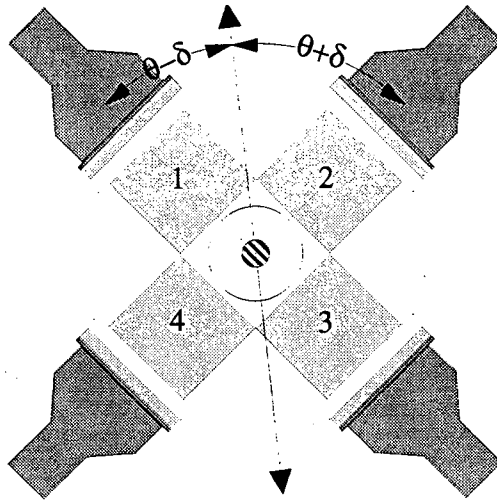The first term in line 4.37 is the familiar $T$ violating contribution that is proportional to

Figure 4.23: Array misalignment characterized by single angle $\delta$.

$E_1$. The second term is not proportional to $E_1$ and is a source of systematic uncertainty. It involves the product of the array misalignment and a difference in the background contributions from the annihilation-gamma coincidences and the beta-gamma coincidences. Since this term is not proportional to $E_1$, it can be present even if $E_1$ is equal to zero. A conservative estimate of the maximum size of this term can be obtained by setting $B_a = 0$. Using the measured array misalignment of $\delta = -0.2°$ and the measured background $B_\beta = 0.123$, the magnitude of this term is $\approx 4 \times 10^{-3}$.

To obtain a better estimate of this systematic error it is necessary to determine the annihilation-gamma coincidence background $B_a$. The annihilation-gamma background coincidences primarily arise from electron capture events that are followed by a gamma-ray cascade. In general, only cascades with 3 or more gamma-rays will contribute to this background. Two gamma-rays are required to activate the annihilation trigger and the third must enter an $E_1$ sensitive detector. The most significant cascades with 3 or more gamma-rays are 1771 → 1238 → 847 keV (0.9 relative to positron branch), 1038 → 1238 → 847 keV (0.53 relative to positron branch) and 2035 → 1238 → 847 keV (0.42 relative to positron branch). Up to the variation in the NaI(Tl) detector efficiencies, these background events

82

are isotropic when averaged over all possible detector combinations.

Two different approaches were used to determine $B_a$. The first approach uses the event mode data, while the second is a calculation based on simple models of the detector response previously used for the summing simulation. To determine the annihilation-gamma background from the event mode data, an 150 keV energy gate was placed around the 1771 keV gamma-ray peak in the $E_1$ sensitive NaI($Tl$) detectors. Using this subset of events, the annihilation detectors were inspected for events that satisfied the annihilation criteria used ($50 < E_\gamma < 585$ keV in two back to back detectors). Since the 1771 keV gamma-ray is followed by a cascade of the 1238 and 847 keV gamma-rays, these events measure the tendency to mislabel the 1238 and 847 keV gamma-rays as annihilation photons. The relative efficiency for the 1771 keV gamma-ray was canceled by using singles data acquired simultaneously with the coincidence data. Using this information, it is possible to predict the background contributions from other gamma-ray combinations provided one assumes that the spectrum shape at energies below 600 keV is similar for the different energy gamma-rays. An identical, independent approach was used for the 2035 keV peak that also cascades to the 1238 and 847 keV gamma-rays. The results of these measurements are shown in Table 4.4.

There are some limitations to this approach. The main difficulty stems from the inability to resolve distinct energy peaks from sum peaks. For example, it is not possible to resolve the 1771 keV peak from a possible sum peak at 1749 keV (arising from the a 1238 keV gamma-ray summing with a 511 keV photon) given the energy resolution of the NaI($Tl$) detectors. The 2035 keV peak is less susceptible to this effect since it is beyond the summing window with 511 keV photons. The result of including these additional events is to over-estimate the annihilation-gamma background $B_a$. In fact, as shown in Table 4.4, the background deduced by using the 2035 keV peak is less than that deduced using the 1771 keV peak. This is qualitatively expected since the 2035 keV peak is less susceptible to pollution from sum events. Although more exotic combinations of event requirements can be used to reduce the summing probability, the remaining statistical sample is too weak to provide a useful estimate of $B_a$.

Based on the slight discrepancy between the results obtained using the 2035 keV line

| Method | $B_a$ |
|---|---|
| 1771 keV line | $0.150 \pm 0.005$ |
| 2035 keV line | $0.135 \pm 0.005$ |
| Calculation | $0.110 \pm 0.010$ |

Table 4.4: Annihilation-gamma background determination using three different approaches. The errors quoted for the 1771 keV and 2035 keV line methods are statistical. The error quoted for the calculation is based upon random variation of input parameters.

and the 1771 keV line, an additional independent approach to determine $B_a$ was desired. To this end, a simulation of the detector geometry was performed. For the NaI($Tl$) detector response, a model identical to that previously used for the summing model was used. For energy dependent efficiencies, tabulated values for NaI($Tl$) detectors were used[52]. To simulate realistic variation from these tabulated values, all parameters for each detector were allowed to randomly fluctuate at a level of 10%. The result of this simulation, is shown in Figure 4.24. From this simulation, an annihilation-gamma background fraction of $B_a = 0.11 \pm 0.01$ is obtained.

The three different values in Table 4.4 represent the degree of certainty that $B_a$ can be known. Taking an unweighted mean of these values and using the range of values as an estimate of the variance, the background $B_a$ is determined to be

$$B_a = 0.13 \pm 0.04 \qquad (4.38)$$

Using this number and its associated variance, it is possible to better estimate the systematic contribution this effect has on a measurement of $E_1$. Assuming that the angular misalignment, beta-gamma background and annihilation gamma-background are independent, the systematic contribution to $E_1$ in Equation 4.37 is estimated to be

$$\frac{\overline{\delta f}(B_a - B_\beta)}{[(1 - \eta_t)\bar{g}(\theta, T)][1 - \bar{f}(\theta, T) + B_a]} = 0.000 \pm 0.003. \qquad (4.39)$$
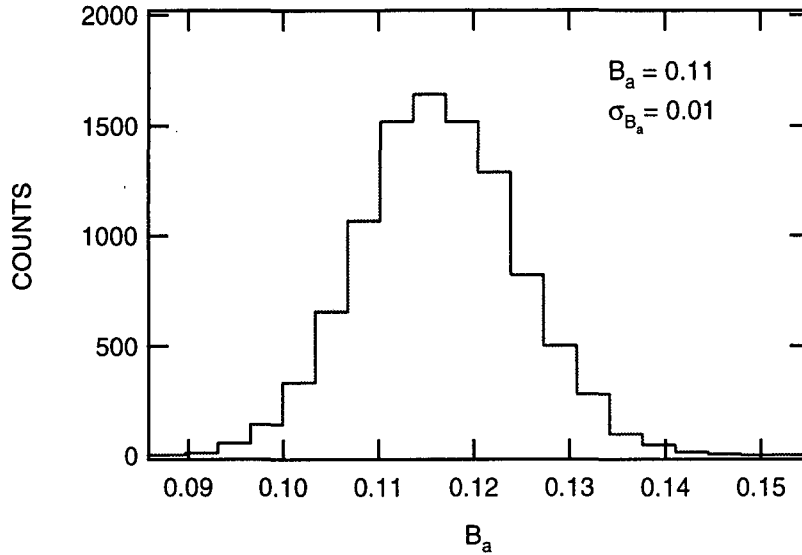
Figure 4.24: Histogram of simulation to determine $B_a$. Annihilation energy requirement is $50 < E_\gamma < 585$ in back to back detectors. The width of the histogram is due to random input values for the NaI($Tl$) detector characteristics.

It is worth noting that the beta-gamma background ($B_\beta = 0.123 \pm 0.005$) is nearly equal to the annihilation-gamma background ($B_a = 0.13 \pm 0.02$). This has the effect of minimizing the previously mentioned systematic contribution. To provide a final check on this fortuitous coincidence, the data was analyzed with a more strict annihilation trigger criteria. Instead of requiring back to back detectors to have an energy $50 < E_\gamma < 585$ keV, an energy cut that only included the 511 keV peaks was used ($435 < E_\gamma < 585$ keV). This energy requirement reduces the statistical power of the data while also significantly suppressing the annihilation-gamma background. By suppressing the annihilation-gamma background, the difference between $B_a$ and $B_\beta$ is enhanced and so too the systematic contribution in Equation 4.39. According to the same background determination methods listed in Table 4.4, the annihilation-gamma background is reduced by over an order of magnitude when this "peak" cut is used. The result for $E_1$ from this "peak" analysis is found to be

$$E_1 = -0.006 \pm 0.008. \tag{4.40}$$

This result is also consistent with no $T$ violation. However, its central value is more neg-

| Source | Uncertainty |
|---|---|
| Statistical | 0.005 |
| Summing correction | 0.002 |
| Misalignment × Background correction | 0.003 |
| Temperature variation during single run | < 0.001 |
| Gain variation during single run | < 0.001 |
| Non-uniform beta-detector efficiency | < 0.001 |

Table 4.5: Measurement uncertainties for $E_1$.

ative than the original result of $E_1 = -0.001 \pm 0.005$. This is precisely the direction the systematic term in Equation 4.39 predicts the result should move as $B_a$ is reduced toward zero. Although the difference between the two results is not statistically significant, it is a suggestion that this systematic uncertainty could ultimately limit future runs of the present experiment with superior statistics. Methods to reduce and possibly eliminate this systematic effect are discussed in Appendix B.

A summary of the measurement uncertainties discussed in this section is shown in Table 4.5. Additional uncertainties that were considered and found to be negligible are also noted.

## 4.6    Discussion of Result

Treating the two systematic uncertainties described in Section 4.5 as independent, the result for $E_1$ is

$$E_1 = -0.001 \pm 0.005(stat) \pm 0.004(syst). \tag{4.41}$$

The statistical and systematic errors can also be combined in quadrature to yield a single error of

$$E_1 = -0.001 \pm 0.006. \tag{4.42}$$

| Determination of $y$ | $\phi$ |
| --- | --- |
| Beta-asymmetry[29] | $180.3 \pm 1.8°$ |
| Beta-gamma CP[30][31] | $180.2 \pm 1.2°$ |
| Average | $180.3 \pm 1.5°$ |

Table 4.6: Determination of $\phi$ based on this result and other determinations of $y$.

Using Equation 2.31, this result can be expressed in terms of $y$ and the $T$ violating phase $\phi$. In Figure 4.25, this is shown along with the previous measurement of $E_1$ and the complementary measurements of the beta-gamma circular polarization and the beta-asymmetry.

The results for $\phi$ are summarized in Table 4.6 using three different determinations for $y$. As shown in the table, the lower value of $|y|$ from the beta-asymmetry measurement[29] results in a larger error in $\phi$ than that obtained using the beta-gamma circular polarization measurements[30][31]. Finally, the result for $\phi$ is also quoted using an average of these two determinations of $y$. Using the average of these two techniques for a final determination of the $T$ violating phase one obtains,

$$\phi = 180.3 \pm 1.5° \tag{4.43}$$

This represents a factor of 4 improvement over the previous result of $\phi = 183 \pm 6°$[27]. The necessary steps to further improve this limit are outlined in Appendix B.
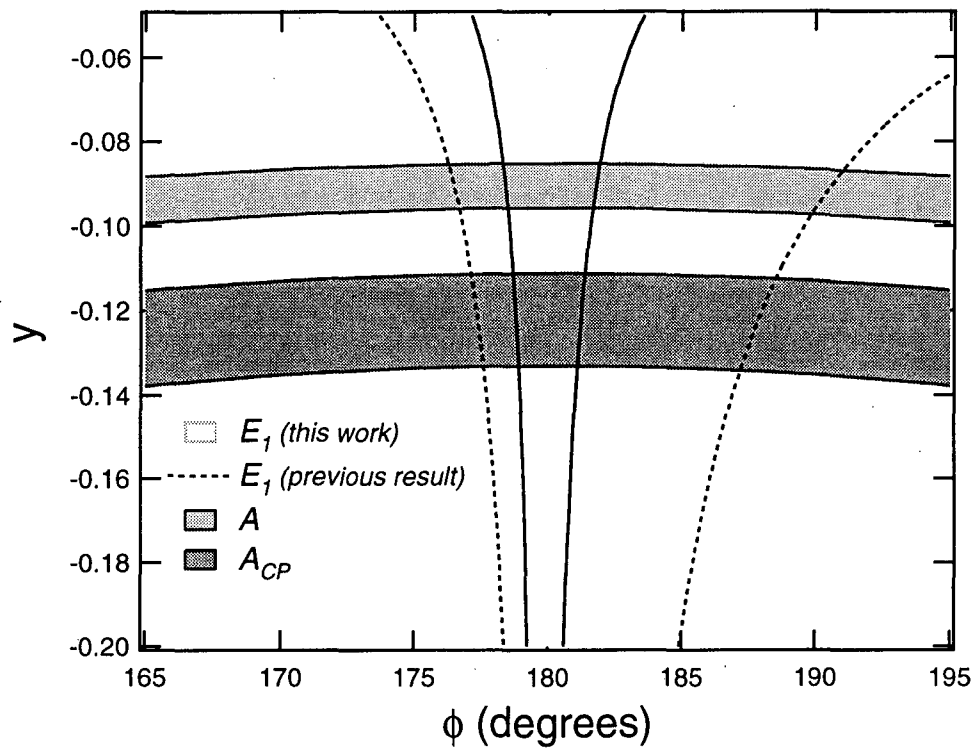
Figure 4.25: Determination of $\phi$ and $y$ for $^{56}$Co based on measurements of $E_1$, the $\beta$-asymmetry $A$[29] and the $\beta - \gamma$ circular polarization $A_{CP}$[30][31]. Error bands are $1\sigma$.

# Appendix A

# Solid Angle Corrections

The solid angle corrections used in this experiment are calculated according to an approach first derived by Rose[60]. Given a general angular distribution of the form

$$W(\beta) = \sum_K a_K P_K(\cos \beta), \tag{A.1}$$

the observed distribution will be

$$\bar{W}(\beta) \quad = \quad \frac{\int W(\beta)\varepsilon d\Omega}{\int \varepsilon d\Omega} \tag{A.2}$$

$$= \quad \frac{\sum a_K \int P_K(\cos \beta)\varepsilon d\Omega}{\int \varepsilon d\Omega} \tag{A.3}$$

where the integrals are over the face of the detector and $\varepsilon$ reflects an angular dependent detection efficiency. Assuming that the detector is cylindrically symmetric, $\varepsilon = \varepsilon(\theta)$. If the cylindrical axis of the detector is located at an angle $\beta_0$, then the direction of the observed $\gamma$-ray can be characterized with angles $(\theta, \phi)$ relative to this detector axis. To evaluate the correction factors, it is necessary to rotate the z-axis to the cylindrical axis defined by the detector. By application of the addition theorem for spherical harmonics

$$P_K(\cos \beta) = \sum_\lambda C^*_{K\lambda}(\beta_0, 0) C_{K\lambda}(\theta, \phi) \tag{A.4}$$

so that

$$\bar{W}(\beta) = \frac{\sum a_K \int \sum_\lambda C_{K\lambda}^*(\beta_0,0)C_{K\lambda}(\theta,\phi)\varepsilon(\theta)d\Omega}{\int \varepsilon(\theta)d\Omega}. \qquad (A.5)$$

Since we are assuming cylindrical symmetry, the integral over $\phi$ is trivial and only the $\lambda = 0$ term will survive in the above sum. The observed radiation pattern reduces to

$$\bar{W}(\beta) = \frac{\sum a_K P_K(\cos\beta_0) \int P_K(\cos\theta)\varepsilon(\theta)d\Omega}{\int \varepsilon(\theta)d\Omega}. \qquad (A.6)$$

and by comparison with Equation A.1, the obvious definition for the solid angle correction factor is

$$Q_K = \frac{\int P_K(\cos\theta)\varepsilon(\theta)d\Omega}{\int \varepsilon(\theta)d\Omega}. \qquad (A.7)$$

To evaluate this expression, it is necessary to assume a model for the detector efficiency $\varepsilon(\theta)$. Assuming that the detection efficiency is related to the path length $x(\theta)$ that the $\gamma$-ray traverses in the detector (neglecting multiple scattering effects), the efficiency can be characterized by

$$\varepsilon(\theta) \propto 1 - \exp[-\tau x(\theta)], \qquad (A.8)$$

where $\tau$ is the absorption coefficient, which will depend upon the gamma-ray energy. With this expression, it is possible to perform a numerical evaluation of Equation A.7. It is worth noting that this calculation will slightly overestimate the correction factors since in the analysis of this experiment only photopeak events are considered. This effectively reduces the solid angle of the detector since the edges are not likely to successfully contain the entire energy of the incident $\gamma$-ray.

# Appendix B

# Future efforts

There are three areas of possible improvement for future $T$ violation searches in this system. These areas include refrigeration, source strength and background elimination.

The Oxford 400 dilution refrigerator provided both an acceptable base temperature and long term stability. However, at mK temperatures it is capable of delivering far more cooling power than is required for this type of experiment. The heat generated by the radioactive source is a few orders of magnitude less than the cooling power of the Oxford 400. This large refrigerator required at least one week to cool down from room temperature to mK temperatures. A smaller refrigerator with less cooling power could be cycled more quickly (24 hours) so that slight changes to the internal apparatus do not require significant delays.

The source strength can be significantly increased without concern for damaging the host crystal. Using the current implantation scheme at Argonne National Laboratory, it is conceivable to increase the source activity by at least another factor of 10. An immediate factor of 5 can be gained simply by re-positioning the implantation target ladder. Currently this ladder sits inside the focus of a quadrupole magnet. Moving the target ladder further downstream from this element will enable more precise tuning of the beam onto the target crystal area. This adjustment, combined with a higher activity cone and longer implantation time, can easily increase the source strength by at least an order of magnitude. This more intense source can reduce the statistical error in $E_1$, but additional improvements should be considered to address the systematic errors as well.

To significantly reduce this limit on $E_1$, it will be necessary to better constrain the background contributions that lead to the systematic errors discussed in Section 4.5. The best approach is to effectively eliminate both the beta-gamma and annihilation-gamma background coincidences.

In both cases, superior background reduction can be achieved with higher resolution, primary gamma-ray detectors. Use of germanium instead of NaI($Tl$) for the $E_1$ sensitive detectors would provide better constraints on the various cascades and allow for tighter energy gates. However, due to the relatively small size of the germanium detectors, several of them would be necessary to obtain an acceptable total solid angle.

Significant reduction of the beta-gamma background coincidences can be achieved by requiring a triple coincidence for every event. Instead of simply requiring a beta-gamma coincidence, detection of the annihilation radiation can also be required. This can effectively eliminate those events which arise from gamma-gamma coincidences due to Compton scattering in the beta detector. Such an additional requirement will necessarily reduce the coincidence rate, but with the current detector arrangement, there is space directly below the source to place more annihilation detectors.

To reduce the annihilation-gamma background coincidences, it is necessary to better identify the annihilation events. The "peak" cut discussed in Section 4.5 has only about a one percent background coincidence contribution when used with a pair of the NaI($Tl$) annihilation detectors. Use of the same energy criteria, but with high resolution germanium detectors, could easily reduce this background to a negligible amount.

# Bibliography

[1] Based on an analogy with the electromagnetic interaction, Fermi's original formulation of beta decay incorporated only a vector term. As such, it was parity invariant.

[2] R. W. Birge, R. P. Haddock, L. T. Kerth, et al. *Physical Review*, 99:1042, 1955.

[3] L. W. Alvarez et al. *Physical Review*, 101:503, 1956.

[4] T.D. Lee and C.N. Yang. *Physical Review*, 104:245–258, 1956.

[5] C. S. Wu et al. *Physical Review*, 105:1413, 1957.

[6] R. L. Garwin, L. M. Lederman, and M. Weinrich. *Physical Review*, 105:1415, 1957.

[7] J. I. Friedmand and V. L. Telegdi. *Physical Review*, 105:1681, 1957.

[8] H. Frauenfelder et al. *Physical Review*, 106:386, 1957.

[9] M. Goldhaber, L. Grodzins, and A. W. Sunyar. *Physical Review*, 109:1015, 1958.

[10] J. H. Christenson, J. W. Cronin, V. L. Fitch, and R. Turlay. *Physical Review Letters*, 13(4):138, 1964.

[11] G. Luders. *Annals of Physics*, 2:1, 1957.

[12] C. Caso et al. *European Physics Journal*, C3:1, 1998.

[13] E. Blanke et al. *Physical Review Letters*, 51:355, 1983.

[14] A. Altarev et al. *Physics Letters B*, 276:242, 1992.

[15] D. DeMille E. D. Commins, S. B. Ross and B. C. Regan. *Physics Letters A*, 50(4):2960, 1994.

[16] N. K. Cheung, H. E. Henrikson, and F. Boehm. *Physical Review C*, 16(6):2381, 1977.

[17] C. E. Overseth and R. F. Roth. *Physical Review Letters*, 19:391, 1967.

[18] B. Winstein et al. Preliminary result from kTeV collaboration presented at the 1998 Wien Conference.

[19] L. M Seghal and M. Wanninger. *Physical Review D*, 46:1035, 1992.

[20] P. Heileger and L. M. Sehgal. *Physical Review D*, 48:4146, 1993.

[21] R. I. Steinberg, P. Liaud, B. Vignon, and V. W. Hughes. *Physical Review D*, 13:2469, 1976.

[22] A. L. Hallin, F. P. Calaprice, D. W. MacArthur, L. E. Pilonen, et al. *Physical Review Letters*, 52:337, 1984.

[23] M. B. Schneider, F. P. Calaprice, A. L. Hallin, D. W. MacArthur, and D. F. Schreiber. *Physical Review Letters*, 51:1239, 1983.

[24] M. Allet et al. *Physical Review Letters*, 68:572, 1992.

[25] E. Ambler, R. W. Hayward, D. D. Hoppes, and R. P. Hudson. *Physical Review*, 108:503, 1957.

[26] E. Ambler, R. W. Hayward, D. D. Hoppes, and R. P. Hudson. *Physical Review*, 110:787, 1958.

[27] F. P. Calaprice, S. J. Freedman, B. Osgood, and W. C. Thomlinson. *Physical Review C*, 15(1):381, 1977.

[28] J. D. Jackson, S. B. Treimen, and H. W. Wyld Jr. *Physical Review*, 106:517, 1957.

[29] W. P. Lee et al. *Physical Review C*, 32(5):1715, 1985.

[30] J. Markey and F. Boehm. *Physical Review C*, 26(1):287, 1982.

[31] H. Behrens. *Z. Phys.*, 201:153, 1967.

[32] C. W. Kim and H. Primakoff. *Physical Review*, 180:1502, 1969.

[33] E. D. Commins. *Weak Interactions*. McGraw-Hill, 1973.

[34] B. R. Holstein. *Weak Interactions in Nuclei*. Princeton University Press, 1989.

[35] R. P. Feynman and M. Gell-Mann. *Physical Review*, 109:193, 1958.

[36] B. R. Holstein. *Physical Review C*, 5(5):1529, 1972.

[37] A. Barroso and R. J. Blin-Stoyle. *Physics Letters*, 45B:178, 1973.

[38] R. B. Curtis and R. R. Lewis. *Physical Review*, 107:1316, 1957.

[39] R. B. Firestone, editor. *Table of Isotopes*. John Wiley and Sons, 8th edition, 1996.

[40] W. A. Hardy. *Journal of Applied Physics*, 17:1225, 1961.

[41] L. C. Biedenharn. *Journal of Mathematical Physics*, 31:287, 1953.

[42] J. Weneser and D. R. Hamilton. *Physical Review*, 92:321, 1953.

[43] B. G. Erozolimski et al. *JETP Letters*, 23:663, 1976.

[44] H. Marshak. *Journal of Research*, 88(3):175, 1983.

[45] J. M. Daniels. *Oriented Nuclei*. Academic Press, 1965.

[46] W. A. Hardy. *Journal of Applied Physics*, 17:1225, 1961.

[47] M. J. Penn et al. *Journal of Applied Physics*, 79:8179, 1996.

[48] *Fifth International Workshop on Low-Temperature Detectors*, volume 93, 1993.

[49] G. F. Knoll. *Radiation Detection and Measurement*. Wiley, 1989.

[50] R. MacKenzie et al. *Physical Review*, A7:135, 1973.

[51] The silicon sample used in this work was provided by B. Cabrera. The titanium contacts were prepared by B. Young.

[52] J. B. Marion and F. C. Young. *Nuclear Reaction Analysis*. North-Holland, 1968.

[53] M. J. Penn. PhD thesis, Stanford University, 1996.

[54] The cobalt single crystals were obtained from Oxford Metals and Oxides, Oxford, UK.

[55] B. Hinfurtner, E. Hagn, E. Zech, and R. Eder. *Physical Review Letters*, 64(18):2188, 1990.

[56] This solvent, whose exact contents are unknown, is available from Buehler Inc., Illinois, USA.

[57] This impantation was made possible by Robert Janseens and the excellent technical support staff at the ATLAS accelerator.

[58] R. Eder, E. Hagn, E. Zech, and M. Deicher. *Physical Review Letters*, 61(11):1301, 1988.

[59] The CHAOS data acquisition system was developed at Lawrence Berkeley National Laboratory over several years. Installation of the system for this experiment was made possible by former laboratory employee Bill Rathbun.

[60] M. E. Rose. *Physical Review*, 91:610, 1953.

ERNEST ORLANDO LAWRENCE BERKELEY NATIONAL LABORATORY
ONE CYCLOTRON ROAD | BERKELEY, CALIFORNIA 94720